Tesi di laurea Magistrale:

Polarization study of the pulsars in the globular cluster 47 Tucanae

Relatore interno:
Prof. Monica Colpi

Correlatori:
Dott. Andrea Possenti
Dott. Caterina Tiburzi

Presentata da:
Federico Abbate

Matricola # 746959

Contents

Chapter 1

Introduction

The origin of the magnetic field in the Universe is one of the still unsolved and key questions of modern astrophysics (Widrow 2002, Beck 2016). Observations tell us that magnetic fields have been present since the very early universe and have probably played important roles in the formation of stars and in the evolution of galaxies (Longair 2008). However, the processes that formed and amplified these fields are still not clear.

One of the most powerful observational tools for studying the intensity and the shape of the cosmic magnetic fields is the measurement of the *Faraday rotation* of the polarization angle of the radio emission coming from celestial sources. This rotation depends on the integrated intensity of the component of the cosmic magnetic field travelled by the radiation, as well as on the density of the ionized component of the cosmic medium along the line of sight and on the wavelength of the observed radiation. When values of the Faraday rotation can be derived for a significant number of directions towards a given celestial source, a polarization map can be inferred for the source, which, in turn, can provide constraints on the magnetic field permeating the observed celestial object.

Globular clusters are spherical agglomerates of $10^5 - 10^6$ stars, nowadays mostly distributed in the Galactic halo. The stars in them are in most cases coeval and the inner regions of them display a stellar density much higher than almost elsewhere in the Galaxy. Due to those features, globular clusters are primary targets for studying stellar evolution, as well as 3 or 4-body dynamical encounters among stars (Colpi and Devecchi 2009). Despite the presence of magnetic fields is almost ubiquitous in the Universe (they have been observed in most planets, stars, in the interstellar medium of the Milky Way, in external Galaxies, as well as in clusters of Galaxies), no intrinsic large scale magnetic field has been observed so far in a globular cluster.

In this Thesis, we will exploit the measurement of the polarization properties of the pulsars in a given globular cluster in order to investigate if it hosts a large scale magnetic field, and/or to put improved constraints on its magnitude. The results are commented in the framework of the current knowledge about the formation and/or the dissipation of the cosmic magnetic fields.

As anticipated above, in this work the "probes" for the magnetic field are the so-called *pulsars*. They are *neutron stars*, i.e. what is left when a star with a mass between $\sim 8\,M_\odot$ and $\sim 20\,M_\odot$ reaches the end of its life, and then explodes as a supernova. A neutron star is so dense that a mass comparable to that of the Sun is concentrated in a few kilometers radius. Neutron stars have very high magnetic fields and spin fast enough to make a complete rotation in seconds or even milliseconds. They usually emit radio waves in two roughly conical regions around the magnetic

poles, which are not in general coincident with the poles of the rotation axis. If this radiation intercepts our line of sight, we see a pulsed pattern repeating at every rotation of the object. Just because of this reason these objects are called pulsars.

From a precision determination of the times of the arrival of the pulses we can determine the positional, kinematical, and physical properties of the pulsars. For example, we can determine their position in the sky with astrometric accuracy, their proper motion, their spin-down rates, their breaking index and the surface magnetic field. If the pulsar is in a binary system, we can also determine all the Keplerian (and in some favorable cases, also the post-Keplerian) orbital parameters.

The pulses also carry information about the gas they have to cross to reach the Earth. In its journey, the radiation at different frequencies is delayed by an amount proportional to the density of the free electrons in the gas. Moreover, as already reported above, if a magnetic field also permeates the gas, we see the effects of the *Faraday rotation*.

The pulsars are mainly found in the Galaxy disk, but a significant population of them is hosted in globular clusters. 47 Tucanae is the globular cluster with the second largest population of observed pulsars, with 25 such objects (Pan et al. 2016). It is also one of the closest to the Earth and thus it is an ideal globular cluster to be investigated. For example, the observation of the pulsars in 47 Tucanae led to the discovery - and the first determination of the density - of an intra-cluster ionized medium in a globular cluster (Freire et al. 2001b).

The immediate aim of my work is to perform a study of the polarization properties of the pulsars in 47 Tucanae - never performed before for the lacking of suitable data. The collected information will then be used to search for the presence of a magnetic field embedded in 47 Tucanae . Since the angular separation of the targeted pulsars in the sky is very small (of the order of the arcseconds), the same observations could possibly probe the turbulent nature of the interstellar medium along the line of sight over these small scales.

The observations were made at the Parkes radio telescope in Australia over a span of almost a year.

In the two subsequent chapters I briefly report on the observational and theoretical properties of the pulsars and of globular clusters, with a focus in particular on the globular cluster population of pulsars and on the specific case of 47 Tucanae. In chapter 4 I describe the observational techniques used in pulsar observations focusing on the determination of the polarization properties of these radio sources. In chapter 5 I present all the steps of the analysis - from the raw data to the calibrated pulse profiles -, the codes used to determine the Faraday rotation, and a summary of the results of this data analysis. The considerations on the possible magnetic field underlying the observed polarization properties, and on its possible origin - inside or outside the globular cluster - are eventually made in chapter 6. Finally, in chapter 7 I draw the conclusions and show the possible improvement of the results which could arise from the observation of 47 Tucanae with new telescopes, like MeerKAT and SKA.

Chapter 2

Pulsar overview

Pulsars (short for pulsating radio stars) are rapidly rotating, highly-magnetised neutron stars. They emits radiation in a beam and every orbit the path of beam crosses our line of sight and we are able to see very regular pulses of light.

The first pulsar (PSR B1919+21 with a period of 1.3 s) was discovered in 1967 by Anthony Hewish and Jocelyn Bell Burnell (fig. 2.1) and, after a deep analysis to eliminate the possibility of it being a Earth-made signal, the discovery was published in February of 1968 (Hewish et al. 1968). At the very beginning, they could not completely exclude that the signal was originating from an extra-terrestrial intelligent civilisation and so the source was nicknamed LGM-1 (short for Little Green Man) but later, with the discovery of other pulsars, this hypothesis was discarded. In 1974, for this reason, Hewish was awarded the Nobel prize for Physics together with Martin Ryle.
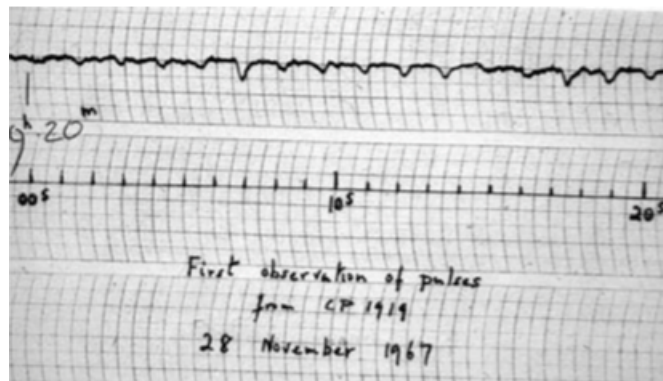
Figure 2.1: Pen-chart recording of the pulses observed from the first pulsar PSR B1919+21 detected. (From Hewish 1975)

Neutron stars had already been predicted by a number of theoretical works (Landau 1932, Baade and Zwicky 1934, Oppenheimer and Volkoff 1939) and it had been proposed that they could be produced in supernova explosions (Colgate and White 1966). Furthermore, other papers suggested that such stars would be rapidly rotating (Hoyle et al. 1964) and highly magnetised (Wheeler 1966).

The first connection between pulsars and neutron stars was made by Gold (1968) who argued that neutron stars could explain many observational properties of pulsar, but this theory wasn't fully accepted until the discovery of the Crab pulsar and the slowdown of its period.

1 Observed properties of pulsars

Some of the general properties of pulsars we can infer by observing their emission are (Manchester 2004, Lorimer and Kramer 2005):

- The period between pulses varies from ~ 1.3 ms to ~ 8 s.

- The period is not constant but slowly increases with a period derivative between $10^{-20} - 10^{-12} s\, s^{-1}$. From these two properties we can infer that there are two distinct population of pulsars, the 'millisecond pulsars', with periods between 1.3 and 10 ms and period derivative between 10^{-19} and $10^{-21} s\, s^{-1}$, and 'normal pulsars', with period clustering between 0.1 and 8 s. and period derivative between 10^{-12} and$10^{-15} s\, s^{-1}$.

- The surface magnetic field (in later sections is shown how to calculate it) is very high, from 10^8G up to 10^{15}G

- The distribution of pulsars in the sky shows a clear correlation with the galactic disk but has a scale height much larger than the stars that supposedly originated them because of the very high peculiar velocities of this objects. The millisecond pulsars are distributed more isotropically mostly because of selection effects. We can only see the ones close to us. With future instruments it may be possible to observe a concentration in the galactic disk. (Fig. 2.2).
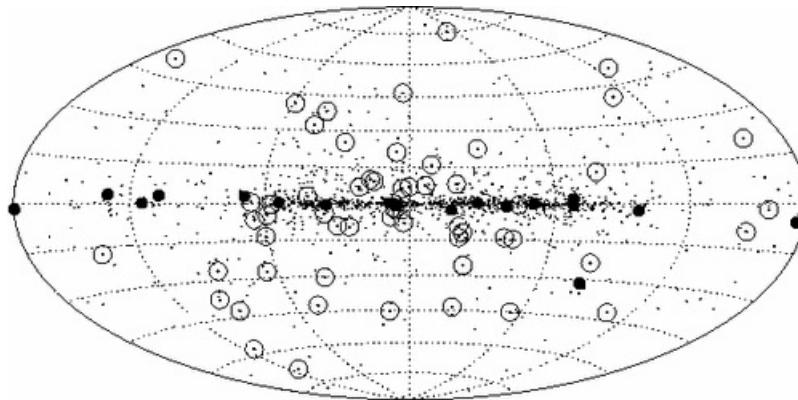
Taken from "Handbook of Pulsar Astronomy" by Lorimer & Kramer

Figure 2.2: Distribution of pulsars in Galactic coordinates. The dots are the normal pulsars, the open circles are millisecond pulsars and the filled dots are pulsars with known SNR (Supernova Remnant) association. From Lorimer and Kramer 2005.

2 Pulsars as rotating neutron stars

Following the book "Black Hole, White Dwarfs and Neutron Stars" by Shapiro and Teukolsky (1983) it is possible to prove why neutron stars are the only known objects that can be responsible for all the observed properties of the pulsars. The most stringent properties are: very short periods (from ~ 1.3 ms to ~ 8 s); periods that always tend to increase very slowly but never decrease.

In a time lapse of 1.3 ms light travels about 400 km. This means that the emitting region cannot be bigger than this size and it is improbable that the source is much bigger than the emitting region. This means that we are dealing with very small objects such as compact objects: white dwarfs, neutron stars or black holes. The only possible mechanisms of producing such a precise clock are: rotation, pulsation or binary systems.

Let's consider that the source is a white dwarf, in this case the fastest possible rotation is at the break-up velocity:

$$\Omega^2 R \sim \frac{GM}{R^2} \tag{2.1}$$

where Ω is the angular velocity of rotation. It can be rewritten in the form:

$$\Omega^2 \sim G\rho \tag{2.2}$$

which links the period of a rotation to the dynamical timescale of the object. For a white dwarf, with $\rho = 10^8 \, \mathrm{gcm}^{-3}$, we obtain $P \geq 1s$.

A pulsating white dwarf would have a similar period for the fundamental harmonic and even smaller for higher harmonics. The problem in a pulsating star is that a loss of energy would cause a decrease in the period which is never observed.

So we have to discard the hypothesis that white dwarfs are responsible for the pulsar emission and we move to consider a neutron star. A pulsating neutron star would still have a negative period derivative and furthermore the window of possible periods would be too small to embrace all observed periods. It is possible to construct a binary neutron star system with an orbital period similar to the observed ones but the orbit would be too small and gravitational wave emission would shrink the binary even further making it collapse in a very short timescale. In this case the orbital period derivative would be negative because of the shrinking of the orbit.

The case of a black hole is impossible because it has no surface to which to attach a periodic emitter and any accretion phenomenon would not have such a precise period.

So, in conclusion only a rotating neutron star is compatible with all the observed properties of pulsar and as we will see in a later section both these objects are linked to the death of a massive star and the subsequent supernova explosion.

3 Important pulsar discoveries

Since the first detection of pulsar by Anthony Hewish and Jocelyn Bell, numerous pulsars have been discovered and today we know around 2500 of them. Some of the most important pulsar discovered are:

- The first binary pulsar B1913+16 was found by Russell Hulse and Joseph Taylor in 1974 (Hulse and Tayolr 1975) with an orbital period of ~ 7.75h. The binary will coalesce in about 200 Myr due to the emission of gravitational waves. The measurement of the orbital shrinkage

of this system led to the first experimental demonstration of gravitational waves. Hulse and Taylor were awarded the 1993 Nobel prize for Physics for their achievement.

- The first millisecond pulsar B1937+21 by Shrinivas Kulkarni, Donald Backer and collaborators (Backer et al. 1982) with a period of ~ 1.6 ms. It remained the fastest known pulsar until the discovery of J1748-2446ad (Hessels et al. 2006) in the globular cluster Terzan 5.

- The first pulsar in a globular cluster discovered in M28 by Andrew Lyne and collaborators at Jordell Bank (Lyne et al. 1987). Since then globular clusters have been found to host a very large population of millisecond pulsars.

- The first planetary pulsar system B1257+12 by Alexander Wolszczan and Dale Frail in 1990 (Wolszczan and Frail 1992). This system contains two Earth-mass planets and one of lunar mass. It was the first extra-solar planetary system discovered.

- The first triple system B1620-26 which consists of a pulsar, a white dwarf and a Jupiter-mass planet discovered by Stephen Thorsett and collaborators (Backer et al. 1993) in the globular cluster M4. This is one example of the very diverse systems which can be found in globular clusters.

- The first double pulsar system J0737-3039 by Marta Burgay and collaborators (Burgay et al. 2003, Lyne et al. 2004). This system consists of a ~ 22.7 ms pulsar in orbit around a ~ 2.77 s pulsar and promises to give the tightest constraints ever given on strong-field gravitational theories.

- The first triple system comprising 3 compact bodies, 2 white dwarfs and 1 neutron star (Ransom et al. 2014). It is allowing us to obtain the most precise investigation of the non relativistic 3 body problem.

4   Birth of neutron stars

Neutron stars are the endpoint of the evolution of massive stars ($\geq 8 - 11\, M_\odot$) which end their lives in violent explosions called Type II Supernova. The theory exposed follows the book "Stellar Structure and Evolution" by Kippenhahn, Weigert and Weiss (2012) and "Black Hole, White Dwarfs and Neutron Stars" by Shapiro and Teukolsky (1983).

A star is always in a complex hydrostatical equilibrium between gravity which would tend to collapse the star and the thermonuclear reactions happening in the center which tend to expand it. After a star has burnt all of the hydrogen in the center the reactions proceed in a shell until the center becomes hot enough to start the fusion of the helium atoms into carbon. Only stars over a certain mass limit ($\sim 2\, M_\odot$) can reach this stage and this fusion continues until a carbon-oxygen core is formed. Stars with masses lower than $\sim 8 - 11\, M_\odot$ (the limit depends on the metallicity) expel all the exterior shells and end their lives as a carbon-oxygen white dwarf. Stars of higher mass, on the other hand, can ignite the carbon in the core and proceed burning all the elements up to iron.

Further fusion reactions beyond iron absorb energy instead of releasing it. So without a source of energy to sustain it, the star must collapse. Since the core is much denser than the rest of the star, its timescale of collapse is also much smaller and its evolution must be considered separately.

When the mass of the core is similar to the Chandrasekhar mass limit of $1.4\,M_{\odot}$ its collapse cannot be stopped by the degeneracy pressure of the electrons (in which case it would become a white dwarf) but proceeds even further. In this stage the temperature rises and the iron nuclei are dissociated by energetic photons into He atoms and free neutrons. As the temperature rises even further the He atoms are dissociated into free nucleons. These processes lower the radiation pressure in the core and speed up the collapse. A great number of neutrinos are produced in various reactions and they contribute to lower the energy content of the core. A final reaction happening in the core we must consider is the inverse beta decay of protons and electrons into neutrons. When the core becomes fully populated by neutrons and neutrinos, the neutrons become degenerate and their degeneracy pressure is enough to stop the collapse of the core forming what is called a neutron star. The neutrinos then rapidly escape carrying most of the energy released.

The outer shells of the star which evolve much slower keep contracting until they reach the solid surface of the neutron star. A powerful shockwave is produced and propagate outwards causing chain reactions that synthesise all the heavy elements. The kinetic energy released in the collapse alone is not sufficient to push the shockwave to the outer layers and produce the observed Supernova explosion. A major contribution is given by the very energetic neutrinos that escape the star after the creation of the neutron stars. Only a small fraction of them is able to interact with the matter in the star but these few reactions release enough energy to power the explosion.

5 Pulsars and Supernova Remnants

By the theory exposed just now we should expect to find pulsars in Supernova Remnants (SNRs) and in fact one of the earliest places we found pulsars is in young SNRs like the Crab Nebula (fig. 2.3)and the Vela Nebula. The discovery of the Crab Pulsar was very important also for other reasons we will see in later sections. Currently there are many possible associations between SNR and pulsars (78 according to Su et al. 2013).

Even though the only canonical way to make a neutron star is through a Supernova (other methods concerning the accretion induced collapse of white dwarfs have been proposed (Bhattacharya and van den Heuvel 1991)), it is highly possible to find SNR with no pulsar or pulsars with no observed SNR nearby.

Let's first consider the case of a SNR with no pulsars. The first thing to note is that neutron stars are visible as pulsars only if the beam crosses our line of sight (the covering factor of the beam is of the order of 1-10%), but in this case we should still be able to see the X-ray emission of the neutron star, which is isotropic. The most important cause of these missed associations is that at the explosion the neutron star can receive a "kick" of several hundreds of km/s possibly due to asymmetries in formation of the compact object (Lyne and Lorimer 1994), which can move the line of sight of the pulsar far from that of the SNR.

The case of pulsars with no visible SNR can be further explained by the fact that SNR last only up to $10^6 - 10^7$ yrs while a pulsar can survive much longer, especially in the case of a millisecond pulsar. So the SNR that originated with the pulsar might already be dissolved into the ISM (Interstellar Medium).
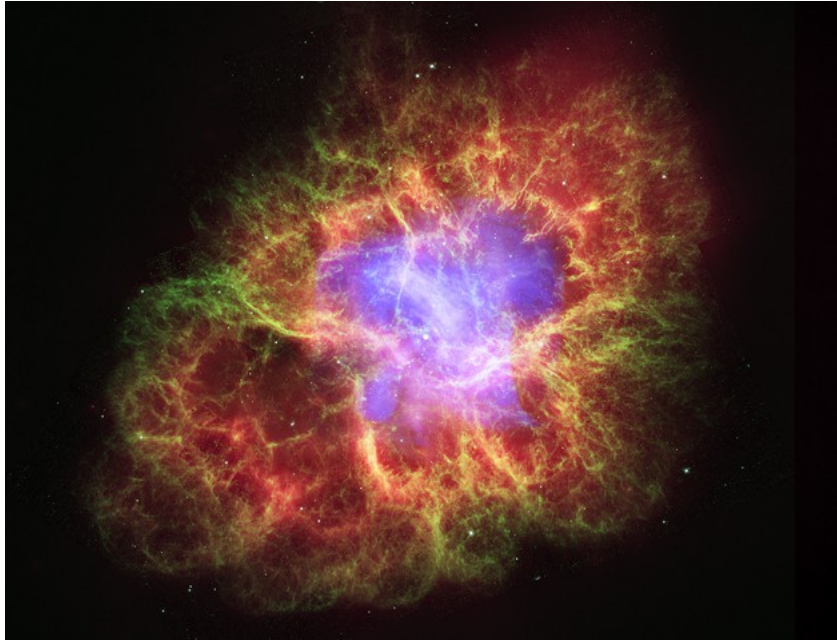
Figure 2.3: Optical, infrared and X-ray composite image of the Crab nebula, the pulsar is the bright spot in the center. Optical image by HST, infrared image by Spitzer and X-ray image by Chadra.

6   Theoretical model of pulsars

Finding a complete theoretical model of neutron stars that describes the internal structure, the external atmosphere and the emission processes is a very complicated task which is not solved today. However starting from the observations we are capable of deriving different relations between quantities that can be used to constrain the various models. (Lorimer and Kramer 2005)

6.1   Mass and radius

Measuring the masses and radii of neutron stars is essential to find the equation of state (and composition) governing the compact object. The mass can be measured very precisely by analysing the arrival time of pulses in a binary pulsar (this method called "timing" is described in later sections) and the results are plotted in fig. 2.5. Most of the masses are consistent with $1.4 M_\odot$ that is predicted by the theory of formation of neutron stars proposed in a previous section. However some of the pulsar, especially the older ones, have higher masses probably because they accreted matter during the recycling phase (see section on binary pulsars).

Every equation of state proposed has a range of masses between which the neutron star can exist (Shapiro and Teukolsky 1983, Cook et al. 1994). The minimum masses are typically of the order of $0.1 M_\odot$ and the maximum masses are typically around $2 M_\odot$. When we observe neutron stars with masses higher than the theoretical maximum we can use observations to disprove the related equations of state.
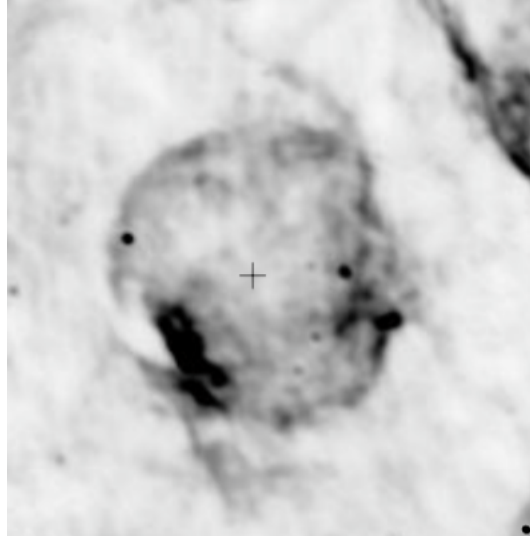
Figure 2.4: Pulsar PSRJ1119-6127 found in the young SNR G292.2-0.5 (Crawford et al. 2001)

The estimate of the radius can be made by observing the X-ray thermal emission of the surface of the neutron star after correcting for the effects of gravitational redshift and of the atmospheric plasma. However, a lower limit can be found providing that the speed of sound in a neutron star can't be higher than the speed of light. An upper limit can be given by requiring that the rotational speed is lower than the break-up speed. The real radius therefore must be in the interval 6-16 km for a millisecond pulsar with a mass of $1.4 M_\odot$.

6.2   Energetics

The binding energy of a neutron star (taking typical values for mass and radius) is $\sim \frac{GM^2}{R} \sim 3 \cdot 10^{53}$ erg. This is the energy released in neutrinos at the formation of the neutron star. The typical moment of inertia is $I \sim kMR^2 \sim 10^{45} \mathrm{g\,cm^2}$ (where k depends on the density profile and is 0.4 for uniform density). A precise measurement will be hopefully possible only through long-term precise timing of the Double Pulsar J0737-3039.

For comparison let's calculate the rotational and the magnetic energy:

- The rotational energy is $\sim 0.5 I \Omega^2 = 0.5 I \left(\frac{2\pi}{P}\right)^2$ which is 10^{47} erg for normal pulsars and 10^{53} erg for millisecond pulsars. So it can be of the same order of the binding energy of the star. The rotational energy is the main source of the observed luminosity for normal and millisecond pulsars.

- The magnetic energy is typically $\sim (1/6) B^2 R^3 \sim 10^{42}$ erg for a magnetic field of 10^{12}G. So the magnetic energy has little importance in the total energy budget unless the magnetic field is very strong $\sim 10^{15}$ G as it is in *magnetars*.
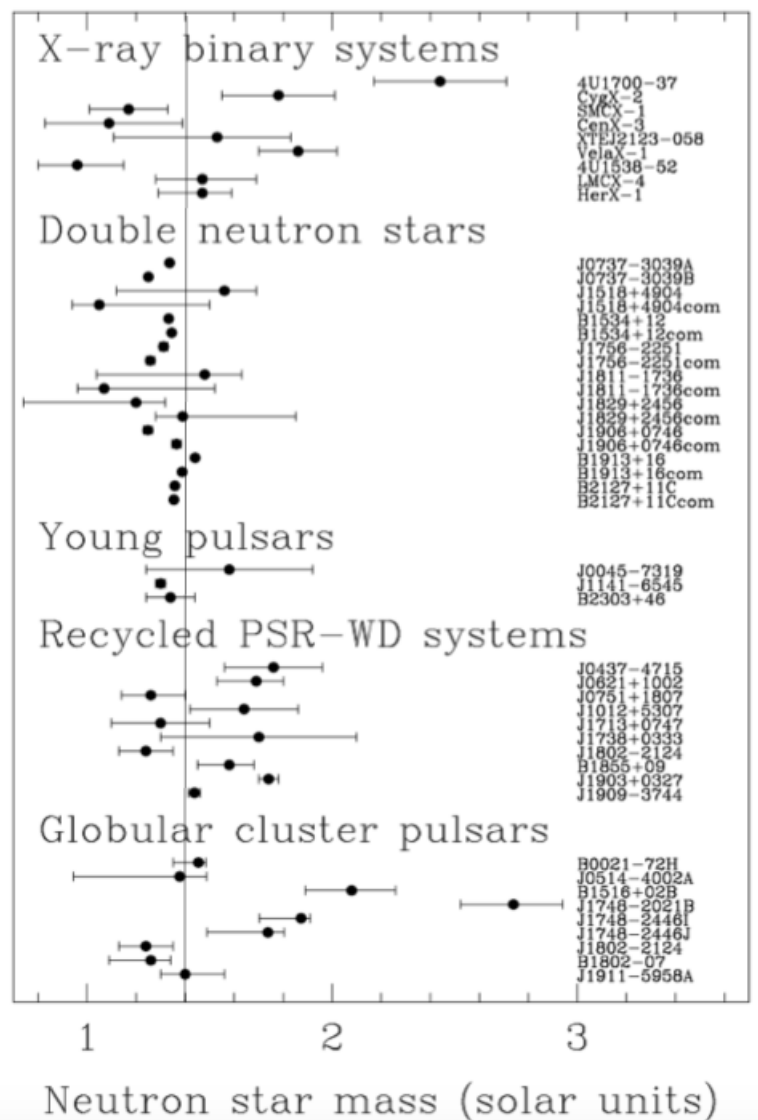
Figure 2.5: Measured masses of pulsars of different types, the vertical line at $1.4 M_\odot$ represents the typical predicted mass (Lorimer 2008)

6.3   The magnetic dipole model

The periods of the pulsars are seen to increase with time with a time derivative $\dot{P}$. This can be linked to a loss of kinetic rotational energy through the equation:

$$\dot{E} = -\frac{dE_{rot}}{dt} = -\frac{d(I\Omega^2/2)}{dt} = -I\Omega\dot{\Omega} = -(4\pi^2)I\dot{P}P^{-3}. \tag{2.3}$$

The quantity $\dot{E}$ is the total power output by the neutron star and is called *spin-down luminosity*. For a canonical normal pulsar it is $\sim 4 \cdot 10^{31}\mathrm{erg\,s^{-1}}$. Only a very small part of this luminosity is observed in the radio pulses.

A pulsar has a very strong magnetic dipole and, as it rotates with a rotational angular frequency Ω, it emits radiation (see, for example, Jackson 1962). The power emitted is:

$$\dot{E}_{dipole} = \frac{2}{3c^3}|\mathbf{m}|^2\Omega^4\sin^2\alpha, \tag{2.4}$$

where α is the angle between the magnetic axis and the rotational axis. If all the energy lost is emitted as dipole radiation we obtain the equation:

$$\dot{\Omega} = -\left(\frac{2|\mathbf{m}|^2\sin^2\alpha}{3Ic^3}\right)\Omega^3. \tag{2.5}$$

Usually this equation is written in a more general form using $\nu = 1/P$ as variable

$$\dot{\nu} = -K\nu^n, \tag{2.6}$$

where n is called *braking index* and is 3 for the dipole case but different if we consider other dissipation mechanisms. The *braking index* can be measured directly if we know the second derivative of the spin frequency by measuring $n = \nu\ddot{\nu}/\dot{\nu}^2$. Measured values range from 1.4 to 2.9 (Kaspi and Helfand 2002). Therefore the magnetic dipole model is not exactly correct but it is still useful when calculating basic properties.

The first property that is useful to calculate is the *characteristic age*. To calculate it rewrite eq. 2.6 as a function of the period, $\dot{P} = KP^{2-n}$ which may be integrated, assuming a constant K and $n \neq -1$ to obtain the age of the pulsar:

$$T = \frac{P}{(n-1)\dot{P}}\left[1 - \left(\frac{P_0}{P}\right)^{n-1}\right], \tag{2.7}$$

where P_0 is the spin period at birth. If we assume it was much shorter than what we observe today and take $n = 3$ as in the dipole, we find the *characteristic age*:

$$\tau_C \equiv \frac{P}{2\dot{P}} \simeq 15.8\mathrm{Myr}\left(\frac{\mathrm{P}}{\mathrm{s}}\right)\left(\frac{\dot{\mathrm{P}}}{10^{-15}}\right)^{-1} \tag{2.8}$$

Although not correct, gives an estimate which most of the times is comparable to the real age. The age estimate of the Crab pulsar is ~ 1240 yr, close to the real age of ~ 950 yr. This consideration convinced most astronomers that the theory was more or less correct. However in some case the vast discrepancies with other age estimates, like the ones from proper motion, suggest that we shouldn't take this age very seriously.

If on the other hand we independently know when a pulsar is born we can revert the equation 2.7 to obtain the birth period:

$$P_0 = P \left[1 - \frac{(n-1)}{2} \frac{T}{\tau_C} \right]^{\frac{1}{n-1}} . \tag{2.9}$$

Another important property that can be estimated using the magnetic dipole model is the strength of the magnetic field. This estimate can be made by noting that the magnetic moment is related to the magnetic field strength by the relation $B \approx |\mathbf{m}|/r^3$ and by rearranging accordingly equation 2.5. We obtain the magnetic field strength at the surface:

$$B_S \equiv B(r=R) = \sqrt{\frac{3c^3}{8\pi^2} \frac{I}{R^6 \sin^2 \alpha} P\dot{P}}. \tag{2.10}$$

For a ordinary pulsar and assuming $\alpha = 90°$ we obtain:

$$B_S = 3.2 \cdot 10^{19} \mathrm{G} \sqrt{P\dot{P}} \simeq 10^{12} \mathrm{G} \left(\frac{\mathrm{P}}{\mathrm{s}} \right)^{1/2} \left(\frac{\dot{\mathrm{P}}}{10^{-15}} \right)^{1/2} . \tag{2.11}$$

Because of all the uncertainties this value is nothing more than an order of magnitude estimate, it is however comparable to that measured in X-ray binaries (Wheaton et al. 1979) and isolated neutron stars (Bignami et al. 2003).

6.4   Pulsar magnetosphere

The consideration of section 6.3 are strictly valid only if the neutron star is rotating in the vacuum, but this situation is impossible to maintain in real life. The neutron star can be thought as a highly magnetised rapidly rotating superconductive sphere in which the electric forces on the surface particles are much stronger than the gravitational ones. This leads to the extraction of material from the surface and the creation of a magnetosphere. This model was first suggested by Goldreich and Julian (1969). See figure 2.6 for a sketch of the proposed model.

The strong rotating magnetic dipole induces a very large electric field. The electrical forces can be stronger than the gravitational ones even by 10 orders of magnitude so the charges are stripped from the surface and populate a region of space around the pulsar called magnetosphere. When a state of equilibrium is reached the maximum number density of the plasma in the polar regions is given by the Goldreich-Julian density:

$$n_{GJ} = \frac{\Omega B_S}{2\pi ce} \simeq \frac{B_S}{ceP} = 7 \cdot 10^{10} \mathrm{cm}^{-3} \left(\frac{\mathrm{P}}{\mathrm{s}} \right)^{-1/2} \left(\frac{\dot{\mathrm{P}}}{10^{-15}} \right)^{1/2} \tag{2.12}$$

The plasma in the magnetosphere is forced to co-rotate with the star because of flux freezing. However this high speed rotation can be maintained only up to a certain radius where the speed should reach the speed of light. This radius is called *light cylinder radius* and is defined as:

$$R_{LC} = \frac{c}{\Omega} = \frac{cP}{2\pi} \simeq 4.77 \cdot 10^4 \left(\frac{P}{s} \right) \mathrm{km} \tag{2.13}$$

This cylinder divides the field lines in two types: *closed field lines*, that close on the surface, and *open field lines*, that cannot close. The open field lines define the polar region centred on the magnetic axis. The model proposes that in the magnetosphere there are regions in which the
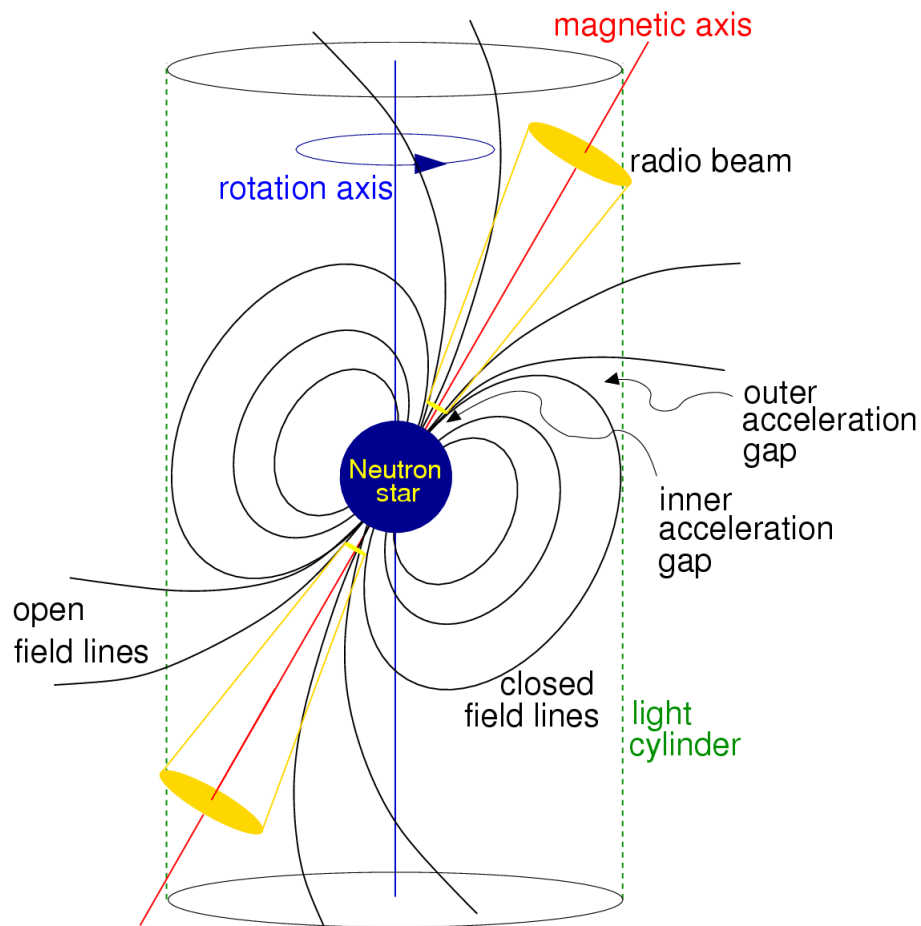
Figure 2.6: Sketch of the model of the pulsar magnetosphere. The various parts will be described in the text (Lorimer 2008)

equilibrium cannot be maintained and there must be residual electric forces. Because of this, these regions are mostly empty but subject to strong accelerations. One of these regions, called *polar gap*, is around the magnetic axis and is thought to generate the particles eventually producing the observed radio emission. The other regions are located around the last closed field line where there should be a separation between positive and negative charges.

7   Pulse profiles

Apart from a few exceptions, pulsars are weak radio sources and for most pulsars it is impossible to study single pulses so it is necessary to sum hundreds or thousands of pulses to form a detectable profile, which is called *integrated profile*. Even though single pulses vary a lot, the integrated profiles are very stable and can be thought as a unique property of the pulsar. (Fig. 2.7)
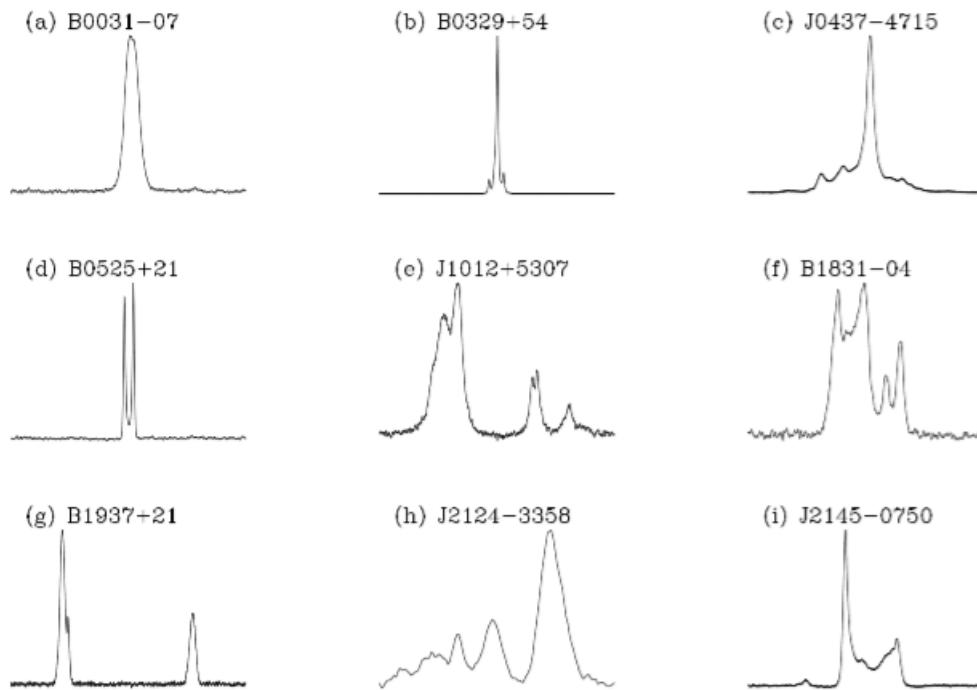
Figure 2.7: plots of various integrated profiles of pulsar.(Lorimer 2008)

Some of the profiles, like 2.7(g) or 2.7(e), show a secondary pulse separated by 180°, called an *interpulse*. A possible cause of this phenomenon is that the magnetic and rotational axis of the neutron star are oriented in a way that both the polar regions intersect our line of sight.

There are two contrasting models that try to explain the different profiles: the "nested cone" model and the "patchy beam" model (fig. 2.8). The "nested cone" model (Rankin 1983) imagines that the emission in the beam comes from an outer conical shell and from an inner shell. Therefore we see different profiles according to how many cones cross our line of sight. In this model a single pulse profile can be seen only when we are just grazing the side of the emission beam. The "patchy beam" model (Lyne and Manchester 1988) on the other hand suggests that the radio beam is only partly filled with small emitting regions distributed at random. In this model the number of pulses is not directly linked to the line of sight in the radio beam.
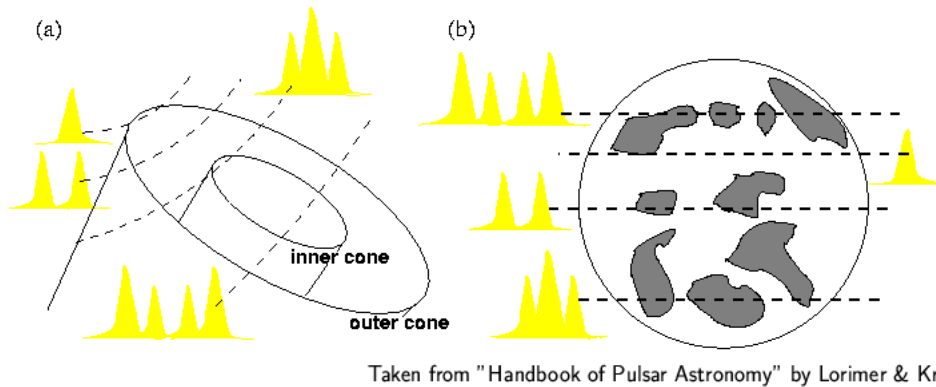
Figure 2.8: Depiction of the different models of the beam, (a) nested cone model (b) patchy beam model(Lorimer and Kramer 2005)

7.1 Rotating Vector Model

Pulsars are also some of the most polarised radio sources. Since important considerations can be derived by studying the polarisation of a signal, we should consider investigating it in more detail.

Usually the position angle of the polarisation varies smoothly along a curve if plotted as a function of the pulse phase. The best model to describe this variation is the Rotating Vector Model (RVM) (Radhakrishnan and Cook 1969).

This model suggests that the variation of the position angle is continuous along an S-shaped curve because of simple geometrical arguments if the direction of linear polarisation follows the direction of the magnetic field at the place of emission. The magnetic field always points in the direction of the magnetic pole and as we sweep along the different line of sights it changes following an S-shaped curve. (Fig. 2.9).

The rotation of the linear polarisation is at most 180° and we can reconstruct the exact position of our line of sight and so we can measure the opening angle of the beam and distinguish which model of the beam structure is better. However only in rare cases this model works so perfectly, sometimes there are jumps in the polarisation angle of 90°, like is described by the Orthogonal Polarisation Model, OPM, by McKinnon and Stinebring (2000). Sometimes the jumps are not orthogonal (Karastergiou et al. 2005) and other times the profile is flattened by interstellar scattering (Li and Han 2003). All these effects make the RVM inapplicable in most of the cases.

8 $\quad P - \dot{P}$ diagram

Using the magnetic dipole model we listed some relationships between the characteristic age τ, the surface magnetic field, the period P and the period derivative $\dot{P}$. Even though this relations are not perfectly satisfied it is very useful to plot the known pulsars in the "$P - \dot{P}$ diagram", fig. 2.10. In this diagram the dashed lines represent lines of constant characteristic age, surface magnetic field and spin-down luminosity taken from the equations 2.7, 2.11 and 2.3.
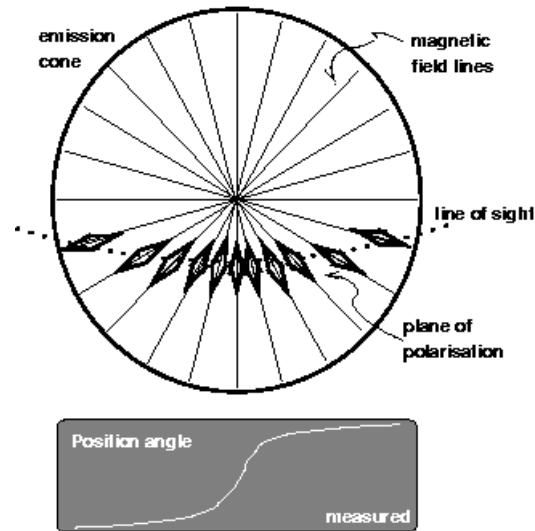
Figure 2.9: Model describing the RVM. The box below shows the variation of the observed position angle as a function of the pulse phase. (Lorimer and Kramer 2005)

This diagram shows very well many properties of pulsars already discussed and other not yet discussed. It is evident at first sight the different nature of millisecond pulsars, which have smaller magnetic fields, and ordinary pulsars, with stronger magnetic fields. It is evident also that most binary pulsars are millisecond pulsars (this is an important characteristic discussed better in a later section), while almost no normal pulsar has a companion. Pulsars emitting at high energy, like Soft Gamma Repeaters (SGR) or Anomalous X-ray Pulsars (AXP) always have very high magnetic fields. SGRs and AXPs are grouped under the name of "magnetars".

The shaded regions of the diagram are the regions we think are forbidden for the radio pulsars. The "death line" separates the region where we find pulsars from the "graveyard". This line corresponds to a constant luminosity of 10^{30}erg/s and under this line we don't see any pulsars (with the exception of one). The theory states that once a pulsar reaches this spin down luminosity it can no longer sustain the radio emission and it shuts down as a pulsar. Most of the models for the radio emission require the creation of pair cascades in the polar region (which then decay creating the emission); if the energy of the pulsar is too low to create the pairs the pulsar cannot emit in radio. If the magnetic field is too high other processes prevent the decay of the pairs into radio photons shutting down the emission. This is a possible reason why we don't expect radio pulsars with very high magnetic fields.

In this particular $P - \dot{P}$ diagram the pulsars with known Supernova Remnant (SNR) associations are also shown, they are only the youngest pulsars because, as we discussed in a previous section, the SNRs live for very short times (around 1-10 Myr).

We can use this diagram to discuss the evolution of normal isolated pulsars.

A pulsar is born after a supernova explosion and at the beginning its rotations is very fast, the
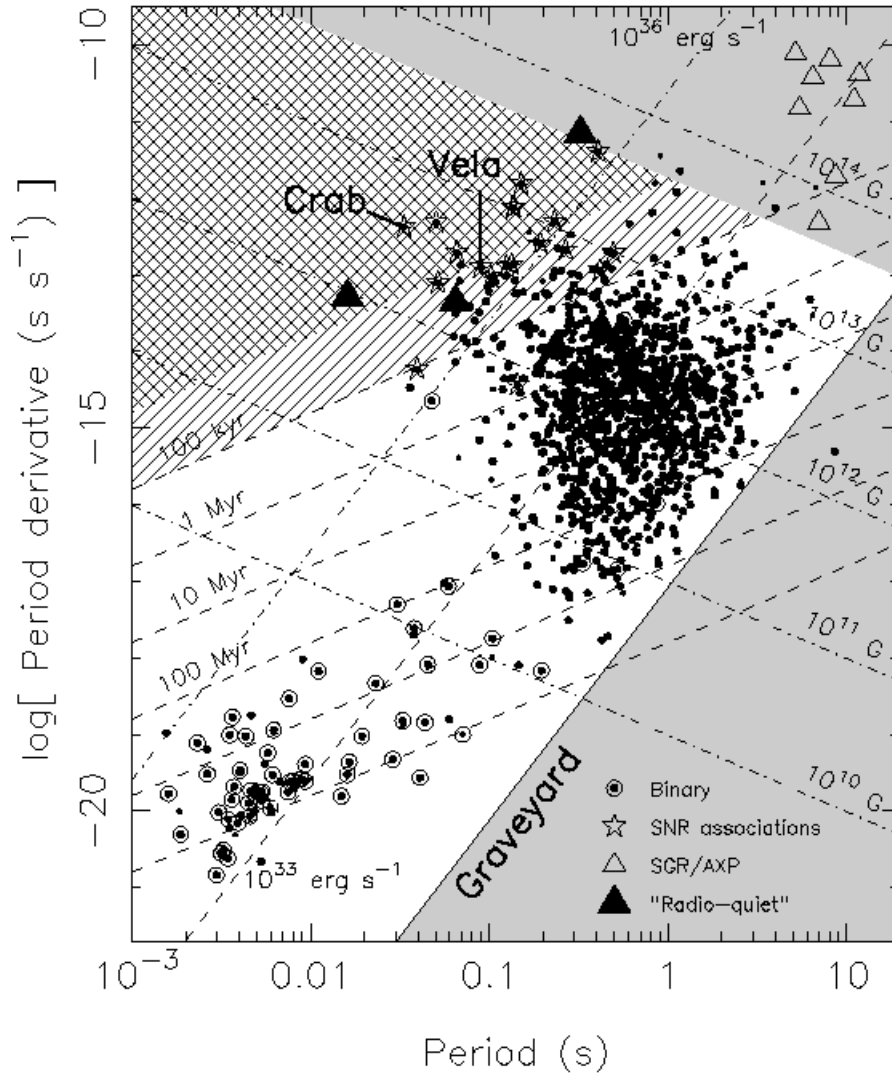
Figure 2.10: $P - \dot{P}$ diagram for radio pulsars, radio-quiet pulsars, Soft Gamma Repeaters and Anomalous X-ray Pulsars. Lines of constant characteristic age, surface magnetic field and spin-down luminosity are shown. Binary pulsars are shown in circles. Pulsars with known SNR associations are shown with stars. The single hashed region shows Vela-like pulsars with age of 10-100 kyr. The double hashed region shows Crab-like pulsars with age less than 10 kyr. The solid line is the "death line" and the grey area is the regions where radio pulsars should not exist.(Lorimer and Kramer 2005)

spin-down luminosity large and the pulsar then slows down very fast. As the pulsar slows down it loses energy at always smaller rates and it eventually approaches the death line. When it reaches

the death line the mechanism responsible for the emission stops working and the pulsar shuts down. It will still be visible in X-rays as a cooling neutron star but when the temperature drops low enough it will become invisible to us.

9 Binary pulsars

The birth and evolution of binary pulsars is much more complex and difficult to predict compared to isolated pulsars because of the mutual interactions. This section is based on a review by van den Heuvel (van den Heuvel 2009).

In every binary system there are 5 points, called *Lagrangian points*, which are at equilibrium respect to the system, the net gravitational force is zero. The points are shown in fig. 2.11. Only two of these points are stable: L_4 and L_5, the others are unstable. The most important of all is L_1 located between the masses. The equipotential surface that passes through this point is called *Roche-Lobe* and it's the key to mass transfer between the stars. If a particle is placed on this surface it is very unstable, a small perturbation could make it collapse on one star or the other. If a star has a strong wind the wind particles crossing this surface will free themselves from the gravitational pull of the parent star and could become bound to the other one.

A more drastic event happens when a star becomes big enough to fill the Roche-Lobe (for example when it reaches the Red Giant Branch or the Asymptotic Giant Branch). In this case the particles on the surface are no more bound to the star and are free to fall on the companion. All the matter that is lost by a star must pass through the Lagrangian point L_1 as if it were a funnel. Because it has angular momentum, it cannot fall directly onto the companion star but will form an accretion disk.

9.1 Accretion on pulsars

The case of a pulsar accreting through an accretion disk is interesting enough to be treated in more detail. As previously said the pulsars have magnetic field lines that are forced to co-rotate with the surface of the star, while the matter in the accretion disk will rotate with a Keplerian velocity profile.

There is a radius at which the magnetic energy density and the gravitational energy density for the accretion disk are equal, this radius is called *Alfven radius*. Outside this radius the accreting matter will be dominated by the gravitational energy and will follow the Keplerian profile. However inside the magnetic fields will dominate and the matter will be forced to follow the magnetic lines and collapse in the polar region of the pulsar.

If the Keplerian velocity at the *Alfven radius* is larger than the rotational velocity of the magnetic field lines (which is the rotational velocity of the pulsar surface), there will be stable accretion. The magnetosphere exerts a torque which slows down the in-falling matter until it reaches the rotational velocity of the pulsar surface. The lost angular momentum is retrieved by the neutron star which is accelerated.

If, on the other hand, the Keplerian velocity at the *Alfven radius* is smaller than the rotational velocity of the magnetic field lines the matter will be pushed away by the centrifugal barrier. This phase is called *propeller* phase.

This means that accreting matter on a pulsar will modify the pulsars velocity of rotation, sometimes even drastically. When enough matter is accreted, a state of equilibrium can be reached where the rotational velocity of the pulsar is the same as the Keplerian velocity at the *Alfven radius*.
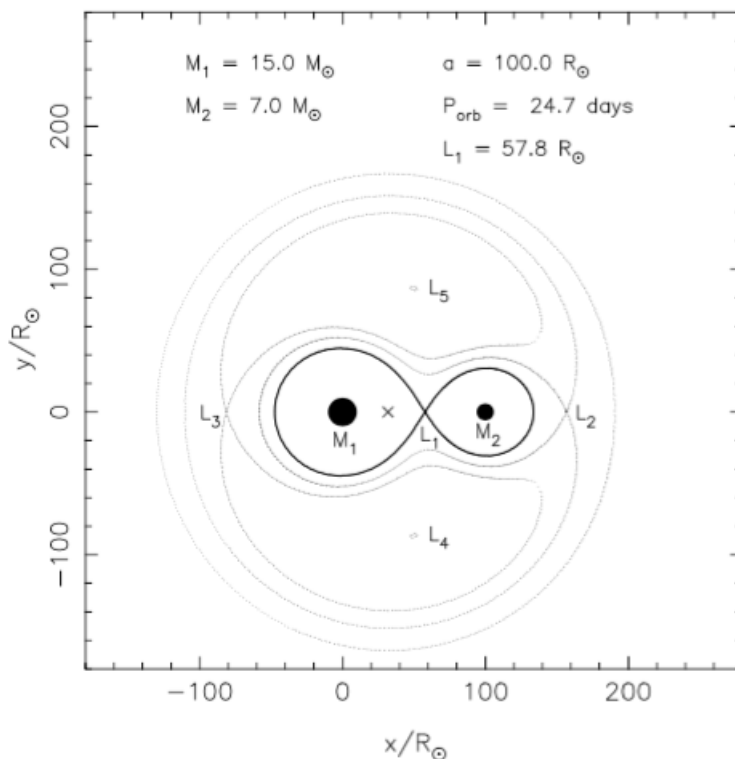
Figure 2.11: A cross section in the equatorial plane of the critical equipotential surfaces in a binary. The points labelled with L are the *Lagrangian points*. The barycenter of the system is indicated by the cross. The curve passing through L_1 is the Roche-Lobe. Figure from van den Heuvel 2009.

Another important but not completely understood effect of accretion on a pulsar is that the magnetic field tends to decrease.

9.2 Evolution of binary systems

Normally stars in a binary system behave the same way they would if they were isolated unless they are forced to interact through exchange of matter.

Depending on the different initial conditions, the evolution and the endpoint of the binaries can vary drastically. I will focus my attention on two types of binaries that will eventually lead to the formation of a neutron star - white dwarf binary and of a neutron star - neutron star binary.

For the first case the initial condition is a binary formed by a very high mass main sequence star and a normal Solar mass star (figure 2.12). The massive star will evolve very fast and enter the Red Giant Branch phase very early on, in this phase it will grow in size enough to fill its Roche-lobe. The envelope of the star will grow so big as to engulf the smaller star, this phase is called common envelope evolution. During the common envelope phase, because of dynamical friction, the smaller star will spiral in towards the core of the bigger star and most of the envelope will be expelled in

outer space. Once all the envelope is removed all that is left is a helium star in tight orbit with a low mass star and most of the mass of the system is lost.

The helium star now evolves rapidly through all the evolutionary phases and explodes as a supernova. If the residual mass of the helium star at the time of the supernova explosion is low enough the explosion is not sufficient to disrupt the system and the binary will survive in a wider and very eccentric orbit. Because the evolution timescale of the low-mass star is very long it has not yet consumed the hydrogen in the core and so the binary will be composed of a neutron star and a low-mass main sequence star.

If the neutron star has its beam pointed towards us we will be able to see a pulsar in an orbit with a low-mass star. The pulsar gradually spins-down beyond the death line and becomes invisible as a pulsating radio source (even though we still might be able to see the thermal emission). This is the phase where, for still unclear reasons, the pulsar should dissipate its magnetic field. When the low-mass star consumes all the hydrogen in the core it starts to burn the hydrogen in the shell and evolves to the Red Giant Branch. It becomes big enough to fill its Roche-lobe and starts accreting on the neutron star emitting in the process X-rays: this phase is called Low Mass X-ray Binary. During this phase the accretion disk spins-up the neutron star turning it into a millisecond pulsar, and because the mass is transferred closer to the barycentre the orbit becomes wider and more circular. When the low-mass star finishes its life (for the chosen mass range following an helium flash) it becomes a white dwarf.

A neutron star - neutron star binary is formed by a very high mass star orbiting another high mass star (but smaller than the first one) (figure 2.13). The highest mass star evolves more rapidly and quickly grows enough to fill its Roche-lobe. When this happens all the envelope is transferred to the second star leaving a naked helium core. The helium star then explodes as a supernova but since most of the mass of the system is now on the other star it does not disrupt the binary, which instead becomes much wider and highly eccentric.

When the second star reaches its Red Giant phase, it fills its Roche-lobe and starts accreting on the neutron star. The accretion process emits high energy X-rays and the system lights up as a High Mass X-ray Binary. The pulsar is rapidly spun up by the process and becomes a millisecond pulsar. Because now the mass is transferred further apart from the barycentre of the system, the binary shrinks rapidly. It shrinks enough that the neutron star is engulfed in the envelope of the second star and starts a common envelope phase. The width of the binary shrinks even further and all the envelope is ejected leaving only the helium core.

When the second star reaches the end of its life and explodes as a supernova the mass ejected is little and the binary can survive the explosion. So at the end the system ends up as a neutron star - neutron star binary in close and eccentric orbit. If both neutron stars are seen as pulsars, as is the case of the Double Pulsar J0737-3039, we see an old millisecond pulsar (the first one to be born) and a young ordinary pulsar.

From the previous scenarios it looks like millisecond pulsars are only found in binaries. While this is true for most of them, it is not for all of them. Excluding pulsars in globular clusters which are in a unique environment in which neutron stars can be expelled from a binary by 3 body encounters, a possibility is that the system disrupted after the explosion of the second star. Another possibility is that the strong relativistic wind of the pulsar is able to vaporise the companion but it is not certain that this is possible with the energetics and timescales involved (Levinson and Eichler 1991).
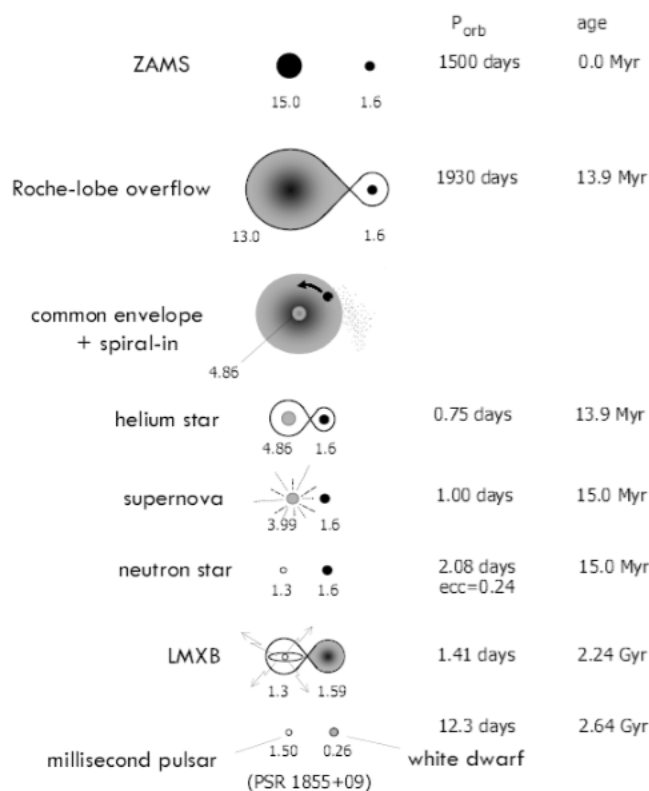
Figure 2.12: Formation process of a neutron star - white dwarf binary starting from a system including a high mass and a low mass main sequence stars. Figure from van den Heuvel 2009.

10   Effects of interstellar matter

The interstellar medium plays an important role in the observation of pulsars. While it has nothing to do with the emission process, it heavily influences the propagation of the signal. In this section I only describe the effects of an homogeneous medium following the description of Lorimer and Kramer in the "Handbook of Pulsar Astronomy" (Lorimer and Kramer 2005).

10.1   Dispersion Measure

The first effect is the dispersion of the pulse at different frequencies. The first to note this effect was Hewish in the paper announcing the discovery of the first pulsar (Hewish et al. 1968) and is so important that if it is not corrected it makes most pulsars undetectable. The effect of the pulse dispersion can be seen in the figure 2.14.

The cause of this effect is the Interstellar Medium (ISM) that is a cold ionised plasma. Electromagnetic radiation, when travelling through a plasma, experiences a frequency-dependant index of

		P$_{orb}$	age
ZAMS	● • 14.4 8.0	100 days	0.0 Myr
Roche-lobe overflow	⬤◗ •⃝ 14.1 8.0	102 days	13.3 Myr
helium star	○ ● 3.5 16.5	416 days	13.3 Myr
1. supernova	☀ ● 3.3 16.5	423 days	15.0 Myr
neutron star	∘ ● 1.4 16.5	5400 days ecc=0.81	15.0 Myr
HMXB	⊙✕⬤ — 1.4 15.0	1300 days	24.6 Myr
common envelope + spiral-in	⊙⬤ 5.0		
	∘ ●	2.6 hrs.	24.6 Myr
helium star RLO	∞○ 1.4 4.1	3.5 hrs.	25.6 Myr
2. supernova	∘ ☀ 1.4 2.6	1.5 hrs.	25.6 Myr
recycled pulsar	— ∘ ∘ — young pulsar 1.4 1.4 (PSR 1913+16)	7.8 hrs. ecc=0.62	25.6 Myr

Figure 2.13: Formation process of a neutron star - neutron binary starting from a system including a very high mass and a high mass main sequence stars. Figure from van den Heuvel 2009.

refraction which, omitting the contribution of the galactic magnetic field, is :

$$\mu = \sqrt{1 - \left(\frac{f_p}{f}\right)^2} \tag{2.14}$$

where f is the observing frequency and f_p is the plasma frequency defined by:

$$f_p = \sqrt{\frac{e^2 n_e}{\pi m_e}} \simeq 8.5\,\mathrm{kHz} \left(\frac{n_e}{\mathrm{cm}^{-3}}\right)^{1/2}. \tag{2.15}$$

In this equation n_e is the number density of electrons and e and m_e are the charge and mass of the electron. For a typical number density of $n_e \sim 0.03\,\mathrm{cm}^{-3}$ (Ables and Manchester 1976) we obtain a plasma frequency of $f_p \simeq 1.5\,\mathrm{kHz}$. So an electromagnetic wave will not propagate if $f < 1.5\,\mathrm{kHz}$ (the index of refraction becomes imaginary) and will propagate almost freely if $f \gg f_p$.
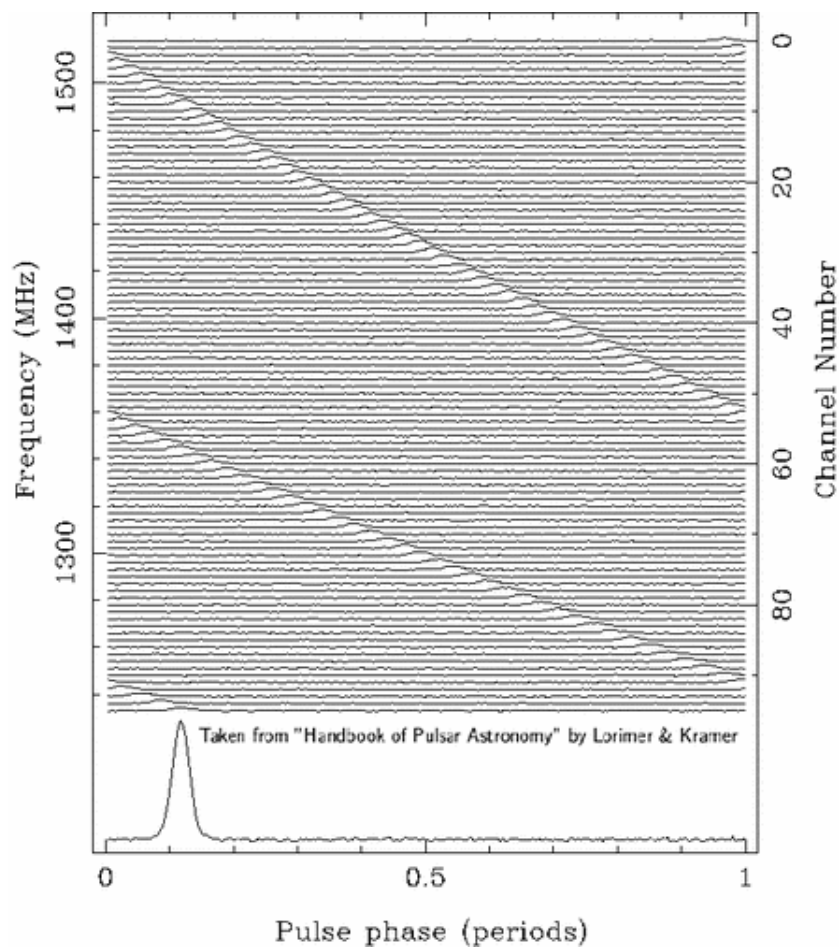
Figure 2.14: Pulse dispersion shown for the pulsar B1356-60. It is evident that if the integrated profile is created without correcting for this effect the pulse would not be visible. Figure from Lorimer and Kramer 2005.

A signal of frequency f will propagate through the interstellar medium with a group velocity $v_g = c\mu$, always smaller than c, and so will be delayed with respect to a signal of infinite frequency along a path of length d by:

$$t = \left(\int_0^d \frac{dl}{v_g} \right) - \frac{d}{c} \tag{2.16}$$

Substituting the values from the previous equations and approximating for $f \gg f_p$ we get:

$$t = \frac{1}{c} \int_0^d \left[1 + \frac{f_p^2}{2f^2} \right] dl - \frac{d}{c} = \frac{e^2}{2\pi m_e c} \frac{\int_o^d n_e dl}{f^2} \equiv \mathcal{D} \times \frac{DM}{f^2} \tag{2.17}$$

Where DM is the dispersion measure, usually expressed in $\mathrm{pc\,cm^{-3}}$, and is given by the formula:

$$DM = \int_0^d n_e dl \tag{2.18}$$

and $\mathcal{D}$ is the dispersion constant:

$$\mathcal{D} \equiv \frac{e^2}{2\pi m_e c} = (4.148808 \pm 0.000003) \times 10^3 \mathrm{MHz^2 pc^{-1} cm^3 s.} \tag{2.19}$$

The uncertainty in $\mathcal{D}$ is given by the uncertainties of e and m_e.
In short the delay in time between two frequencies f_1 and f_2 both in MHz is:

$$\Delta t \simeq 4.15 \times 10^6 \mathrm{ms} \, (\mathrm{f_1^{-2} - f_2^{-2}}) \times \mathrm{DM} \tag{2.20}$$

If the distribution of free electrons along the line of sight is known, the measure of DM can be used to estimate the distance of the pulsar. This measure depends critically on the model of the distribution of free electrons in our galaxy, the most recent example being NE2001 (Cordes and Lazio 2002, 2003). However it seems to underestimate the distance of pulsars close to the galaxy plane.

The delay of a signal can also be expressed in terms of phase rotations. A signal of frequency f compared to a signal of infinite frequency is observed to lag in phase by $\Delta \Psi = kd$ where d is the length travelled and k is the wave number defined by $k = 2\pi/\lambda$. k can be related to the index of refraction through the equation:

$$k = \frac{2\pi}{c} \mu f \tag{2.21}$$

10.2   Faraday rotation and Rotation Measure

Now, if we don't neglect the contribution of the magnetic field, we obtain a frequency-dependant index of refraction for a signal of frequency f of the form:

$$\mu = \sqrt{1 - \left(\frac{f_p}{f}\right)^2 \mp \frac{f_p^2 f_B}{f^3}} \tag{2.22}$$

The cyclotron frequency f_B contains the information of the line of sight component of the magnetic field through the equation:

$$f_B = \frac{eB_\parallel}{2\pi m_e c} \simeq 3\mathrm{MHz} \left(\frac{B_\parallel}{G}\right) \tag{2.23}$$

For the Galaxy $B_\parallel \sim 1\mu G$ so for the ISM we expect $f_B \sim 3\mathrm{Hz}$.

In a magnetised plasma there is also another effect that we neglected until now: radiation polarised in different directions propagate at different speeds (the same effect can be observed on Earth with birefringent crystals). This is contained in the equation 2.22 as follows: the left-hand circularly polarised radiation has the minus sign while the right-hand circularly polarised radiation has the plus sign.

The difference in arrival times for the different polarisations is $\sim 1\mathrm{ns}$, too small to be measured even by modern day observatories (but might be achievable for the next generation of radio

telescopes). However it is high enough to rotate the polarisation position angle of a source by a discernible amount. This rotation in polarisation is called *Faraday rotation.*

The differential phase rotation between left and right circularly polarised radiation along a path of length d is:

$$\Delta\Psi_{Faraday} = \int_0^d (k_R - k_L)dl \tag{2.24}$$

where k_R and k_L are the wave numbers of the right and left circularly polarised radiation. If we assume (as is always our case) that $f \gg f_p$ and $f \gg f_B$, we can express the rotation as:

$$\Delta\Psi_{Faraday} = \frac{e^3}{\pi m_e^2 c^2 f^2} \int_0^d n_e B_\parallel dl \tag{2.25}$$

If we express the same equation for the Polarisation Position Angle (PPA), which is periodic on π rather than 2π, we obtain:

$$\Delta\Psi_{PPA} = \Delta\Psi_{Faraday}/2 = \lambda^2 \times RM \tag{2.26}$$

where λ is the wavelength and RM is called *rotation measure* and is defined as:

$$RM = \frac{e^3}{2\pi m_e^2 c^4} \int_0^d n_e B_\parallel dl \tag{2.27}$$

10.3   Interstellar magnetic fields

Once we have estimated the DM and the RM of a pulsar we can probe the average magnetic field along the line of sight through the relation:

$$\langle B_\parallel \rangle = \frac{\int_0^d n_e B_\parallel dl}{\int_0^d n_e dl} = 1.23\,\mu G \left(\frac{RM}{\mathrm{rad\,m^{-2}}}\right) \left(\frac{DM}{\mathrm{cm^{-3}\,pc}}\right)^{-1} \tag{2.28}$$

It is also possible to measure the average intensity of the magnetic field in the intermediate region between pairs of pulsars, if the line of sights are close enough to each other, by using the formula (first suggested by Lyne and Smith 1989):

$$\langle B_\parallel \rangle_{d_1 - d_2} = 1.23 \frac{\Delta RM}{\Delta DM} \mu G \tag{2.29}$$

where d_1 and d_2 are the distances of the sources from the Sun and ΔRM and ΔDM are the differences between rotation measures and dispersion measures of the two pulsars.

If other parameters of the pulsars like the position and distance (measured mostly through models of free electrons distribution in our Galaxy) are known it is possible to create a model of the galactic magnetic field. This has been done extensively and various models from the simplest to more complex ones have been proposed and tested from the first years of pulsar observations to the recent period (Manchester 1972, Manchester and Taylor 1977, Lyne and Smith 1989, Noutsos et al. 2008, Tiburzi et al. 2013).

Chapter 3

Globular clusters

1 General description

Globular clusters are gravitationally bound spherical stellar systems typically very old (~ 10 Gyr), massive ($\sim 10^5 M_\odot$) and with low metallicity. They are commonly found in the halo or bulge of galaxies. There are more than 150 globular clusters orbiting the Milky Way Galaxy. Their dimensions are typically some tens of parsecs across and the stellar densities are very big especially in the center ($\sim 10^3 - 10^5 \text{pc}^{-3}$). A key difference between globular clusters and dwarf galaxies is the absence of star-formation and likely of measurable concentrations of dark matter. Two examples of globular clusters are shown in figure 3.1.
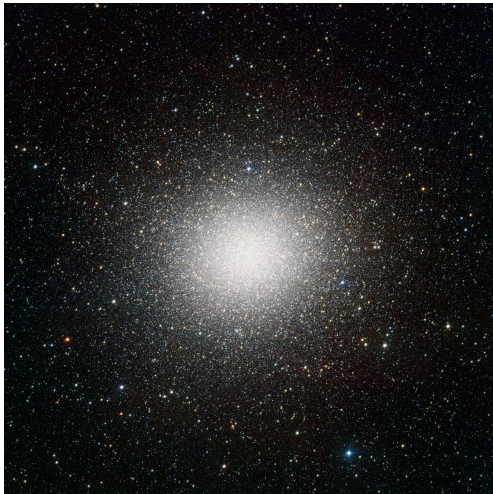
(a) Omega Centauri. Image from VST. Credits: ESO/INAF-VST/OmegaCAM

(b) M15. Image from Hubble space Telescope. Credits: NASA/ESA

Figure 3.1: Examples of globular clusters.

This definition of globular clusters is the one usually given but since it is possible to find exceptions to almost all criteria a more general definition may be: "A gravitationally-bound, stellar cluster that in terms of its position and velocity vectors does not coincide with the presently star-forming component of its host galaxy" (Kruijssen 2015). The term "stellar cluster" excludes dark-matter dominated systems like dwarf galaxies. A globular cluster can pass through the star-forming regions of the galaxy but the velocity component will be different.

The population of globular clusters in the Galaxy appears to be divided in two subsystems, one rapidly rotating in the bulge near the center of the Galaxy and the other slowly rotating in the spherical halo.

An important parameter in the classification of globular clusters is the metallicity. It is usually smaller than the solar one because these stars are supposed to be some of the oldest in the universe and the environment at the time of formation was not very polluted from past generations of stars. The metallicity is usually given as $[Fe/H]$ which is the logarithm of the abundance of iron compared to that of hydrogen normalized to the Solar system value and is typically bimodal peaking at $[Fe/H] \sim -1.6$ and $[Fe/H] \sim -0.6$ (Meylan and Heggie 1997).

1.1 Color-Magnitude diagram
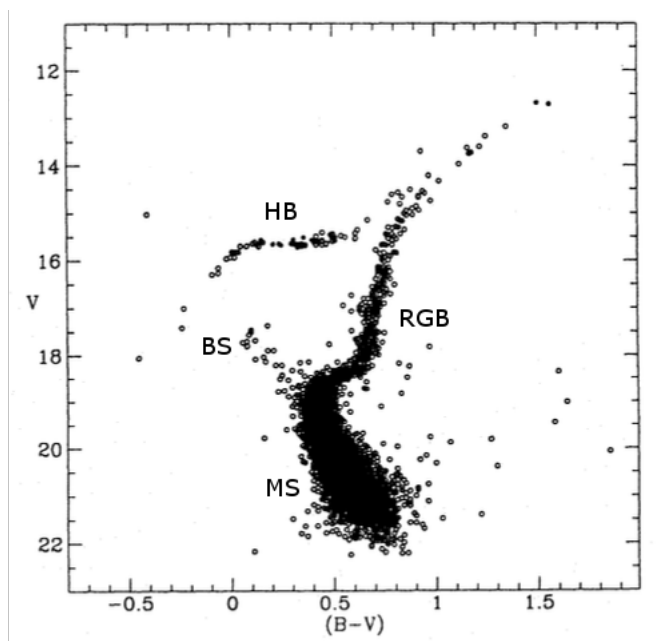
Figure 3.2: CM diagram of stars from the globular cluster M3. Data from Buonanno et al. 1994.

The Color-Magnitude (CM) diagram of the stars in globular clusters is very peculiar (fig. 3.2) if confronted with CM diagram of stars in the Galaxy. The Main Sequence (called MS in fig. 3.2) is populated only in the low mass region and has a clear turnoff, the point at which happens is then called turnoff point. The few stars along the main sequence above this turnoff are called

Blue Stragglers (BS). A large number of stars connect the interrupted main sequence with the Red Giant Branch (RGB) which is very narrow. Above the main sequence, and very clearly visible, is the extended Horizontal Branch (HB).

The common interpretation of these kind of diagrams is that the globular cluster is formed by a single population of stars born at the same epoch. Since more massive stars evolve faster out of the main sequence than less massive ones, the position of the turnoff point gives us an indication of the age of the cluster. By fitting the observed main sequence with theoretical ones we can find the approximate distance of the cluster (a more precise way would be to use the RR-Lyrae variables as distance estimators) and the age of the main sequence stars at the turnoff point. This estimate of the age is not very precise as it depend on the distance estimate, a better way would be to find a distance independent method of calculating the age. One way is to calculate the difference in magnitude between the horizontal branch and the turnoff point (ΔV method) or to calculate the difference in color between the turnoff point and the red giant branch ($\Delta(B-V)$ method) (Binney and Merrifield 1998).

If the star-formation only happens during the birth of the cluster the presence of the blue stragglers stars poses a problem. These stars are more massive than the average star in the cluster and should have already evolved out of the main sequence and ended their lives as white dwarf. The common explanation is that they were formed later in the life of the cluster after mass transfer from a companion in a binary system or from mergers induced by collisions (Ferraro et al. 2015).

Recently more precise measurements have found that some globular clusters have actually multiple populations of stars (Conroy and Spergel 2011, Milone et al. 2012) an example is shown in fig. 3.3.
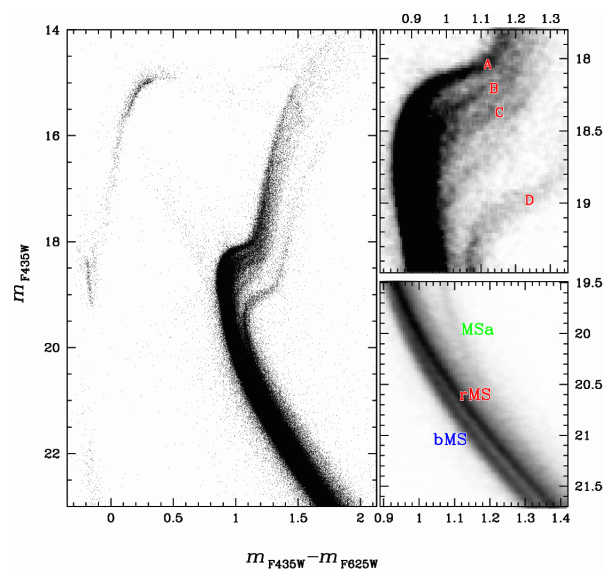
Figure 3.3: CM diagram of stars from the globular cluster ω Centauri. On the right the zoomed parts of the diagram show multiple turnoff points. Figure from Bellini et al. 2010.

1.2 Radial profile

The globular clusters appear very symmetrical and their stellar density profile can be described using only the radius. A model that seems to fit the radial profile well is the King model (King 1966) as can be seen from figure 3.4. The King model is based on the radial density of an isothermal sphere model but is truncated at an external radius called the tidal radius r_t. The other important parameters for this model are the central surface brightness (or density if the mass to light ratio is known) and the core radius, r_c, defined to be the radius at which the surface brightness has fallen to half of its central value. The concentration $c = \log(r_t/r_c)$ is a useful distance indipendent measure of the cluster morphology. (Binney and Merrifield 1998, Binney and Tremaine 2008). Another model that sometimes is used is the Plummer profile (Plummer 1911).
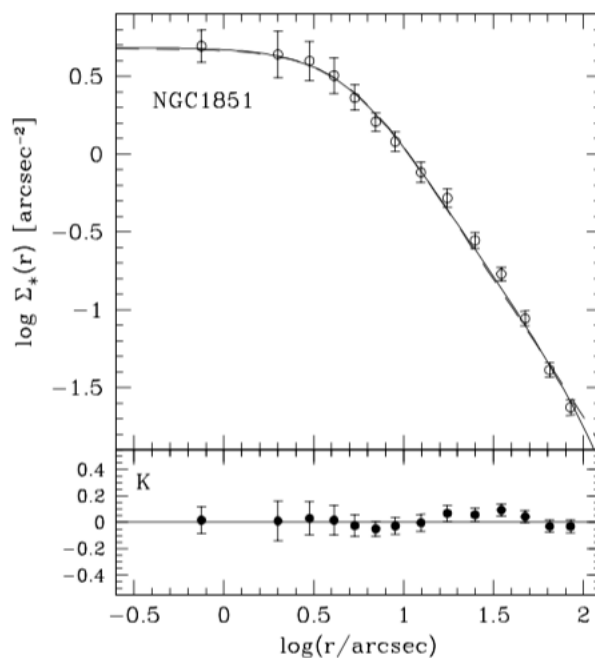
Figure 3.4: Radial profile of the globular cluster NGC 1851. The solid line represents the best King model. The panel below shows the deviations of the observed data to the model. Figure from Miocchi et al. 2013.

2 Dynamics

The dynamics of a star in a stellar system is determined by two components: the gravitational interaction with the collective potential of the cluster and the gravitational interactions with single stars. Single interactions with stars usually don't modify significantly the dynamics of a sample star but, over some time, their cumulated effect can strongly affect the orbits. The sum of all the

interactions necessary to distort the orbit of a sample star so much that it loses memory of the original direction of the velocity is called a *collision*.

The time needed to make a collision in the sense indicated above is called the *relaxation time*. After this time has passed all the stars have modified their orbit in a way that it's impossible to reconstruct the original velocity distribution of the cluster. This time, for a population of stars of equal mass m, density n and velocity dispersion σ, can be expressed as: (Colpi and Devecchi 2009)

$$t_r = 0.34 \frac{\sigma^3}{G^2 m^2 n \ln \Lambda}, \tag{3.1}$$

where $\ln \Lambda \sim 10$ is the Coulomb logarithm.

If the relaxation time is shorter than the life time of the stellar system, the system is called *collisional*. Globular clusters have relaxation times of $10^8 - 10^9$ yr calculated at the half-mass radius and of 10^6 yr calculated at the core radius. This values confronted with their life-times of 10^{10} yr show that globular clusters are very collisional systems. This means that interactions between stars are very important and have to be considered when evaluating the dynamical history of the cluster. The next parts follow the description of Colpi and Devecchi (2009).

2.1   Core collapse in single-mass clusters

Stellar interactions can be separated in two classes: distant encounters, that induce small and repeated changes in the energy content of the star, and close encounters, that can modify significantly the energy in a single encounter. These encounters can cause stars to leave the cluster in two ways: *evaporation*, where a series of distant encounters gradually increase the energy until it becomes positive, and *ejection*, where a single close encounter gives enough energy to a star to escape.

The evolution of a single-mass globular cluster leads to a collapse of the core in two phases. In the first phase a lot of encounters occur especially in the very dense core, this leads to mass-loss through evaporation and stars are driven in the outer parts of the cluster. Because of energy conservation and the virial theorem, as the outer part expands, the core must contract and heat up. When the core becomes so dense that the local relaxation time is much smaller than it is in the rest of the cluster, it decouples dynamically and becomes unable to transfer heat to the halo. At this point starts the second phase of evolution where the core becomes isothermal and keeps contracting until it becomes singular at the center (like in the singular isothermal sphere). The situation of an infinite density in the core is never reached because of the role played by close encounters with binary stars.

2.2   Mass segregation in multiple component clusters

In real clusters however stars have different masses and this leads to another important process in globular clusters, *mass segregation*. Mass segregation is the result of the equipartition of kinetic energy reached by stars of different masses. Since more massive stars have more kinetic energy than lower mass stars on the same orbit, the interactions cause massive stars to lose energy and fall in the center while lighter stars gain energy and move in the outer parts of the cluster. As this process keeps going, in the core we are left with only massive stars while the halo is populated only by lighter stars, i. e. spatial segregation sets in. When this happens the core tends to only contain a single mass population of stars and is unstable to core collapse. The first to note this instability was Spitzer and so it is usually referred to as the "Spitzer Instability" (Spitzer 1987).

2.3   Close encounters and binary systems

A solution to the core collapse can be found considering the role of close encounters with binary stars. Binary stars can be primordial (plausible considering that almost 50% of stars in the Galaxy disk are born in binaries) or of dynamical origin, forming from a three body encounter of a single star and a binary. Since binary systems are heavier than single stars they tend to segregate to the very dense center in which, thanks also to the large gravitational cross section, close encounters with single stars are very common.

The end-states of three body encounters involving a binary can be classified in: *fly-by*, in which the end-state is identical to the original one with different energy values; *exchange*, in which the single star takes the place of one of the binary stars; *ionisation*, in which the binary separates and the three stars become unbound; *merger*, in which the two binary stars are brought so close that they coalesce; *triplet*, in which the three stars form an unstable bound system.

Contrary to what happens in single-single interactions, during single-binary fly-by interactions there can be an energy exchange between the components. This is because binary systems have an internal degree of freedom parametrised by the semi-major axis of the binary which can change during encounters releasing or absorbing energy to the other star. Binary systems in encounters can be classified as *soft binary* if the kinetic energy of the incoming star is greater than the internal kinetic energy of the binary or *hard binary* if the opposite is true.

In the case of soft binaries the system tends to absorb some of the energy of the incoming star becoming wider so a common saying is that *soft binaries become softer*. In the case of hard binaries is the opposite, the system tend to release energy to the incoming star becoming tighter, in this case the saying goes *hard binaries become harder*.

From these considerations is clear that wide binaries tend to become even wider and less bound leading to an eventual ionisation of the system while tight binaries tend to become more bound and to release even more energy in the cluster. The presence of even a few hard binaries in the core of the cluster can release enough energy as to mix the populations of stars and even stop the collapse of the core altogether.

In exchange interactions, where the incoming star takes the place of one component of the binary, if stars have unequal masses the most probable end-state is the one where the binary is composed by the two heavier stars.

Following these considerations when looking at very relaxed globular clusters we expect to find the binaries closer to the core and composed of the heaviest stars.

3   Pulsars in GC

Globular clusters appear to be good candidates for the search of pulsars because of the high stellar densities, the fact that the central regions could be observed with a single pointing of the radio telescope and the large number of LMXB found. Another attractive feature of these objects is the fact that the dispersion measure varies slightly in the same cluster so the search procedure could be made more efficient limiting the range of possible DM.

The main problems which limited the early discoveries were mainly due to the large computation power required. Since the clusters are very far, a much longer observation time is needed to find even the brightest pulsars and this increases the complexity of data reduction. Another problem is that a large fraction of pulsar are binaries and the observed period can change significantly during

the long integration times. In order to find such pulsars a search at various accelerations is needed and this requires a lot of computations (Camilo et al. 2000).

Thanks to the new radio telescopes, receivers, advanced hardware and dedicated sotware, 146 pulsars have been discovered in 28 globular clusters.[1] With the record of 34 pulsars in the globular cluster Terzan 5. These pulsars differ from those in the galaxy disk because they are much older, almost all are recycled millisecond pulsars. This is to be expected as they formed in the very early evolutionary stages of the cluster and since they are more massive than the average star population observed nowadays they are likely to have spent some time in a binary system and therefore have been recycled (Freire 2013).
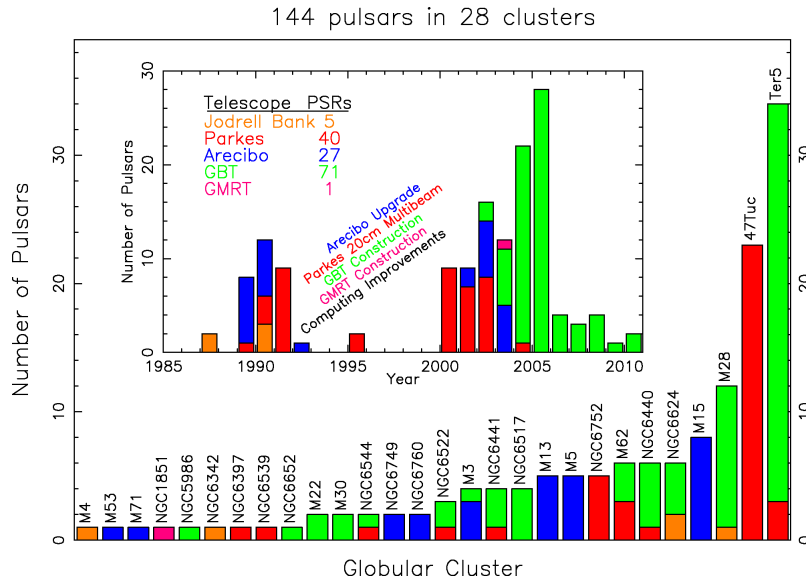
Figure 3.5: Numbers of pulsars found in each globular cluster. The color shows the telescope with which they were discovered and the insert shows the year of their discovery. Figure from http://www.naic.edu/∼pfreire/GCpsr.html.

The population of millisecond pulsars in globular clusters is very peculiar also because of the high number of exotic pulsars not common in the disk. These pulsars can have very high eccentricity, due to the chaotic environment of the cluster cores. There are many eclipsing binaries and binaries with low mass main sequence companions called "Redbacks".

With precise timing procedures it is possible to find the exact position of the pulsars in the cluster and the results show that most of them are concentrated in the center around the core radius as suggested by the mass segregation. (3.6)

---

[1]An updated count with main properties given for every pulsar and reference list can be found on http://www.naic.edu/∼pfreire/GCpsr.html
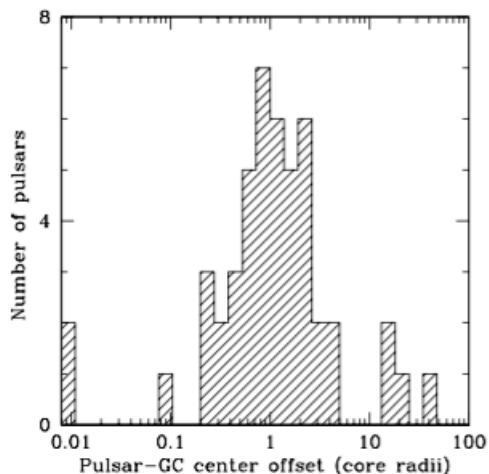
Figure 3.6: Histogram of 48 pulsar showing the angular offset in units of core radius of the cluster. Figure from Camilo and Rasio 2005.

3.1   Formation and evolution

An important characteristic of the globular clusters is the abundance of pulsars and of their progenitors, the X-ray binaries, which appear to be two or three orders of magnitude more numerous per unit mass than the population in the Galaxy disk. This fact is surprising as in the normal scenario, presented in the previous chapter, pulsars form from core-collapse supernovae (CCS) and usually receive kicks larger than a few hundreds kilometres per second, which is faster than the escape velocity of the typical cluster. According to this there shouldn't be any neutron star left. Even if the CCS happen in binaries with a massive companion which could anchor the neutron star to the system only a small fraction should remain (Freire 2013).

There are however different methods for forming a neutron star that do not involve high kick velocities. One way is the "electron capture" supernova (ECS) which happens when the degenerate ONeMg core reaches a critical mass $M_{ECS} = 1.38 M_\odot$ and electron capture happens before the nuclear burning can form an iron core (Colpi and Devecchi 2009). The energy released and natal kick received in this kind of explosion are much smaller than the ones in CCS so the neutron star can remain in the cluster. For single stars this channel is open only in the mass window between $8 - 10 M_\odot$ while for binary stars there can be other ways to achieve an ECS. One way is a ONeMg white dwarf driven above the mass limit by accretion, called accretion induced collapse (AIC). Another way is a merger of two white dwarfs with total mass above the limit, called merging induced collapse (MIC).

As suggested by Colpi and Devecchi (2009) in GCs very few of the pulsars formed in binaries remain in the same binaries. The explanation for the very diverse population observed can be found in the close encounters in the very dense core. Very important are the exchange interactions where the neutron star can take the place of another star in a binary system. This way we can explain the strange observed systems like the "redbacks" and the eclipsing binaries. Other rare systems have been observed like a double neutron star system (Prince et al. 1991) and a triple system with

a white dwarf and a Jupiter-mass planet companion (Thorsett et al. 1999, Sigurdsson et al. 2003).

3.2 Science with pulsars in globular clusters

Globular clusters are therefore very interesting objects for the the study of pulsars with their very rich and diverse population. The knowledge that can be gained by studying these objects mainly falls in two classes: peculiar individual systems which can be used to investigate fundamental physics; and the investigation of the properties of the globular cluster using the collective population of pulsars (Hessels et al. 2015).

Peculiar individual systems

Some of the fastest spinning neutron stars, including the fastest known with a period of 1.39 ms in Terzan 5 (Hessels et al. 2006), are in globular clusters. Pulsars in GCs can in theory experience multiple recycling episodes achieving record rotation rates. Further search for this objects might find even faster stars perhaps even breaking the millisecond limit.

Because of the high eccentricity of the binaries in the clusters it is easier to measure the periastron advance of the orbit which can be used to measure the mass of the neutron star. Globular cluster pulsars are thought to be very massive because of the prolonged and/or multiple accretion stages. Further precise observations can measure masses of more neutron stars mapping their distribution especially at high masses. Finding the highest possible masses can give tighter constrains on the equation-of-state (Antoniadis et al. 2013).

The observation and discovery of new exotic pulsars can give us a better idea of how these neutron stars have formed and evolved. For example, apparently young pulsars have been discovered in some globular clusters suggesting that such stars can form nowadays or that there is some process to rejuvenate them (Lyne et al. 1996). Another kind of strange systems present in globular clusters are the binaries with main sequence companions and the eclipsing binaries both of which could tell us more about the possible evolutionary processes.

Because of the very dynamic environment of the clusters all kinds of binaries could form including some possible millisecond pulsar - millisecond pulsar binary or millisecond pulsar - black hole binary. These system could help us understanding how such objects curve the spacetime and providing tests of general relativity in a regime where it has never been tested before. No such object is currently known but if they exist globular clusters are the best place to look for them (Clausen et al. 2014).

General properties of clusters

The study of the acceleration imparted to the pulsars can be used to probe the gravitational potential of the cluster. Also it may be possible to check the presence of an intermediate-mass black hole (IMBH) at the center through studies of nearby pulsars or even pulsars in a binary system with the IMBH (Devecchi et al. 2007). The accurate determination of the proper motion of the neutron stars can be used to measure the proper motion of the cluster in the Galactic halo. These observations together with optical studies can be used to model the gravitational potential in the halo of the Galaxy.

In each cluster the type of pulsars found, the location, the fraction of binaries and the companions can vary a lot. This could be due to the different dynamical histories of the cluster (Verbunt and Freire 2014) and can help us better understanding some stages of evolution like the process of core-collapse.

The precise measure of the dispersion and rotation measures (DM and RM) of the pulsars can be used to detect the ionized part of the intra-cluster medium (Freire et al. 2001b) and its magnetic field. From these measurements it could be possible to study the origin and the evolution of the gas in the cluster.

4   Intracluster Medium

The interstellar medium in globular clusters, or intracluster medium (ICM), has evaded observations for a long time (Naiman et al. 2013). Such gas should build up in the clusters because of mass loss from main sequence stars, red giants and horizontal branch stars. Stars on the RGB or the AGB are expected to lose $\sim 10^{-9} - 10^{-8} M_{\odot} \, \mathrm{yr}^{-1}$ (Dupree et al. 2009) and summing the contribution of all dust there should be $\dot{M} \sim 10^{-6} M_{\odot} \, \mathrm{yr}^{-1}$ of dust (McDonald et al. 2011). With such rates of predicted mass loss acting on the long lives of the globular clusters a lot of ICM is expected unless there are some efficient evacuation mechanisms.

Recent submillimeter and infrared searches for dust have only given upper limits of $\leq 4{\times}10^{-4} M_{\odot}$ (Barmby et al. 2009), orders of magnitude less than what expected from the stellar population. Searches for the CO rotational energy level at 2.6 mm were not more successful finding upper limits of about $0.1 M_{\odot}$ (Leon and Combes 1996). A possible detection of two CO lines was found towards the globular cluster 47 Tucanae (Origlia et al. 1997) but more recent observations with ALMA did not confirm it (McDonald et al. 2015). Observations of neutral hydrogen at 21 cm were, with a few exceptions, also unsuccessful and found upper limits of a few solar masses (van Loon et al. 2006). The most reliable constraint on the presence of ICM is the measure of ionized gas with a density of $n_e = 0.067 \pm 0.015 \, \mathrm{cm}^{-3}$ obtained through the study of dispersion measures of millisecond pulsars in the globular cluster 47 Tucanae (Freire et al. 2001b).

Different mechanisms for removing the ICM efficiently have been proposed (McDonald and Zijlstra 2015), some external and some internal. When the globular clusters cross the galactic plane ram pressure stripping can remove all of the gas but this happens only every $\sim 10^8$ yr. Another external evacuation process is ram pressure stripping as the cluster passes through the Galactic halo but the density of the halo is one order of magnitude too low for this process to be effective on bigger clusters (Frank and Gisler 1976); more precise simulations confirmed that only clusters with masses $\leq 10^5 M_{\odot}$ can be cleared of gas in this way (Priestley et al. 2011).

Internal evacuation mechanisms can be divided in impulsive phenomena and continuous ones. Different impulsive phenomena have been proposed like stellar collisions (Chatterjee et al. 2008) which are too unfrequent to efficiently clear the ICM, and novae (Scott and Durisen 1978) which could work only on small clusters. Some continuous processes to evacuate the gas are the radiation from pulsar winds (Spergel 1991), main sequence stellar winds (Naiman et al. 2013) and fast winds from red giants (Smith et al. 2004).

5   47 Tucanae

The globular cluster 47 Tucanae (NGC 104) is the second brightest in the sky with an absolute magnitude in optical of -9.26 (Binney and Merrifield 1998) and is one of the closest to the Sun. It's luminous enough to be visible to the naked eye and the name comes from the fact that it was misinterpreted as a star in the constellation Tucana. All the important properties of this globular cluster are in the table 3.1.

Parameter	Value	Notes and references
Center RA (J2000)	$00^h24^m05^s.67 \pm 0^s.07$	McLaughlin et al. 2006
Center Dec (J2000)	$-72°04'52".62 \pm 0".26$	McLaughlin et al. 2006
Distance from Sun	(4.5 ± 0.2) kpc	Harris 2010
Distance from galactic center	7.4 kpc	Harris 2010
Mass	$(1.1 \pm 0.1) \times 10^6 M_\odot$	Lane et al. 2010
Metallicity $[Fe/H]$	-0.76	Harris 2010
Tidal radius	42'.3 (55.4 pc)	Harris 2010
Half mass radius	(7.8 ± 0.9) pc	Lane et al. 2010
Core radius	21".6 (0.5 pc)	Harris 2010
Age	(10.0 ± 0.4) Gyr	Gratton et al. 1997
Core relaxation time	$(7.1 \pm 1.1) \times 10^7$ yr	Bianchini et al. 2013
Time since galactic plane crossing	6×10^7 yr	Odenkirchen et al. 1997
Sound travel time	~ 4.3 Myr	McDonald and Zijlstra 2015
Heliocentric radial velocity	(-18.0 ± 0.1) km/s	Harris 2010
Proper motion in RA $\mu_\alpha cos\delta$	$(+7.26 \pm 0.03)$ mas/yr (~ 150 km/s)	Cioni et al. 2016
Proper motion in Dec μ_δ	(-1.25 ± 0.03) mas/yr (~ -26 km/s)	Cioni et al. 2016
Escape velocity at the core	68.8 km/s	Gnedin et al. 2002
Velocity dispersion	13.06 ± 1.00 km/s	Bianchini et al. 2013
Central density	$\sim 1 \times 10^5 M_\odot \, pc^{-3}$	Pryor and Meylan 1993, Bianchini et al. 2013
Central ICM density	$(0.067 \pm 0.015) \, cm^{-3}$	Freire et al. 2001b
Surrounding halo density	$\sim 0.007 \, cm^{-3}$	Taylor and Cordes 1993

Table 3.1: Main properties of the globular cluster 47 Tuc.

The cluster is not perfectly spherical but presents an ellipticity of 0.16 ± 0.02 (Chen and Chen 2010) and presents a rotation with velocity ~ 4 km/s along an axis with an angle of 136° measured from the north (Bianchini et al. 2013). See figure (3.7).

Precise photometric studies (Milone et al. 2012) have revealed that in the cluster there is a second generation of stars slightly younger than the first. Models like that of Ventura et al. (2014) show that this second generation of stars has been formed from AGBs ejecta and pristine gas driven into the cluster by a cooling flow. This process continued for almost 100 Myr and then stopped because the explosions of SN Ia ejected all the gas from the cluster. In the same paper it is also estimated that at birth the cluster was about 7.5 times more massive than it is now and that a large fraction of first generation stars left the cluster during the early evolution.

5.1 Pulsars in 47 Tucanae

The globular cluster 47 Tucanae has been subject of numerous searches and studies of pulsars with impressive results (Manchester et al. 1991, Robinson et al. 1995, Camilo et al. 2000, Freire et al. 2001a,b, 2003). Up to now there have been found 25 pulsars (Pan et al. 2016) and for 22 of them was found a timing solution[2]. The timing solutions used for our observations were derived by Ridolfi et al. (in prep.) and are presented in the table 3.2.

---

[2]an up to date list of the timing solutions can be found at http://www3.mpifr-bonn.mpg.de/staff/pfreire/47Tuc/

Name	RA	DEC	F0	F1	DM	PM RA	PM DEC	Binary
J0023-7204C	00:23:50.35477(3)	-72:04:31.50466(1)	173.708218	$1.50420(2) \times 10^{-15}$	24.600(1)	5.30(3)	-3.14(3)	no
J0024-7204D	00:24:13.88092(3)	-72:04:43.8524(1)	186.651669	$1.1921(3) \times 10^{-16}$	24.7319(8)	4.23(3)	-2.24(3)	no
J0024-7205E	00:24:11.10308(7)	-72:05:20.1453(2)	282.779107	$-7.87746(6) \times 10^{-15}$	24.23637(8)	6.14(5)	-2.36(5)	yes
J0024-7204F	00:24:03.85546(5)	-72:04:42.8183(2)	381.158663	$-9.37113(9) \times 10^{-15}$	24.382(1)	4.52(5)	-2.49(6)	no
J0024-7204G	00:24:07.9602(1)	-72:04:39.7028(4)	247.501525	$2.5825(1) \times 10^{-15}$	24.436(3)	4.5(1)	-2.9(1)	no
J0024-7204H	00:24:06.7031(1)	-72:04:06.8068(5)	311.493417	$1.773(1) \times 10^{-16}$	24.368(3)	5.2(1)	-2.8(1)	yes
J0024-7204I	00:24:07.9348(1)	-72:04:39.6809(4)	286.944699	$3.7771(1) \times 10^{-15}$	24.429(4)	4.9(1)	-2.3(1)	yes
J0023-7203J	00:23:59.40762(1)	-72:03:58.79077(4)	476.046858	$2.21934(3) \times 10^{-15}$	24.5879(3)	5.29(1)	-3.61(1)	yes
J0024-7204L	00:24:03.7719(3)	-72:04:56.9239(9)	230.087746	$6.46087(5) \times 10^{-15}$	24.399(4)	4.5(2)	-2.2(2)	no
J0024-7204M	00:23:54.4900(3)	-72:05:30.7571(9)	271.987228	$2.8431(1) \times^{-15}$	24.432(6)	5.1(3)	-2.1(3)	no
J0024-7204N	00:24:09.1878(1)	-72:04:28.8911(7)	327.444318	$2.3435(2) \times 10^{-15}$	24.573(5)	6.4(2)	-2.7(2)	no
J0024-7204O	00:24:04.65256(5)	-72:04:53.7667(2)	378.308788	$-4.34376(8) \times 10^{-15}$	24.356(2)	5.03(5)	-2.59(6)	yes
J0024-7204Q	00:24:16.4908(1)	-72:04:25.1642(6)	247.943237	$-2.09065(3) \times 10^{-15}$	24.266(3)	5.2(2)	-2.6(1)	yes
J0024-7204R	00:24:07.5851(1)	-72:04:50.3952(7)	287.318119	$-1.22467(3) \times 10^{-14}$	24.361(3)	4.8(2)	-3.4(2)	yes
J0024-7204S	00:24:03.9795(1)	-72:04:42.3529(4)	353.306209	$1.50465(1) \times 10^{-14}$	24.376(2)	4.4(1)	-2.6(1)	yes
J0024-7204T	00:24:08.5488(5)	-72:04:38.932(2)	131.778699	$-5.10254(6) \times 10^{-15}$	24.39(1)	5.4(5)	-2.5(6)	yes
J0023-7203U	00:24:09.83654(7)	-72:03:59.6881(3)	230.264772	$-5.04915(7) \times 10^{-15}$	24.337(2)	4.59(8)	-3.8(1)	yes
J0024-7204Y	00:24:01.40252(1)	-72:04:41.8365(4)	455.237178	$7.2890(1) \times 10^{-15}$	24.468(2)	4.4(1)	-3.4(1)	yes

Table 3.2: Timing solutions for the pulsars in 47 Tucanae detected in the observations. The column RA is the right ascension expressed in the form hh:mm:ss, while the column DEC is the declination written in the form dd:mm:ss. F0 is the spin frequency expressed in Hz. F1 is the derivative of the frequency and is in units of s^{-2}. DM is the dispersion measure expressed in pc/cm^3. PM RA and PM DEC are the right ascension and declination of the proper motion and are both expressed in arcseconds. The last column shows which pulsars are in a binary system. The numbers in the parentheses are the errors on the last digit. For the spin frequency I cut the number of significant figures to 9 to facilitate the reading.
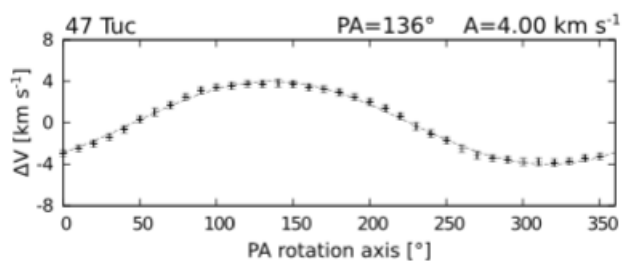
Figure 3.7: Difference between the average stellar velocities calculated on each side of the system divided by a line passing through the center with a given position angle, P.A. The P.A. at which the maximum difference is reached corresponds to the position of the rotation axis. The best-fit sine function is plotted (solid line) and the corresponding P.A. and amplitude A are indicated. Figure from Bianchini et al. 2013.
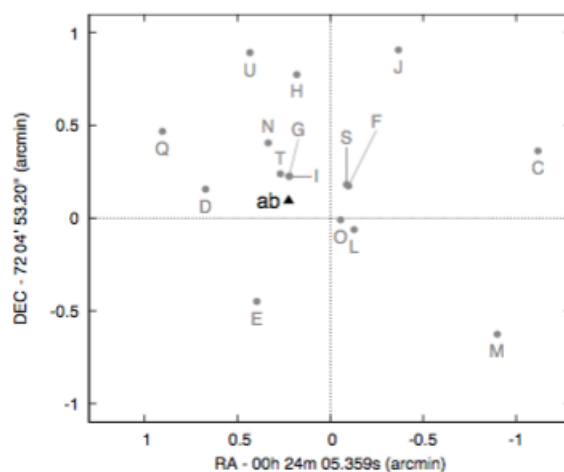
Figure 3.8: Position of the pulsars in 47 Tucanae with known timing solutions. The center of the image corresponds to the center of the cluster. Figure from Pan et al. 2016.

The pulsars are named in alphabetically in order of discovery with a prefix that is J followed by the equatorial coordinates of the neutron star. Sometimes the used prefix can be the name 47Tuc. In the list of the pulsars there are some letters missing: A, B and K. A and B, presented by Ables et al. (1989), were not confirmed in later observations (Manchester et al. 1991). Pulsar 47TucK (Manchester et al. 1991) was later found to be the third harmonic of the pulsar 47TucD. (Robinson et al. 1995).

All of the pulsars except 47TucX are located in the center of the cluster with maximum offsets of 1 arc-minute ($\sim$ 3 core radii).

The pulsars are all millisecond pulsars with periods going from $\sim$ 1.84 ms for 47TucAB (Pan

et al. 2016) to ~ 7.58 ms for 47TucT (Camilo et al. 2000).

13 of the 25 pulsars are in binaries with orbital periods from ~ 3 hours to 2.3 days. All have companions with maximum masses lower than $0.2\,M_\odot$ and some go as low as $0.02\,M_\odot$. Optical counterparts were found for the He white dwarf companions of the pulsars U (Edmonds et al. 2001), W (Edmonds et al. 2002), Q, S, T, Y (Rivera-Sandoval et al. 2015, Cadelano et al. 2015) with tentative associations for H and I (Cadelano et al. 2015). Four binaries are eclipsing and therefore not observable at all times, these are 47TucJ, 47TucO, 47TucR, 47TucW.

Because of the precise measurements of the positions it was possible to find the X-ray counterparts of all the pulsars with the Chandra X-ray Observatory (Heinke et al. 2005, Bogdanov et al. 2006) except those without a timing solution (47TucP, 47TucV, 47TucAA) .

5.2 Intracluster Medium

The diffuse gas in 47 Tucanae is constantly produced by the AGB and RGB stars with a time averaged rate of $\sim 3 \times 10^{-6} M_\odot\,\mathrm{yr}^{-1}$ (McDonald and Zijlstra 2015). Only $\sim 1/3$ of the gas is produced by AGB stars while the rest is produced by stars at the RGB tip (McDonald and Zijlstra 2015).

The intracluster medium is expelled by some fast internal mechanism so that it does not accumulate. This mechanism operates on the dynamical time scale of ~ 4.3 Myr so the total remaining ICM mass is equal to mass lost by stars on a dynamical time (McDonald and Zijlstra 2015).

Detection of the ICM

So far observations have failed to find neutral gas or dust in this cluster. The only confirmed detection of ICM is that of ionized medium in the cluster using the dispersion measures of the pulsars by Freire et al. (2001b). Here, following the paper, I describe how they arrived at this result.

The authors used data of DM and $(\dot{P}/P)$ from the 15 pulsars with known timing solution at the time. The quantity $(\dot{P}/P)$ contains information on the line-of-sight acceleration in the gravitational potential of the cluster through the formula $(\dot{P}/P) = a/c$. However the observed quantity receives also a contribution from the intrinsic spin-down of the pulsars, which is always positive. This means that if $(\dot{P}/P)$ is negative, the line-of-sight acceleration must be directed towards us. This is possible only if the pulsar lies in the hemisphere beyond the plane passing through the center.

As can be seen from fig. 3.9 most of the pulsars with negative $(\dot{P}/P)_{obs}$ have DM higher than the central value. This means that the radiation from the furthest pulsars has to cross more ionized hydrogen than the radiation from the nearest pulsars. It is very improbable that this is due to a chance alignment and it is considered to be caused by the intracluster medium.

Then, they tried to measure R, the distance on the line-of-sight from the plane passing through the center and the position of the pulsar. To do this they assumed a constant value of $(\dot{P}/P)_{int}$ and measured the line-of-sight acceleration with the formula $a/c = (\dot{P}/P)_{obs} - (\dot{P}/P)_{int}$ and confronted it with what is expected from a King model for the gravitational potential.

Using this value of R they built a model with three free parameters, n_e (uniform density of ionized medium), DM_c (DM for the center of the cluster) and $(\dot{P}/P)_{int}$ to describe how the DM should vary for each pulsar:

$$\mathcal{DM}_i = DM_c + n_e R_i[(\dot{P}/P)_{obs} - (\dot{P}/P)_{int}] \tag{3.2}$$
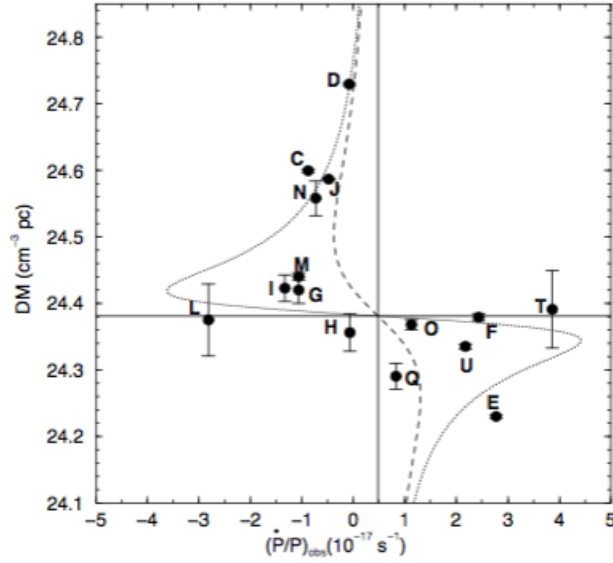
Figure 3.9: Measured DM against $(\dot{P}/P)_{obs}$ for 15 millisecond pulsars. Most of the pulsars with negative $(\dot{P}/P)_{obs}$ have DM higher than the center. The curves show the expected trend along line of sights passing through the core (dotted) and 2 pc from the core (dashed). Figure from Freire et al. 2001b.

Using a least-square method they found the parameters that minimise the difference between the observed DM and the model and obtained $n_e = 0.067 \pm 0.015\,\mathrm{cm}^{-3}$, $DM_c = 24.381 \pm 0.009\,\mathrm{cm}^{-3}\mathrm{pc}$ and $[\dot{P}/P]_{int} = (0.48 \pm 0.18) \times 10^{-17}\mathrm{s}^{-1}$.

Using these values they measured that the central region populated by the pulsars (approximately a spherical region with radius ~ 2.5 pc) contains $\sim 0.1\,M_\odot$ of ionized matter. Using a Plummer density model it is possible to estimate the total mass of the ionized ICM in the cluster to $\sim 11\,M_\odot$ (McDonald and Zijlstra 2015).

Ionization and evacuation of the ICM

Searches for neutral gas in the cluster only resulted in upper limits. This means that either there is very little gas, contrary to what is expected considering the strong winds of the AGB stars, or it is completely ionized. This part follow the description of McDonald and Zijlstra 2015 which give a detailed description of the possible ionizing radiation sources in the cluster and their capability to ionize all the neutral matter ejected by stars.

The first thing to do is to calculate the neutral mass input in the cluster. The biggest contribution comes from dying stars which expel entirely their envelopes. The average stellar death rate is one per 80000 yr (McDonald et al. 2011) and the average initial and final mass are 0.87 and 0.53 $M_\odot$ (McDonald et al. 2011, Kalirai 2013) this implies a total mass-loss rate of $\dot{M}_* \approx 4 \times 10^{-6}\,M_\odot\,\mathrm{yr}^{-1}$ or $\dot{N}_* \approx 1.6 \times 10^{44}\mathrm{amu\,s}^{-1}$. If all of this material must be ionized $\geq 10^{44}$ ionizing photons s^{-1} are needed. This means that in the cluster there must be at least 2×10^{26} W of ionizing radiation.

A first possible source of this radiation is the γ-ray emission of pulsars. Pulsars lose a substantial amount of their spin-down luminosity as high-energy radiation. The spin down luminosity (eq. 2.3) of each pulsar, assuming normal masses and radii, is $\sim 10^{26} - 10^{27.5}$ W. If we assume a total ~ 1000 pulsars and an attenuation coefficient of 1 part per billion (only one photon every billion is absorbed) the total ionizing radiation absorbed is $\sim 10^{21}$ W, not enough for the whole cluster. Pulsars could heat and ionize the ICM by thermalization of the relativistic ions ejected. This mechanism should manifest itself as a diffuse high energy radiation within the cluster. Such radiation has been observed (Wu et al. 2014) but the flux ($\sim 2 \times 10^{25}$ W) is an order of magnitude smaller than the necessary.

Other possible sources are the X-ray binaries, cataclysmic variables and other discrete X-ray and extreme UV sources. Summing the brightest X-ray sources detected by Chandra (Heinke et al. 2005) the total ionizing flux is $\approx 4 \times 10^{41}$ photons s^{-1} of which only $\approx 10^{32}$ photons s^{-1} will be absorbed. This flux is 11 orders of magnitude too small so this source must be excluded.

The last possible source are thermal UV sources like post-AGB stars and young white dwarfs. In far UV observations of the cluster (O'Connell et al. 1997, Knigge et al. 2008, Schiavon et al. 2012) the flux is dominated by only a few stars but several of them are capable of providing the necessary ionizing flux to ionize the entire ICM.

Considering the sum of these sources the total estimated ionizing flux is $\sim 10^{45}$ photons s^{-1} and assuming a recombination rate of $1.4 \times 10^{-15} \text{cm}^{-3}\text{s}^{-1}$ the Strömgren sphere radius is 110-200 pc. This is larger than the entire cluster and therefore we expect no neutral hydrogen in the cluster. In summary all the ICM is expected to be ionized by the few post-AGB stars and hot white dwarfs.

McDonald and Zijlstra performed a simulation to show that, assuming that every 80000 yr a new white dwarf is born, the cluster will always be ionized with fluxes between 2×10^{46} and 8×10^{47} photons s^{-1}.

The radiatively heated ICM must be pressure supported against the gravitational attraction of the cluster. The pressure, given by the ideal gas law, depends on the temperature profile of the gas. By modelling the gravitational potential with a Plummer model and the temperature with a photoionization model, McDonald and Zijlstra (2015) calculated the radial velocity of the gas and the mass ejected by the cluster. The simulations show that the gas is driven out of the cluster and is cleared on a dynamical time-scale.

Chapter 4

Observational techniques

In this chapter I will explain the various techniques used for observing radio pulsars and how to reduce the data obtained from the observations. First, the radio signals are corrected from the effects of dispersion and the interferences due to artificial signals (Radio Frequency Interference) are eliminated. Then the data is calibrated in flux and in polarization using templates obtained at the radio telescope.

1   Observing pulsars

During the early times of pulsar observations the radio signal was obtained directly from the detector tracing with a pen the intensity of the signal on a roll of paper. An example of this pen chart recording can be seen in figure 2.1. The recordings were later analysed directly by the observers looking for a periodic signal.

With this kind of observations only the brightest pulsars with low dispersion measures and long periods could be detected. To observe the rest of the population the astronomical community had to develop new and fascinating techniques.

The first problem that had to be solved was the low flux of most of the pulsars. The single pulses for the majority of these objects have such low fluxes that they are much fainter than the noise recorded by the detector so they are undetectable with this technique. The technique used to solve this problem for pulsars of known period is to divide the observation in subsets of duration exactly set at the period of the pulsar and sum all the subsets together. This process is called *folding* and the result is called the *integrated profile*.

Provided the intrinsic period is constant in all the subsets the pulsed signal arrive at the same phase and it is summed together. Observing for a long time can therefore make the signal to increase linearly with the number of subsets whereas the noise grows only as the root of the number of subsets.

There are however additional problems to be taken into account. As we know the dispersion of the pulse in frequency spreads the phase of the signal across the observing band. This will smear the integrated profile and cancel completely the pulsar signal. Another problem occurs if the folding period is not correct or the pulsar is in a binary system. In this case the pulse will move along the phase and become invisible when integrating the signal over many subsets. A third problem is that short bursts of loud interference can appear sporadically and mask the pulsar.

The usual solution to these problems is on one side to de-disperse the signal (see below) and on the other side to observe the pulsar for a long time and create integrated profiles every short time lapses, typically less then one minute, called *sub-integration times*. Inside each sub-integration we can be sure that the profile will be very sharp even if it is not very bright. Then we can check if the pulses are all aligned at the same phase and sum them together to create the total integrated profile. If the profiles in the sub-integrations are not aligned we have to modify the timing solution of the pulsar, a concept that will be explained better in the section on the timing technique. If some sub-integrations are affected by interference the usual course of action is to eliminate them as described in a following paragraph.

1.1   De-dispersion

As mentioned above, a critical problem to be solved is the dispersion of the pulse due to the ionized medium on the line of sight. As we saw in figure 2.14, dispersion, if not treated correctly, can make undetectable otherwise bright pulsars. To solve this problem a number of techniques have been developed under the name of *de-dispersion techniques*: (following the description of Lorimer and Kramer 2005)

Incoherent de-dispersion

The simplest technique consists in dividing the incoming radiation in different frequency channels and applying for each frequency the corresponding time delay. The equation that is used to calculate the delays is (from eq. 2.20):

$$\Delta t \simeq 4.15 \times 10^6 \text{ms} \, (\text{f}_{\text{ref}}^{-2} - \text{f}_{\text{chan}}^{-2}) \times \text{DM}, \tag{4.1}$$

where f_{ref} is usually the center frequency of the band expressed in MHz, f_{chan} is the frequency of the channel expressed in MHz.

The process of de-dispersion is shown in the figure 4.1. As can be seen in that figure also inside each frequency band the pulse is dispersed. To minimize the effect it is necessary to choose the widths of the frequency bands in order to obtain a smearing less than about the sampling time while using the smallest number of bands.

The simplest way to divide the radiation in frequency channels is through the use of analog filterbank spectrometers. The incoming signal is divided in a number of wires connected to different filters that select only a narrow band of frequencies which are then digitised separately. However this method does not allow rapid changes in the number and bandwidths of channels as we have to modify directly the hardware.

Another much more flexible method is the *autocorrelation spectrometer*. This instrument multiplies the signal with a delayed copy of itself and reconstructs the autocorrelation function. From the autocorrelation function it can be possible to find the power spectrum and so the frequency information we need. The frequency width of one channel which is achievable with this technique is linked to the number of lags recorded. Since this number can easily be modified via software, the width can be varied without touching the hardware.

Coherent de-dispersion

A way to completely eliminate the effect of the ionized matter is to use the coherent de-dispersion technique. After having measured the complex voltages received by the telescope, this method
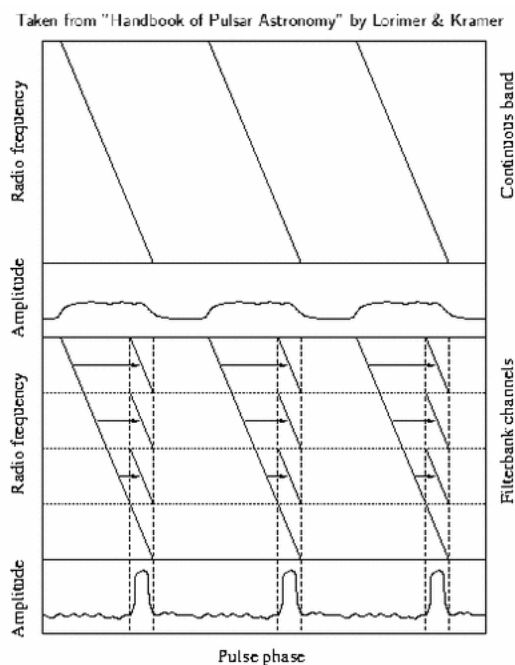
Figure 4.1: Pulse dispersion and incoherent de-dispersion. The top panel shows the measured time sequence of the pulse, the diagonal lines are the pulse peaks as a function of frequency and time. Not correcting for dispersion gives a very large and smeared profile. In the bottom panel the process of incoherent de-dispersion is exemplified using only four frequency bands. The frequency channel are delayed so that the pulses always happen at the same phase. The corresponding profile is much more peaked and clear. Figure from Lorimer and Kramer 2005.

recovers the intrinsic voltages as resulting from a non dispersive medium.

The distortion due to the interstellar medium can be seen as the effect of a phase-only function or *transfer function*, H, defined in the frequency domain as follows:

$$V(f_0 + f) = V_{int}(f_0 + f)H(f_0 + f), \tag{4.2}$$

where f_0 is the frequency of the center of the band, $V(f_0 + f)$ is the Fourier transform of the voltage measured by the telescope and $V_{int}(f_0 + f)$ is the Fourier transform of the intrinsic voltage emitted by the pulsar.

It can be shown that the transfer function H can be linked to the dispersion measure DM through the formula (Lorimer and Kramer 2005):

$$H(f_0 + f) = e^{i\frac{2\pi \mathcal{D}}{(f_0+f)f_0^2}\mathrm{DM}f^2}, \tag{4.3}$$

where $\mathcal{D}$ is the dispersion constant defined in eq. 2.19.

To obtain the original voltage emitted we only need to measure the complex voltage observed and apply the Fourier transform.

To measure the complex voltage and digitise it directly the technique of *baseband sampling* is used. This consists in duplicating the signal and mixing one with a local oscillator (LO) of frequency f_{LO} and the other with the same LO but with a phase shift of $\pi/2$. If we choose a LO with frequency equal to the center of the band ($f_{LO} = f_0$) and we apply a low pass filter it can be shown that the two signals are just the real and the imaginary part of the complex voltage. After this stage the signals are digitised and sampled at the Nyquist rate.

Now we can calculate the emitted radiation and correct for the effects of dispersion.

Coherent de-dispersion is very computationally expensive but modern hardware and software allow us to de-disperse a time series in real time and this allows the observer to check during the observation if everything is working correctly. Additionally it is not necessary in this case to record all the informations taken by the telescope but only the de-dispersed time series which saves a lot of hard disk space.

1.2 Radio Frequency Interference (RFI)

When observing the sky at radio frequencies there is also the problem of Radio Frequency Interference (RFI). These interferences usually have man-made origin and are so loud that can cover completely the weak astronomical signals we are searching for. The RFI can be of different origin: some can come from sources with fixed frequencies like radio and television communications or the mobile and internet network; some can come from harmonics from the AC power line; some can originate from the computers in the observatory and some can even be of natural origin coming from electrical storms.

Some precautions have been taken by the community to reduce the interferences such as protecting with specific laws some important frequencies and by building radio telescopes in remote and radio-quiet areas. However it is impossible to remove all the RFI from the observing band and some care has to be taken to isolate and correct them from the data.

The interference usually manifests itself in two ways, as wide-band sporadic bursts or as a constant signal at a fixed frequency. The path taken to correct it is to eliminate the affected sub-integrations and frequency channels with a frequency or time domain clipping. An example of the result of this correction process can be seen in figure 4.2: after removing the interference, the signal from the pulsar becomes clearly visible.

Some RFI, usually those originating from a fixed source, always affect the same frequency channels and therefore can be treated differently. After scanning the sky with the main antenna or with a smaller one at the same observatory a list of the affected channels is created. Then the data obtained from those frequencies are automatically discarded.

2 Flux calibration

Astronomical data as taken from the telescope is not calibrated in flux and so the measured quantity is not in jansky (Jy) (or mJy as is more common with pulsar data) but usually is in Arbitrary Digital Unit (ADU) or counts.

To correct this (following Lorimer and Kramer 2005) it is first necessary to measure the system noise temperature of the telescope. To do this we observe a source of known flux (or antenna temperature T_{src}) and measure the counts (called ON counts) then we observe a patch of sky with no strong sources and measure the counts there (called OFF counts). The noise temperature T_{sys} can be derived from the formula:

(a) Archive affected by RFI
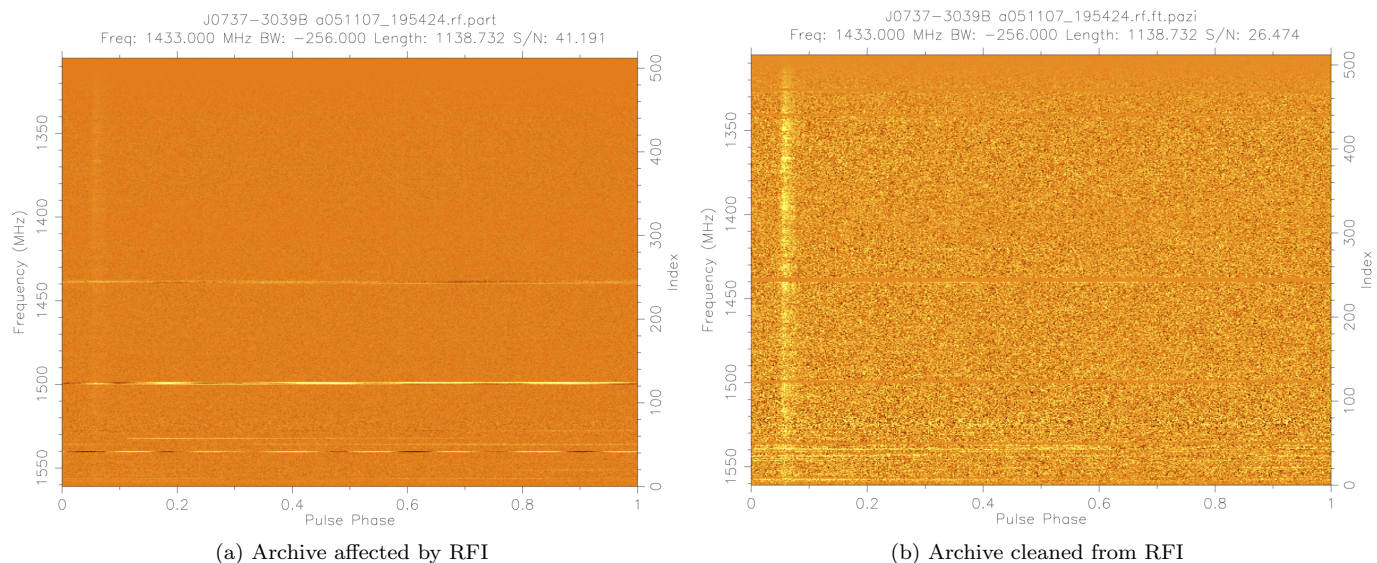
(b) Archive cleaned from RFI

Figure 4.2: Plots of the profile of the pulsar J0737-3039B as a function of frequency and phase. On the left is the plot affected by the RFI and on the right is a plot of the same data after frequency domain clipping.

$$\frac{\text{ON} - \text{OFF}}{\text{OFF}} = \frac{T_{src}}{T_{sys}} \tag{4.4}$$

Having measured T_{sys} it is possible to obtain the mean flux density of the pulsar profile knowing the SNR (signal-to-noise ratio) of the profile and the so called gain of the telescope.

This approach is stricly valid only if the noise level when observing the calibrator source and when observing the pulsar is the same. A better way to proceed would be to inject noise in the antenna through a diode and measure the counts (called CAL counts). If the corresponding antenna temperature T_{cal} is known then this level can be used as a reference instead of T_{sys}. When observing the diode we will have:

$$\frac{\text{CAL} - \text{OFF}}{\text{OFF}} = \frac{T_{cal}}{T_{sys}}. \tag{4.5}$$

So together with eq. 4.4 we obtain:

$$\frac{S_{cal}}{S_{src}} = \frac{T_{cal}}{T_{src}} = \frac{\text{CAL} - \text{OFF}}{\text{ON} - \text{OFF}}, \tag{4.6}$$

Where S_{cal} and S_{src} are the calibrated flux measures.

Using this method it is possible to calibrate in flux in a way that is independent of the gain of the telescope and system temperature.

3 Polarisation calibration

As we have seen in the second chapter, pulsars are often very polarized sources of radiation. It is, therefore, very interesting to obtain calibrated polarized data. Apart from being able to study the polarization, the rotation measure and the magnetic field on the line of sight, having calibrated data also corrects some noise in very precise timing experiments (van Straten 2013) and makes the signal to noise ratio of the profile better.

For this purpose the telescope receiver has to extract two orthogonal polarizations (usually linear or circular) from the incoming radiation. The two polarizations are then amplified and processed separately and then mixed to obtain the *Stokes parameters* (Stokes 1852). The Stokes parameters are 4 parameters which describe completely the polarization of the radiation, they are: I, which represents the total intensity, Q which represents the linear polarization along the two major axis, U, representing the linear polarization along the diagonals and V, representing the circular polarization.

Depending on the polarizations extracted and the de-dispersion technique used it is possible to reconstruct the Stokes parameters using simple formulas (taken from Lorimer and Kramer 2005). If the data is coherently de-dispersed and the linear polarizations are extracted, called X and Y, then the formulas are:

$$I = |X|^2 + |Y|^2 \tag{4.7}$$
$$Q = |X|^2 - |Y|^2 \tag{4.8}$$
$$U = 2\mathrm{Re}(\mathrm{X} * \mathrm{Y}) \tag{4.9}$$
$$V = 2\mathrm{Im}(\mathrm{X} * \mathrm{Y}). \tag{4.10}$$

If the data is coherently de-dispersed and the circular polarizations are extracted, called L and R, then the formulas are:

$$I = |L|^2 + |R|^2 \tag{4.11}$$
$$Q = 2\mathrm{Re}(\mathrm{L} * \mathrm{R}) \tag{4.12}$$
$$U = 2\mathrm{Im}(\mathrm{L} * \mathrm{R}) \tag{4.13}$$
$$V = |L|^2 - |R|^2. \tag{4.14}$$

If the data is corrected using incoherent de-dispersion, the signals of the various channels are added without keeping the phase constant. So we can't probe directly the phase of the voltage but only the amplitude of the two feeds, A and B. In this case we need to add a stage in which the two polarizations are autocorrelated with themselves (producing P_{AA} and P_{BB}) and cross-correlated with each other (producing P_{AB} and P_{BA}). Then the Stokes parameters can be extracted in the case of linear polarization from:

$$I = |P_{AA}|^2 + |P_{BB}|^2 \tag{4.15}$$
$$Q = |P_{AA}|^2 - |P_{BB}|^2 \tag{4.16}$$
$$U = 2\mathrm{Re}(\mathrm{P_{AB}}) \tag{4.17}$$
$$V = 2\mathrm{Im}(\mathrm{P_{BA}}). \tag{4.18}$$

Instead for circular polarization:

$$I = |P_{AA}|^2 + |P_{BB}|^2 \tag{4.19}$$

$$Q = 2\mathrm{Re}(\mathrm{P_{BA}}) \tag{4.20}$$

$$U = 2\mathrm{Im}(\mathrm{P_{AB}}) \tag{4.21}$$

$$V = |P_{AA}|^2 - |P_{BB}|^2. \tag{4.22}$$

From the Stokes parameters it is possible to find the polarization position angle of the radiation (measured from north to east with respect to the north celestial pole) and the full linear polarization from:

$$\mathrm{PA} = \frac{1}{2}\mathrm{arctan}(\frac{\mathrm{U}}{\mathrm{Q}}) \tag{4.23}$$

$$L = (U^2 + Q^2)^{1/2} \tag{4.24}$$

The parameters obtained in this way are still not the real Stokes parameters as they need to be calibrated (Heiles et al. 2001).

Problems can arise in practice since no feed can work perfectly over the whole observing band: e.g. some junctions used can have a response that is frequency-dependant. Furthermore it is almost impossible to build two perfectly orthogonal feeds and some polarized signal will be captured also by the feed which should be perpendicular to that. The two polarizations feeds are connected to different wires and amplifiers therefore the net gain of the entire circuits can be different for the two polarizations even if the feeds are perfect. An example of this can be seen in fig 4.3.

The way to correct the effects due to the imperfect feeds (called *cross coupling*) is to illuminate the feeds with a noise source so that both polarizations should measure the same signal. The outputs are then compared with the input and a matrix containing the corrections is created. This calibration does not need to be made very often as the feed are usually stable. At the Parkes radio telescope it is done every 3 months.

The way to correct the different gains of the different polarizations is to inject directly into both circuits a known signal of fixed intensity. Since the gain fluctuations of the amplifiers can vary in short times it is necessary to repeat this calibration at the start of every observation.

3.1 Mueller matrix

Calling S the Stokes vector (i.e. the 4-dimensional vector formed by the four Stokes parameters) we can summarize the effects of all the imperfections in the receiver as the effects of a transfer function:

$$S_{out} = \mathcal{M} \times S_{in}, \tag{4.25}$$

where $\mathcal{M}$ is the *Mueller matrix* (Mueller 1948), S_{out} is the Stokes vector measured by the receiver and S_{in} is the real Stokes vector of the incoming radiation.

The Mueller matrix can be decomposed as the product of four different matrices each correcting for a single effect:

$$\mathcal{M} = \mathcal{M}_{Amp} \times \mathcal{M}_{CC} \times \mathcal{M}_{Feed} \times \mathcal{M}_{PA} \tag{4.26}$$
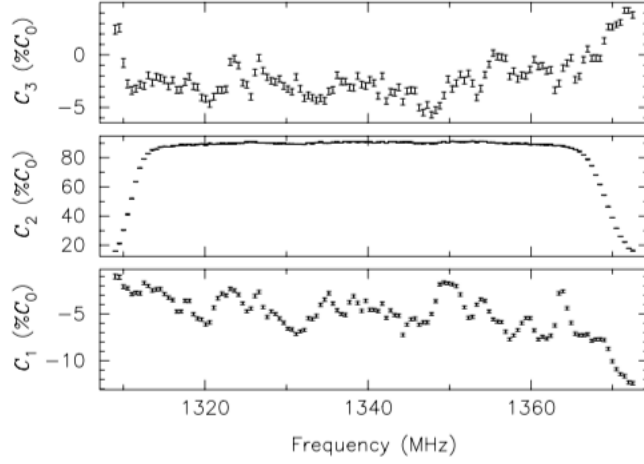
Figure 4.3: Stokes parameters measured for the noise diode reference signal at the Parkes radio telescope. The value of the Stokes parameters Q, U and V are represented by C_1, C_2 and C_3. The input signal should ideally be a 100% linearly polarized signal with position angle of $45°$, so the ideal Stokes vector should be $[1, 0, 1, 0]$. The receiver introduces polarization with the wrong position angle and circular polarization. The dependence on the frequency is clearly visible especially at the boundaries of the band. Figure from van Straten 2004.

$\mathcal{M}_{Amp}$ considers the different gains of the two circuits, $\mathcal{M}_{CC}$ considers the cross-coupling of the feeds, $\mathcal{M}_{Feed}$ considers the type of feeds used and $\mathcal{M}_{PA}$ considers the fact that while observing the source the telescope feeds will rotate (if the telescope mount is alt-azimuthal).

Here, following Heiles et al. 2001 and Lorimer and Kramer 2005, I will describe the form of every component of the matrix going from right to left, i.e. following the order of the matrix multiplication.

$\mathcal{M}_{PA}$

The feeds of telescope will be rotated with respect to the north celestial pole by an angle:

$$\mathrm{PA_{az}} = \arctan\left(\frac{\sin \mathrm{HA} \cos \phi}{\sin \phi \cos \delta - \cos \phi \sin \delta \cos \mathrm{HA}}\right), \tag{4.27}$$

where HA is the hour angle of the source of declination δ, ϕ is the latitude of the observatory.

The corresponding Mueller matrix will simply be a rotation matrix for the parameters Q and U of this angle:

$$\mathcal{M}_{PA} = \begin{bmatrix} 1 & 0 & 0 & 0 \\ 0 & \cos 2\mathrm{PA_{az}} & \sin 2\mathrm{PA_{az}} & 0 \\ 0 & -\sin 2\mathrm{PA_{az}} & \cos 2\mathrm{PA_{az}} & 0 \\ 0 & 0 & 0 & 1 \end{bmatrix} \tag{4.28}$$

In the case of an equatorial telescope this matrix would not be needed as the feeds would not rotate with respect to the north celestial pole. However since all the major radio telescopes functioning nowadays have alt-azimuthal mounts I will not consider this case.

$\mathcal{M}_{Feed}$

Depending on whether the feeds are linear or circular they read different values of the polarization. The effect can be described by the angle α which is the amount of coupling into the orthogonal polarization.

$$\mathcal{M}_{Feed} = \begin{bmatrix} 1 & 0 & 0 & 0 \\ 0 & \cos 2\alpha & 0 & \sin 2\alpha \\ 0 & 0 & 1 & 0 \\ 0 & -\sin 2\alpha & 0 & \cos 2\alpha \end{bmatrix} \tag{4.29}$$

For linear feeds ($\alpha = 0$) it just becomes:

$$\mathcal{M}_{PA} = \begin{bmatrix} 1 & 0 & 0 & 0 \\ 0 & 1 & 0 & 0 \\ 0 & 0 & 1 & 0 \\ 0 & 0 & 0 & 1 \end{bmatrix} \tag{4.30}$$

while for circular feeds ($\alpha = 45°$) it becomes:

$$\mathcal{M}_{PA} = \begin{bmatrix} 1 & 0 & 0 & 0 \\ 0 & 0 & 0 & 1 \\ 0 & 0 & 1 & 0 \\ 0 & -1 & 0 & 0 \end{bmatrix} \tag{4.31}$$

$\mathcal{M}_{CC}$

If the feeds are imperfect and there is a cross coupling between the two feeds, the matrix needed to correct this effect is:

$$\mathcal{M}_{PA} = \begin{bmatrix} 1 & 0 & A & B \\ 0 & 1 & C & D \\ A & -C & 1 & 0 \\ B & -D & 0 & 1 \end{bmatrix} \tag{4.32}$$

where the constants depend on the magnitude and phase (ϵ and ϕ) of the cross-coupling from the two probes:

$$A = \epsilon_1 \cos \phi_1 + \epsilon_2 \cos \phi_2 \tag{4.33}$$
$$B = \epsilon_1 \sin \phi_1 + \epsilon_2 \sin \phi_2 \tag{4.34}$$
$$C = \epsilon_1 \cos \phi_1 - \epsilon_2 \cos \phi_2 \tag{4.35}$$
$$D = \epsilon_1 \sin \phi_1 - \epsilon_2 \sin \phi_2 \tag{4.36}$$

$\mathcal{M}_{Amp}$

The different amplifier chains might have different gains and phase delays. Considering that the two circuits have a difference in gain of ΔG and a difference in phase delays of $\Delta\varphi$:

$$\mathcal{M}_{PA} = \begin{bmatrix} 1 & \Delta G/2 & 0 & 0 \\ \Delta G/2 & 0 & 0 & 0 \\ 0 & 0 & \cos\Delta\varphi & -\sin\Delta\varphi \\ 0 & 0 & \sin\Delta\varphi & \cos\Delta\varphi \end{bmatrix} \tag{4.37}$$

After obtaining all the useful quantities from calibrations with known sources of different types it is possible to reconstruct the total Mueller matrix, and multiply its inverse with the measured Stokes vector to obtain the calibrated polarization quantities.

Most of the critical problems arise from manufacture errors of the feeds and amplifiers and it would be tempting to try to fix them directly at the hardware level. However, since it would be highly expensive and almost impossible to build perfect detectors, the software solution of the calibration as described above is the most cost-effective and safe way to proceed.

4   Timing technique

Many of the important results and discoveries in pulsar astronomy have been made with the technique of *pulsar timing*. This technique consists in measuring the arrival times of the pulses to a high precision and using this information to find the positional, kinematic and, when possible, orbital parameters of the source. The way to find these parameters will be explained in the next paragraphs following the description in D'Amico and Burgay 2009 and Lorimer and Kramer 2005.

4.1   Time of Arrival (ToA) observation

The first step is to obtain the time of arrival of the pulses at the telescope with a high precision. To do so we must first build a template for the pulse profile and that is done either by using an integrated profile with high SNR taken from many observations or by approximating it with a simulated noiseless profile.

The template is then shifted and enlarged to match perfectly the observed profiles with an algorithm that minimises the residual chi square. The phase difference between the peak and a fiducial point of the profile yields the relative ToA difference with respect to the beginning of the sub-integration producing the observed profile.

Once the ToAs are measured they need to be converted in a uniform time reference scale, like the International Atomic Time (TAI), so that the data from all observatories and from all the past years can be confronted directly. The standard time reference, the UTC, cannot be used because it is often changed adding leap seconds (the last one was added on June 31th 2015). Although little, this time difference would shift all ToAs and render them incomparable with the ones from the previous years.

Then the ToAs have to be transformed to the Solar System Baricenter (SSB) reference frame. This is an inertial reference frame centred at the solar system baricenter and devoid of all relativistic corrections. To do this we need to consider the motion of the Earth around the Sun which gives rise to the *Roemer delay*, the general relativistic effects due to the curved spacetime of the Solar

System, the *Einstein delay*, and the additional delay due to the curvature of spacetime near large bodies, the *Shapiro delay*.

4.2   Parameters derivable from timing

From the ToAs we can many different parameters of various nature. This is done studying the *time residuals* of each observation. The time residuals are the differences in phase between the ToAs and and the start of the sub-integration. They can be transformed in time by multiplying the phase by the period of the pulsar. The parameters that can be be found are:

Period

If the period at which the observations are folded is not correct we would observe the pulse profile to shift to different phases as the observation goes on. In this case we will also observe that the residuals of the ToAs will linearly increase, or decrease, over the span of the observation. We can correct this effect and find the correct period by finding the slope of this line.

Period derivative

We know that all pulsars tend to slow down and so we should expect the period of the pulsar to decrease over time. If the observation is long enough we should see that the residuals of the ToAs will drift out of the optimal region following a parabolic curve (assuming that the period derivative is constant). We can correct this effect by setting a correct period derivative in our fitting model.

Position

When we move the ToAs in the SSB reference frame we have to correct for the Roemer delay, which corresponds to the time difference that the light has to travel to reach the current position of the Earth with respect to the SSB. This delay will depend on the position in the sky of the pulsar and initially it is known only approximately as the beam of the typical radio telescope is large. Consequently if the initially set coordinates for the pulsars are wrong we should see a periodic sinusoidal trend with a period of exactly one year. This can be corrected with high precision leading to a better determination of the position.

Proper motion

We have seen in the pulsar overview chapter that pulsars tend to have large velocities. If the velocity perpendicular to the line of sight is large and the observations span many years, we can see that the position of the pulsar in the sky will change and we can measure the speed. The effect will be a sinusoidal trend with a period of one year (like for the Roemer delay) with amplitude increasing as the pulsar moves far from the measured position.

Binary parameters

If the pulsar is in a binary system we should see the arrival time of the pulses anticipate or delay according to the position in the orbit. The effect would be like that of the Roemer delay but the period will be that of the binary system. The different parameters (known as Keplerian parameters) that can be measured in this case are: the orbital period, the eccentricity, the projection of the

semi-major axis along the line of sight toward the pulsar, the periastron longitude and the epoch of periastron.

Using keplerian dynamics it is possible to find the reduced mass of the system. So we find a relationship between the mass of the neutron star, te mass of the companion and the angle of inclination. At this point however it is impossible to find each parameter independently and we can give an estimate of the minimum mass of the companion assuming a typical neutron star mass and an orbit inclination of $90°$.

Post-keplerian parameters

If very precise ToAs are available for binary pulsars in close binaries with compact objects then it may be possible to measure relativistic effects in the strong field regime. These can be expressed through a total of five post-keplerian parameters. These are: the rate of advance of the periastron, the orbital decay (due to gravitational radiation emission), the gravitational redshift γ and the rate and shape of the Shapiro delay (caused by the strong field of the companion).

We have a total of three different unknown quantities, the masses of the stars and the inclination of the orbit, and one relation between them derived from the keplerian parameters. In the framework of a given gravity theory we can relate the PK parameters to the same variables. Therefore, measuring just two of the PK parameters and assuming a gravity theory (the most used is general relativity), can completely determine the system.

All these parameters are usually contained in a file, called *ephemeris*. It is called this way because it allows us to predict in the future when the pulses will arrive just as the ephemerides of the Solar System predict where the planets will be. The residuals of the timing procedure with a good model and with wrong models are shown in fig. 4.4.

4.3   Tests for General Relativity

Once two post-keplerian parameters are determined and all the variables of the system are found then using the equations associated with the PK parameters in a given gravity theory is possible to estimate the other post-keplerian parameters. If these can also be measured directly it is possible to test the self-consistency of the theory used to predict them, so we can test wether the chosen theory is self-consistent in the strong regime. Tests of GR have only been done in the weak field regime in laboratories or in the Solar System so measuring these parameters could give better insight on or discredit the best theory for gravitation we have got so far.

Such tests have been carried out for the first time on the first binary pulsar discovered, B1913+16 (Hulse and Tayolr 1975). The theory predicted that the orbital period of this system would decay over time due to the emission of gravitational waves and observations proved compatible with the predicted delay (fig. 4.5). Because of this discovery, in 1993 Hulse and Taylor were awarded the Nobel prize for Physics.

The most stringent test made to this day was done on the Double Pulsar J0737-3039 (Burgay et al. 2003, Lyne et al. 2004). For this system it was possible to measure all five post-keplerian parameters and it was possible to prove that the prediction of GR are correct up to $99.987(50)\%$ (fig. 4.6).
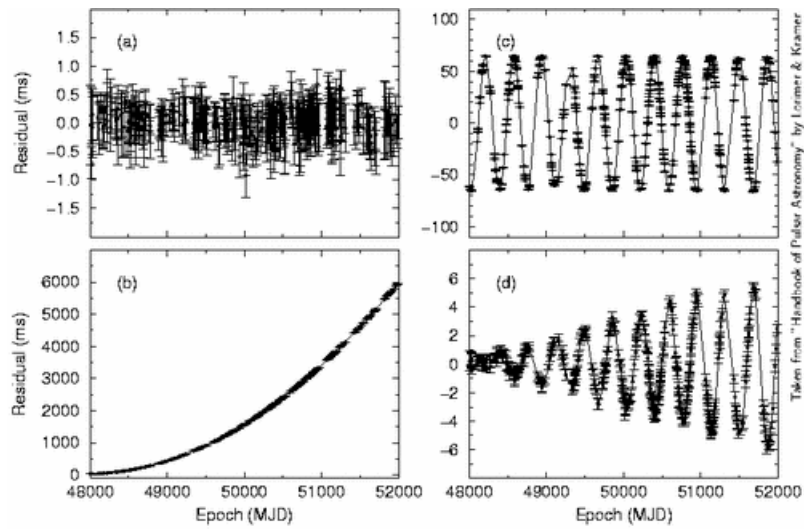
Figure 4.4: Examples of timing residuals for pulsar B1933+16. Figure (a) shows the residual with a good timing model. Figure (b) shows how the residuals appear if the period derivative is underestimated. Figure (c) shows the residuals if there is an offset in position. Figure (d) shows the effect of not considering the proper motion. Figure from Lorimer and Kramer 2005.
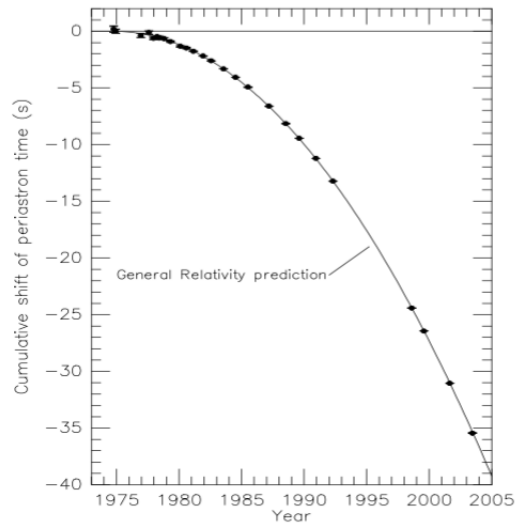
Figure 4.5: Orbital decay of pulsar B1913+16. The data indicate the change in the epoch of periastron while the line shows the GR prediction. Figure from Weisberg and Taylor 2005.

Figure 4.6: Plot of the possible masses of the two companions of the Double Pulsar J0737-3039. The lines represent the 1-sigma range of masses of the two companions according to each post-keplerian parameter. All lines cross in a very small region of masses. This shows that GR is self-consistent at the precision achieved by this test. The inset shows an enlargement of this region. Figure from Kramer et al. 2006.

Chapter 5

Data reduction and analysis

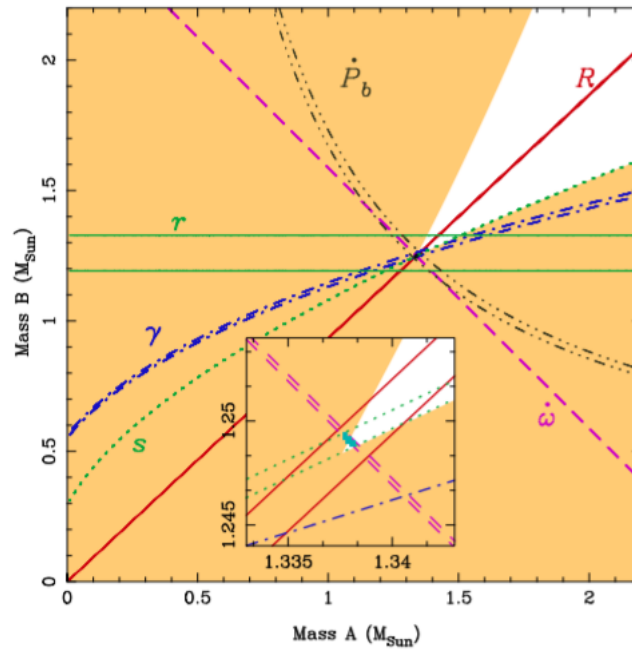In this chapter I will describe the data reduction process and the subsequent analysis. First, the data are acquired from the radio telescope and are sent to a super computer powerful enough to process it. Then they are cleaned and calibrated using dedicated software. After that, the Faraday rotation of the pulsars is finally calculated with a self-made code, tested with a Monte-Carlo simulation.

1 Obtaining data

The observations used in this analysis where obtained from April 2014 to March 2015 at the Parkes radio telescope (fig. 5.1) in Australia. This radio telescope was built in the 1960's and has had a glorious history in satellite tracking, communications and in radio astronomy. Thanks to the 21 cm Multibeam receiver installed in 1996 (Staveley-Smith et al. 1996), it became the world's leader in pulsar observations discovering alone more than half of all the pulsars known nowadays. This receiver has 13 beams, one at the center and the rest disposed along two concentric hexagons. Each beam has a Full Width Half Power (FWHP) of $14.4'$ and the beams are separated by two FWHP. The ability to observe 13 different regions of the sky while maintaining a high sensibility made it possible to allow the observers to conduct deep all-sky searches in very short times. This was the characteristic that allowed the Multibeam receiver to outshine its rivals in the search for new pulsars.

Our observations were made using the central beam of this receiver as the front-end while the CASPSR (CASPER Parkes Swinburne Recorder) back-end developed in collaboration with the Center for Astronomy Signal Processing and Electronics Research (CASPER) at Berkeley, was used. This backend uses coherent de-dispersion to correct the data.

The Multibeam receiver works at a frequency of 1360 MHz with a maximum bandwidth of 400 MHz, but, because of the RFI, the observing band was centered at 1382 MHz with a bandwidth of 312 MHz.

Because of the large field of view and the small angular size of the globular cluster 47 Tucanae (the half mass radius is $\sim 6'$), the receiver is able to observe the entirety of the central regions of the cluster with a single beam. This means that in a single pointing we are able to observe simultaneously all of the pulsars known in the cluster.

The total number of observations used in this analysis is 11, each around 8 hours long. This would mean that we have $80 - 90$ hours of integration time but not all the pulsars were visible

Figure 5.1: The Parkes radio telescope

during all of the observations. This is because the weakest of them are visible only during favourable scintillation events. So the total time in which each pulsar was observed can be significantly less than the time pent on source by the telescope.

Once the data for these observations have been recorded, they were transferred at the gSTAR cluster of the GREEN II supercomputer at the Swinburne University of Technology in Melbourne [1]. This cluster has 50 nodes each containing 2 six-core Westmere processors at 2.66 GHz, 48 GB RAM and 2 NVIDIA Tesla C2070 GPUs. On the same supercomputer are recorded also all the calibrators in flux and in polarization.

1.1   Data reduction

The data had to first be cleaned from RFI, calibrated and reduced in size so that they could be analysed more rapidly. To do so I used the open-source software package *psrchive* (Hotan et al. 2004, van Straten et al. 2012). This software package is implemented primarily in C++ and runs on UNIX environments.

RFI cleaning

The first step is RFI cleaning. As I said in the previous chapter, this is done by removing the frequency channels and subintegrations affected by the interference. The software in *psrchive* that eliminates the RFI is called *pazi* and has a graphical interface that shows all the different channels and subintegrations and updates the integrated profile every time data is removed.

---

[1]More information can be found on the site http://supercomputing.swin.edu.au

At every observation all the pulsars were observed simultaneously so the frequency channels affected by the RFI at each observations are the same. Because of this it is possible to obtain a list of affected channels looking at a single pulsar and remove the same channels from the rest. However, since the data of the different pulsars is folded at different periods, a periodic interference could be seen in the data of a pulsar but not in that of another as it is smeared on the entire profile. The same happens when looking at subintegrations, the same interference can appear in different places if the folding time is different.

Because of all these problems the best course of action to correctly remove all the RFI is to look at the data of every pulsar at every observation separately.

Since also the polarization calibrators are subject to RFI it is better to clean them in the same way so that the calibrated data can be considered completely clean.

Flux and polarization calibration

Flux and polarization calibration are usually done together using the software *pac* from *psrchive*. First we use it to create a database that contains the paths and relative informations to all the calibrator files, then we apply the calibration. The software first checks if the observations and the calibrators have the same receiver parameters, then it checks the date of the observations and applies the calibrators which are nearest in time.

Updating the timing ephemerides

Until this point the data have been corrected for an approximate DM and period but as we saw in the previous chapter this is not enough to have all the pulses arrive at the same phase. To correct that we must apply the correct timing solutions. Usually the solutions used at this stage are extracted from previous observations of the same pulsars. Since we are observing only millisecond pulsars, which are known to be very stable, an old solution can still work pretty well.

The best course of action after having applied the old solutions is to extract the new ToAs, using the software *pat*, and finding the new and correct timing solution using the software *tempo2* (Hobbs et al. 2006, Edwards et al. 2006). An example of how this can increase the SNR is shown in fig. 5.2.

Extracting the integrated profiles

At this point the data have been corrected from all the effects and we just need to create the integrated profile and select the right number of frequency sub-bands and profile bins.

In practice, the data from all the observations is compacted in a single file and then all subintegrations are summed together and we obtain the total integrated profile. If the profile is very noisy we can reduce the number of bins of the profile. This reduces the number of information that the profile carries but usually cuts down the noise and raises the SNR (Signal to Noise Ratio). The improvement granted by this procedure can be seen in fig. 5.3.

To obtain the Faraday rotation measure we need polarization information at different frequencies. The total number of channels recorder by the instrument is 1024, but using too many channels can actually be worse as the SNR of each channel is very low. Since the pulsars observed are not very strong we chose to work with only 4 frequency channels (i.e. sub-bands) to maximize the SNR of each channel.

(a) Time residuals with old ephemeris.   (b) Time residuals with new ephemeris.
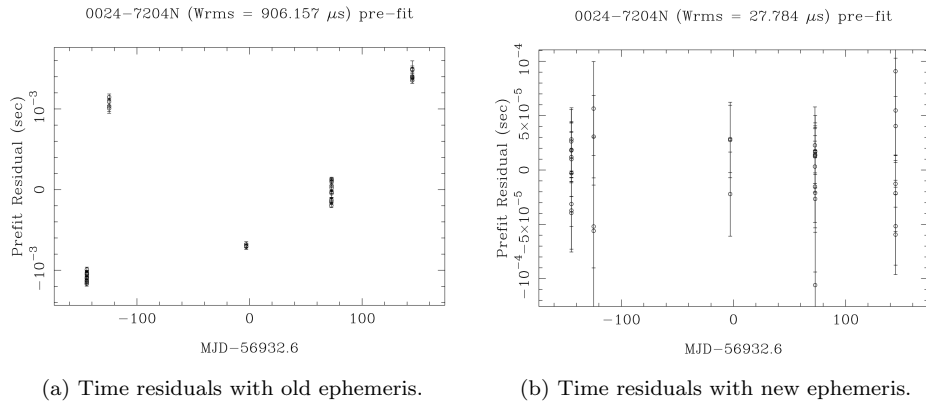
Figure 5.2: Plots of the time residuals of pulsar 47Tuc N with old and out of date timing solution (a) and with new and up to date timing solution (b). The plot (a) shows that the old timing solution is not correct. Instead with the newer ephemeris, the residuals are all close to zero. This guarantees that the profiles from all observations will be roughly aligned with one another. The integrated profile obtained with this solution will be very sharp and have a high SNR.

(a) Profile with 512 profile bins.   (b) Profile with 128 profile bins.
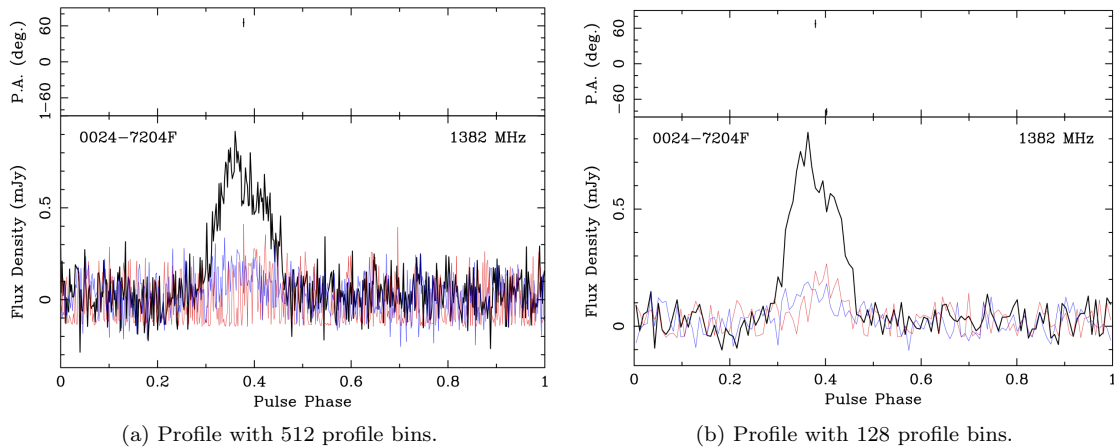
Figure 5.3: Integrated profile of pulsar 47Tuc F created keeping 512 profile bins (a) and reducing the number of bins to 128 (b). The second profile has a noise level that is reduced. Also, in (b), the linear and circular polarization of the profile become more important.

As we have noted before these pulsars are subject to scintillation and are not visible during all of the observations. So for some of the weakest pulsars we considered only the observations in which the pulsar was clearly visible to create the final integrated profile. In this way we lost much of the integration time but we were able to reduce the noise level and increase significantly the SNR. An example of how a profile can benefit from this procedure is seen in figure 5.4.

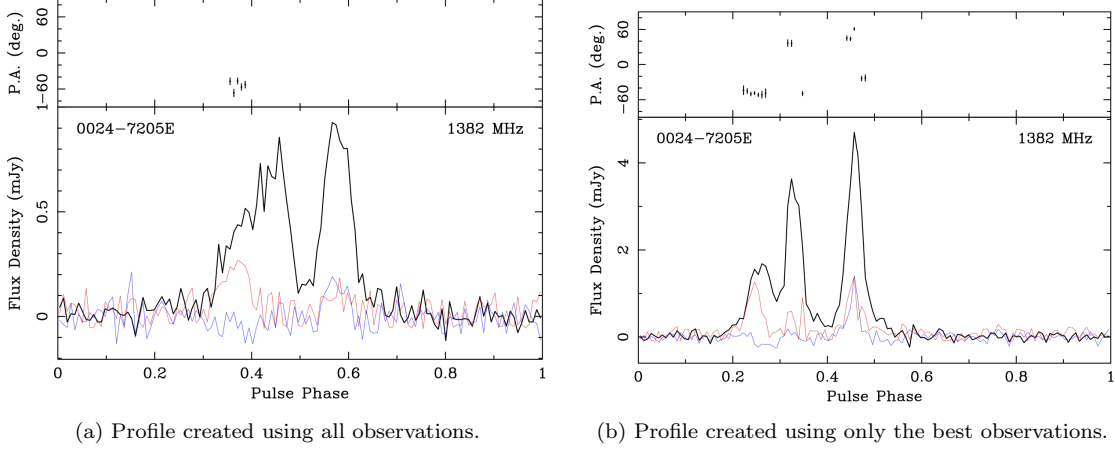(a) Profile created using all observations.   (b) Profile created using only the best observations.

Figure 5.4: Integrated profile of pulsar 47Tuc E created using all of the available observations (a) and using only the observations during favourable scintillation events (b). The second profile shows that the peaks of the profile are three and not two as appears in the first profile and they all become much more clear. Also the polarization information becomes much more significative.

2   Measure of Faraday rotation

As I have described in the pulsar overview chapter, the Faraday rotation of the electromagnetic radiation can be measured as a frequency-dependant rotation of the polarization position angle (PA) by the formula:

$$\Delta PA = \lambda^2 \times \text{RM} = c^2 \text{RM} \frac{1}{f^2}, \tag{5.1}$$

where RM is the *rotation measure* defined as:

$$RM = \frac{e^3}{2\pi m_e^2 c^4} \int_0^d n_e B_\parallel dl. \tag{5.2}$$

To measure the RM of a pulsar there are two different ways. The first, based on equation 5.1, consists in measuring the polarization position angle of the radiation at different frequencies and then searching for the best RM that fits the data. The second method uses the concept that summing different frequencies with the polarization angle wrongly rotated, ultimately depolarizes the profile and worsens the SNR of the polarized component. Hence the idea of correcting the signal for different RMs and then choosing the one that maximizes the polarization of the profile.

To obtain a more precise measure of RM, it is possible to calculate it in both ways and, since the two methods work in independent ways, average the result.

2.1   RMFIT

A software that allows the measure of RM is included in *psrchive* and it's called *rmfit*. This software can measure the rotation measure in both ways described above. However the procedure that fits the position angle at different frequencies is not very precise and so I have chosen to write a new code to obtain this measure. Still, this procedure can give us an approximate idea of what the RM is. Once we have this estimate of RM the best way to proceed is to correct the data with this quantity using the option -R of the software *pam*. As we have previously said, the Faraday rotation can depolarize the signal. Correcting for a value of RM close to the real one can cause the polarization of the signal to grow and allow us a more accurate measure. If this procedure fails to converge to a result it is highly probable that also the code that I have written will not give a measure of RM, so this procedure is also indicative of whether the pulsar should be further analyzed.

Instead, the procedure in *psrchive* that uses the second method to determine the amount of Faraday rotation works correctly. An example of this procedure can be seen in fig. 5.5. This procedure is not always applicable as it requires a significant polarization percentage and a high SNR, otherwise the change in polarization as RM changes is not appreciable.
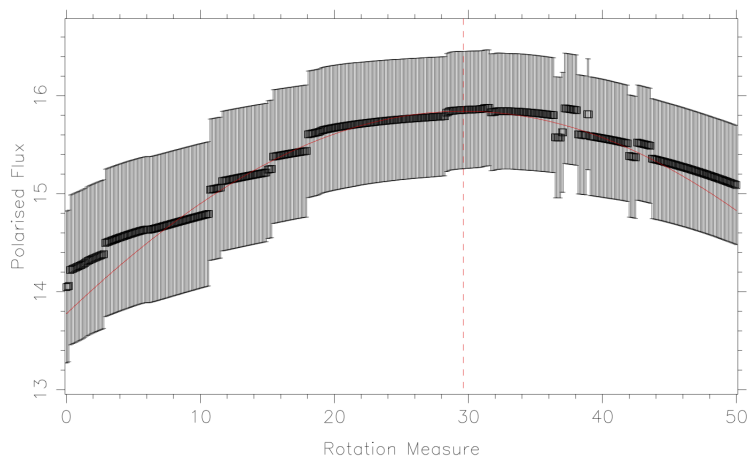
Figure 5.5: Example of the result of a RM fit using *rmfit*. The program calculates the RM in the second method described in the text. The data is from the pulsar 47Tuc E. On the x-axis the rotation measure is in units of rad/m^2, the polarized flux on the y-axis is in units of mJy. The program calculates the total polarized flux of the profile for the different values of RM. It returns as the result the RM (shown with the red dotted line) with the maximum value of the flux after performing a fit (red line). In this case the best RM is (27.8 ± 3.6) rad/m^2.

2.2   RM code

In order to obtain a more reliable measure of the Faraday rotation, following the prescriptions in Noutsos et al. (2008) and in Tiburzi et al. (2013), I have written a code in the programming language Python (it will be reported in the appendix). Now I will describe how this code works.

Other than the profile (which had to be converted in the .txt format to be read by Python) my code accepts as input the phase of the location of the pulse and the phase of the off-pulse region i.e. a region in which there is no signal (this will be used to measure the noise statistics). There are ways to automatically find where the profile is but they only work well if the profile has a single peak and the linear polarization peak is aligned with the total intensity peak. This rarely happens and so I decided to select the region of the pulse by hand. To select it I looked at the profile and chose the interval of phase around the linear polarization peak. From the off-pulse region I measure the root mean square of the noise of the total intensity.

The next step is to measure the polarisation position angle for each frequency channel. To do this I summed all the phase bins in the pulse region to enhance the signal and used the formula:

$$\text{PA} = \frac{1}{2} \arctan \left(\frac{\sum_{i=n_{start}}^{n_{end}} U_i}{\sum_{i=n_{start}}^{n_{end}} Q_i} \right), \tag{5.3}$$

where U_i and Q_i are the Stokes parameters U and Q for each bin of the profile and n_{start} and n_{end} are the start and end bin of the pulse region.

To calculate the error bars of this measure we first need to measure the linear polarization. Also in this case I sum the values of all the bins together to enhance the signal. The formula used is:

$$L_{meas} = \sqrt{\left(\sum_{i=n_{start}}^{n_{end}} U_i \right)^2 + \left(\sum_{i=n_{start}}^{n_{end}} Q_i \right)^2}. \tag{5.4}$$

However this value is not the true linear polarization of the pulse because both U and Q are affected by noise and since L_{meas} is defined as the sum in quadrature of U and Q it is positively biased. To remove this bias level I follow the prescription of Wardle and Kronberg (1974) and calculate $p_0 = L_{meas}/(rms(I)\sqrt{n_{pulse}})$, where $rms(I)$ is the root mean square of the total intensity measured in the off-pulse region and n_{pulse} is the number of bins in the pulse region. The true value of L is:

$$L_{true} = \begin{cases} 0.0 & \text{if } p_0 < 2.0 \\ \sqrt{L_{meas}^2 - (rms(I)\sqrt{n_{pulse}})^2} & \text{otherwise} \end{cases}. \tag{5.5}$$

Simmons and Stewart (1985) showed that this correction is the best to use when $p_0 > 0.7$.

Once we have measured the true linear polarization of the profile we can proceed with the measure of the errors on the position angle. The formula to use depends on the strength of the linear polarization. This can be determined by measuring $P_0 = L_{true}/(rms(I)\sqrt{n_{pulse}})$; if P_0 is bigger then 10 we can use the formula by Everett and Weisberg (2001) based on the assumption that the underlying distribution is a gaussian:

$$\sigma_{PA} = \frac{1}{2P_0} \tag{5.6}$$

If instead the value of P_0 is lower then the assumption of a normal distribution is not valid and we need to use the real distribution function, described in Naghizadeh-Khouei and Clarke (1993), which is:

$$G(\text{PA} - \text{PA}_{\text{true}}; \text{P}_0) = \frac{1}{\sqrt{\pi}} \left(\frac{1}{\sqrt{\pi}} + \eta_0 e^{\eta_0^2} [1 + \text{erf}(\eta_0)] \right) e^{-\text{P}_0^2/2} \tag{5.7}$$

where PA_{true} is the measured value of PA, $\eta_0 = (P_0/\sqrt{2}) \cos 2(\text{PA} - \text{PA}_{\text{true}})$ and erf is the Gaussian error function. Since this distribution function is not analytically integrable, we need to find the value of σ_{PA} so that the integral (computed numerically) between $\text{PA}_{\text{true}} - \sigma_{\text{PA}}$ and $\text{PA}_{\text{true}} + \sigma_{\text{PA}}$ is 0.683.

Once we have obtained the position angles and their errors for all the frequency channels then we can perform the fit to find the value of RM. I have chosen to use a least square fitting procedure internal in python and the function to fit was:

$$\text{PA}(\lambda) = \text{RM}\lambda^2 + \text{k}, \tag{5.8}$$

where k is a constant that measures the shift of the position angle from the reference value at zero wavelength (or infinite frequency). An example of the fit and its result is shown in fig.5.6.
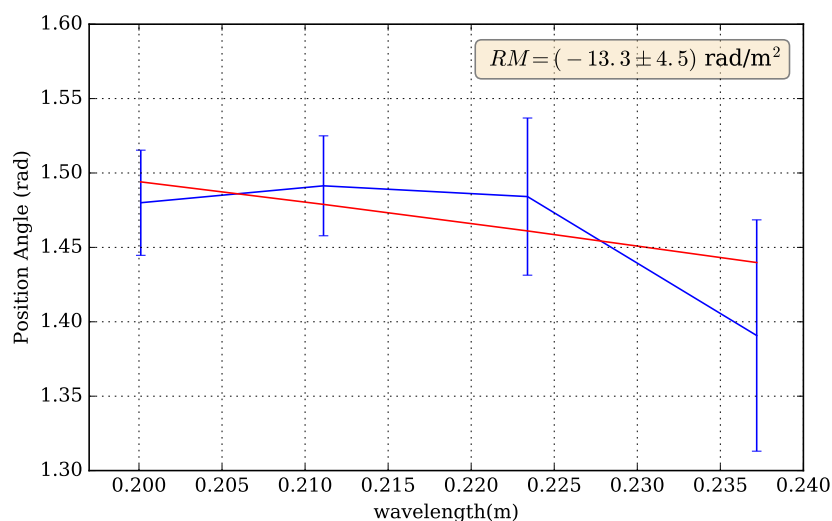

Figure 5.6: Example of the estimation of RM with my code. The data is from the pulsar 47Tuc J. The archive was previously corrected for $\text{RM} = -10\,\text{rad/m}^2$ and the result of the fit is $\text{RM} = (-3.3 \pm 4.5)\,\text{rad/m}^2$. The value shown in the figure is the real value of the RM.

In performing this fit we can sometimes have problems due to the periodicity of the position angle, which is periodic in π radians. If the value of RM is high enough, or the frequency band is large enough, it is possible that the shift of the position angle between adjacent sub-bands becomes larger than π. If this happens there will be a jump in PA of π. To fix this we can either adjust the position angles by adding the value π to every point after the jump or by modifying the fitting

function to replicate the jumps. If the frequency channels are very few and the errors are very big then another problem can occur: the fitting procedure can find a RM value (sometimes also accurate) which is very wrong because tries to fit a jump where there is none or inversely misses a jump where there is one. A way to proceed to correct this effect is to calculate an approximate value of RM with rmfit (which checks for this effect) and then apply this value to the data. In this way the residual RM should be small and so we do not expect any jumps or, if there are, they should be very visible and easy to fit.

Sometimes it is not possible to select a single pulse profile because the profile has more than one peak and trying to select them all within a single region would necessary insert a lot of noise and reduce the signal. Moreover it is not advisable because if there is a jump of $\pi/2$ in the polarization angle as described by the OPM model (McKinnon and Stinebring 2000), summing different bins with orthogonal polarization would end up reducing the polarization value. Furthermore if there is a global change in the position angle across the phase of the profile, as suggested by the RVM (Radhakrishnan and Cook 1969), adding signal from all the profile would lead to bigger errors.

So, following Ho et al. (2013), I decided (when possible) to divide the pulse region in smaller regions and calculate the PA and σ_{PA} for each subregion. Then I performed a simultaneous fitting procedure to find the best RM. For pulsars with different peaks I tried to measure the PA and σ_{PA} for the different peaks and performed the same simultaneous fit. This method did not always give satisfying results as the signal to noise ratio of the polarization in each subregion was too low and the fit failed.

3 Polarization percentages

Another important quantity to consider when studying the polarization of pulsars is the percentage of linear and circular polarization. This procedure for deriving those quantities follows Tiburzi et al. (2013). To measure them as accurately as possible I corrected for the RM measured and summed all frequencies together. For the pulsars for which I was not able to measure the RM I set it 0 and summed all frequencies.

First, I measured the total intensity of the profile by summing the values for I in the pulse region and dividing it by the total number of the bins in the profile. The error is obtained by measuring the root mean square of the off pulse region and multiplying it by $\sqrt{n_{pulse}}/n_{bin}$, where n_{pulse} is the number of bins in the pulse and n_{bin} is the total number of bins of the profile.

To measure the linear polarization percentage I calculated the linear polarization, L, for all the single bins of the profile. Then I applied the same de-bias method of Wardle and Kronberg (1974) and I separated the pulse region from the off-pulse region. A sample plot showing the selection of pulse and off-pulse regions can be seen in fig. 5.7. In the pulse region I summed all the values together and divided by the total number of bins. To measure the error, I calculated the root mean square of L in the off-pulse region and I multiplied it by the same factor used for the total intensity.

Next I calculated the percentage polarization of the absolute value of the circular polarization, $|V|$. Following Karastergiou and Johnston (2006) I measured the quantity $b = \sqrt{\frac{2}{\pi}}\mathrm{rms}(V)$, where rms(V) is the root mean square of V in the off-pulse region. The unbiased value for $|V|$ is:

$$|V|_{true} = \begin{cases} 0.0 & \text{if } |V|_{meas}/b < 2.0 \\ \sqrt{|V|_{meas}^2 - b^2} & \text{otherwise} \end{cases}. \tag{5.9}$$

The absolute value of the circular polarization is measured by summing all the values in the pulse region together and dividing it by n_{bin}. The error for this quantity is obtained with the equation: $\mathrm{rms(V)}\sqrt{\mathrm{n_{pulse}}}/\mathrm{n_{bin}}$.

Sometimes it is also interesting to measure the circular polarization keeping the sign, to do this I removed the bias value and obtained the true V using the formula:

$$V_{true} = \begin{cases} 0.0 & \text{if } |V|_{meas}/b < 2.0 \\ \sqrt{V_{meas}^2 - b^2} & \text{if } V_{meas}/b > 2.0 \\ -\sqrt{V_{meas}^2 - b^2} & \text{if } V_{meas}/b < -2.0 \end{cases} \quad . \tag{5.10}$$

The total value on the pulse and the error are calculated in the same way as the others.

Finally to obtain the percentages I divided all the quantities by the total intensity of the profile and multiplied them by 100.
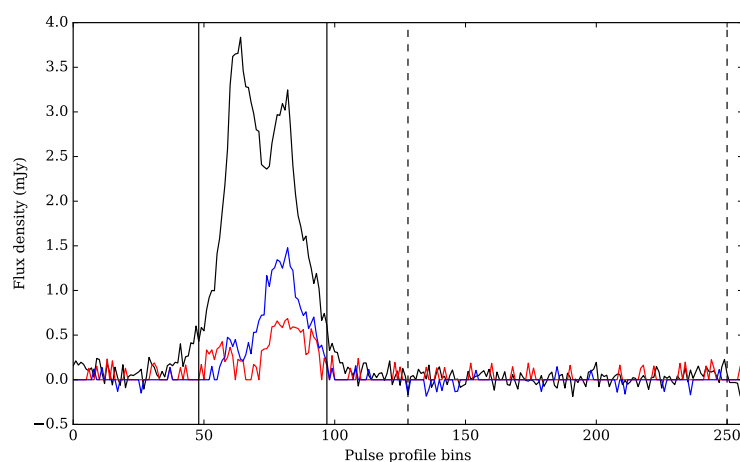

Figure 5.7: Profile of pulsar 47Tuc C with pulse and off-pulse regions highlighted. The pulse region is between the filled vertical lines. The off-pulse region used in this case is between the dashed vertical lines. The profile is shown in total intensity (black), linear polarization (red) and circular polarization (blue). The linear and circular polarization are corrected for the bias as described in the text above.

4   Monte Carlo simulation

When I first run the code and obtained the first results, I immediately noticed that the errors were bigger than those calculated with the same method with *rmfit* so I questioned wether my code was working in the correct manner. To test my code, I devised a Monte Carlo simulation (the code is reported in the appendix). In this simulation I create a profile with the same characteristics as the real one, I add a random noise of the same amplitude as the noise in the real profile and calculate the value of RM. After repeating these steps for 1000 times I measured the statistics of the

obtained distribution and draw conclusions that can be applied also to the real data. In this section I describe how the code works and the results that I was able to extract from the simulations.

4.1 Profile creation

To generate a simulated profile of the pulsars, I first created a noiseless template of the total intensity profile from the real data using the software *paas* from *psrchive*. This is an interactive software that allows us to fit analytically the profile with a set of gaussian. The user can select an approximate position, width and height of each gaussian and the software finds the parameters that best fit the profile. In the simulation I used this template as the profile in total intensity to which I later add the polarization information and the noise. To add the frequency information I created 4 (the number of frequencies used for the determination of RM) different profiles all from the same template and I assigned each profile with the frequency corresponding to the channel.

To create the profiles for the other Stokes parameters, I first visually divided the linear polarization profile in different components and measured the polarization percentage for each component with the code previously described. Since the real linear polarization profile is usually very noisy, it is very difficult to discern the real shape of the components, so I approximated them as gaussians. I measured how high the gaussian would have to be to have the observed percentage of polarization and generated a linear polarization profile combining all the components for each frequency.

Then I went on to generate the Stokes parameters U and Q. To do it I inverted the relations 4.23 and 4.24 to obtain the formulas:

$$Q = \sqrt{\frac{L^2}{\tan^2(2\text{PA}) + 1}} \times sgn(\cos(2\text{PA})) \tag{5.11}$$

$$U = Q \tan(2\text{PA}), \tag{5.12}$$

where PA is the position angle. The sign operator was added in the equation for Q as the square root only returns positive values while the Stokes parameter can also be negative. From these equations it appears we still need to determine the position angle of the polarization. The position angle depends on the value of RM and the frequency of observation by the formula 5.1. So, first I fixed a value of RM and measured the PA for each frequency channel and then I created the Q and U profiles.

This part of the code can be used to generate simulated profiles of all kind of pulsars provided that the real RM is given. Since we don't know the real RM of the pulsars we can assume that the approximate value we corrected for previously is correct and generate profiles with RM = 0. This might not be exact but, since the goal of the simulation is just to test the code and the errors found for RM, it should not affect the final results.

Another advantage of setting RM to 0 is that we don't have to worry about the jumps in PA as, even considering the possible noise, the angles should all be close to 0.

Lastly, I added some noise to make the simulated profile look more similar to the real one. I noticed that in the real data the noise level for the parameters I, Q and U was the same but it can vary for the different frequency channels. To recreate this I found the root mean square of the off-pulse region in the real profile for each channel and measured the mean and standard deviation of these values on the different channels, μ_{noise} and σ_{noise}. In the simulation I then extracted a value for the noise from a gaussian distribution centered at μ_{noise} with standard deviation σ_{noise}.

Once I have found the values for the standard deviation of the noise for each channel, I generated for each bin a noise value extracted from a gaussian distribution centered at 0 and with that standard deviation. Finally I added these values to the simulated profiles and obtained a realistic copy of the real profiles. An example can be seen in figure 5.8.

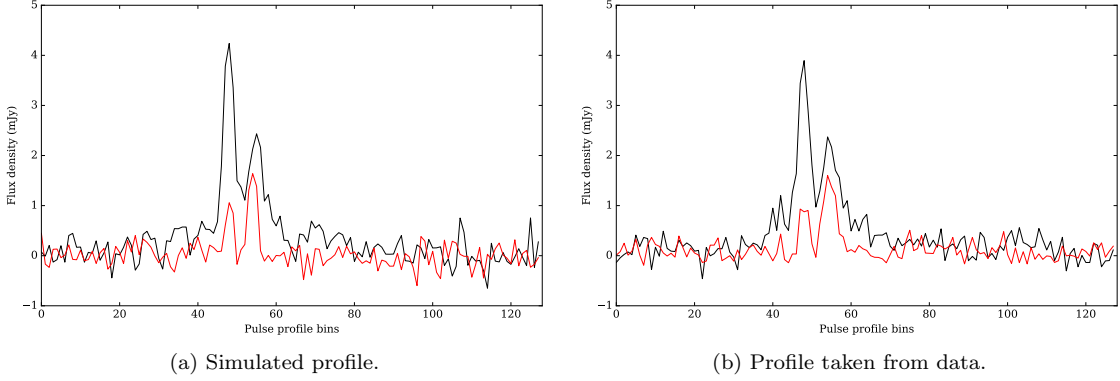(a) Simulated profile.   (b) Profile taken from data.

Figure 5.8: Example of a simulated profile (a) confronted with the profile taken from the data (b). The data is from pulsar 47Tuc G. The black line is the total intensity profile and the red line is the linear polarization. The simulated profile has the same value of flux density, polarization and noise.

In generating the profiles I have neglected the circular polarization, V. This was because it is not used in any way in the code to calculate RM.

4.2   Simulation set-up

After the profile has been created I calculated the RM using the same code that I used for the real data. I stored the resulting RM and corresponding error and repeated the process for 1000 times. To make the code go faster I did not repeat the entire profile creation process but I just added different values for the noise still extracted starting from the same μ_{noise} and σ_{noise}.

Since the simulation was still running slow, I examined the entire code to look for a way to make it run faster. I noticed that the slowest part was the measure of the error on the PA in which I had to perform a numerical integration and a minimization routine. The function that I had to integrate is (eq. 5.7):

$$G(\text{PA} - \text{PA}_{\text{true}}; \text{P}_0) = \frac{1}{\sqrt{\pi}} \left(\frac{1}{\sqrt{\pi}} + \eta_0 e^{\eta_0^2} [1 + \text{erf}(\eta_0)] \right) e^{-\text{P}_0^2/2}. \tag{5.13}$$

where $\eta_0 = (P_0/\sqrt{2}) \cos 2(\text{PA} - \text{PA}_{\text{true}})$. It has two parameters, PA_{true} and P_0, and a variable, PA, which I varied to look for σ_{PA}. The parameter PA_{true} is just a translation, while the parameter P_0 determines the height and width of the distribution.

This means that I could define a function that given the P_0 determines the value of σ_{PA} directly. To build this function I calculated σ_{PA} for different values of P_0 and performed a polynomial fit. Using the result of the fit I was able to measure the error on PA without having to repeat the

numerical integration every time. This made the code much lighter and therefore I was able to repeat the simulation for 1000 times in a short amount of time.
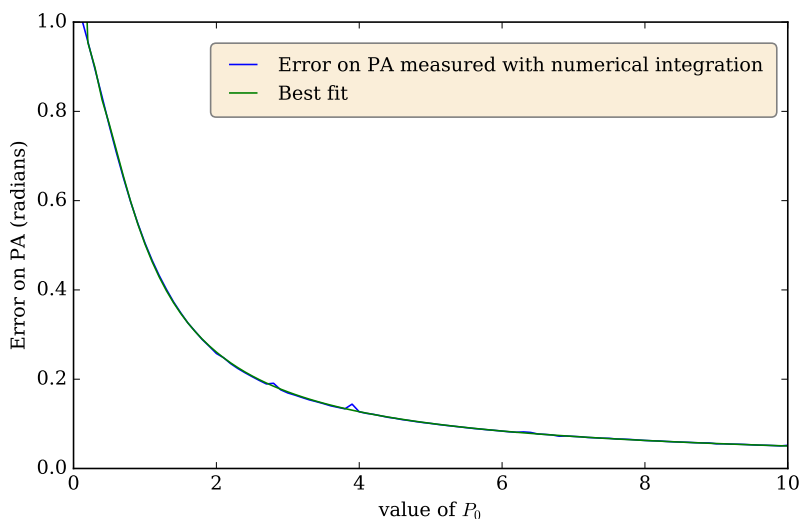

Figure 5.9: Plot of the values of the error on PA measured as a function of P_0. The green line is a polynomial fit up to the 6th order. The plot is truncated at $P_0 = 10$ because above that value I measured the error on PA following the prescription of Everett and Weisberg (2001).

4.3   Simulation results

Having obtained 1000 different values of RM I could perform some statistical analysis. I checked that the distribution of the different values followed a gaussian centered on the real value of 0 and measured the standard deviation. I can therefore assume that the real error that my code is able to achieve is this standard deviation.

   If the standard deviation of the distribution and the average value of the error of RM are similar it means that the code works correctly. After some debugging, the code showed to work nicely. An histogram with the results of a simulation on a pulsar is shown in fig. 5.10.

   Then I checked that these errors were compatible with those measured for the real pulsars.

   With this important results I concluded that my code was working in the right way and decided to take as error of the RM of the pulsars the standard deviation of the distribution resulting from the Monte Carlo simulation.
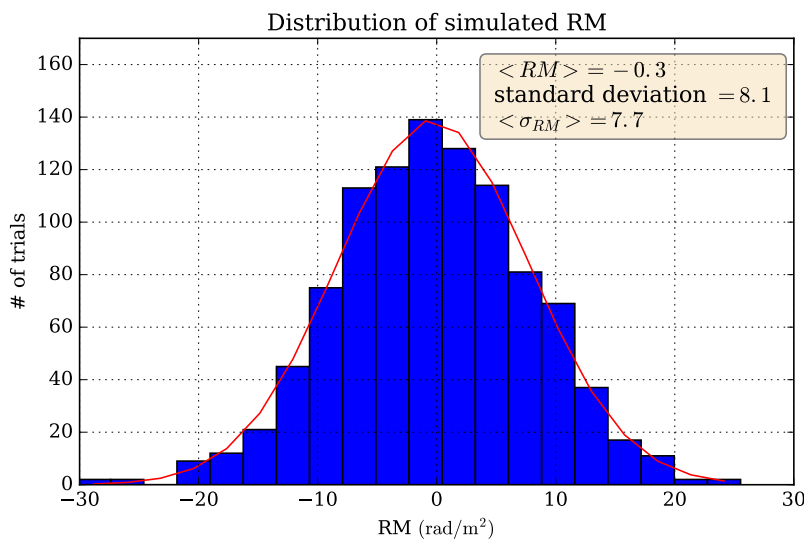
Figure 5.10: Histogram of the results of the simulation for pulsar 47Tuc F. The distribution is centered on the real value of RM (set to be 0 rad/m^2) and is fitted with a standard deviation of 8.1 rad/m^2. $< \sigma_{RM} >$ is the average of the errors of RM measured by the code at every trial and is 7.7 rad/m^2. These are very close to each other, this means that the code is working correctly.

5 Results

The results obtained with my code and with *rmfit* are shown in table 5.1. In the last column I performed, when possible, a weighted average of the two values. In table 5.2 I will report the measured flux, polarization percentages, final values of RM and average magnetic field along the line of sight. The position and RM measure of the pulsars are plotted in fig. 5.12.

5.1 Single profiles

C This pulsar has two peaks in the total intensity profile, the same structure is seen in the linear polarization profile but here the second peak is higher. In the circular polarization profile the first peak is barely visible while the second peak is dominant. The position angle varies along the profile but no clear trend is seen.

D The profile shows a single asymmetric peak sharper on the right. The linear polarization shows a small peak in correspondence with the highest part of the peak.

E This pulsar has three peaks in the total intensity profile. The first peak has very high linear polarization and a small negative component of circular polarization. The second peak appears to have two separated linear polarization signals. The third peak has high linear polarization and high positive circular polarization. The PA does not vary along the first peak while it appears to have orthogonal jumps in correspondence of the second and the third peak. This jumps could be

(a) Profile of 47 Tucanae C.

(b) Profile of 47 Tucanae D.

(c) Profile of 47 Tucanae E.

(d) Profile of 47 Tucanae F.
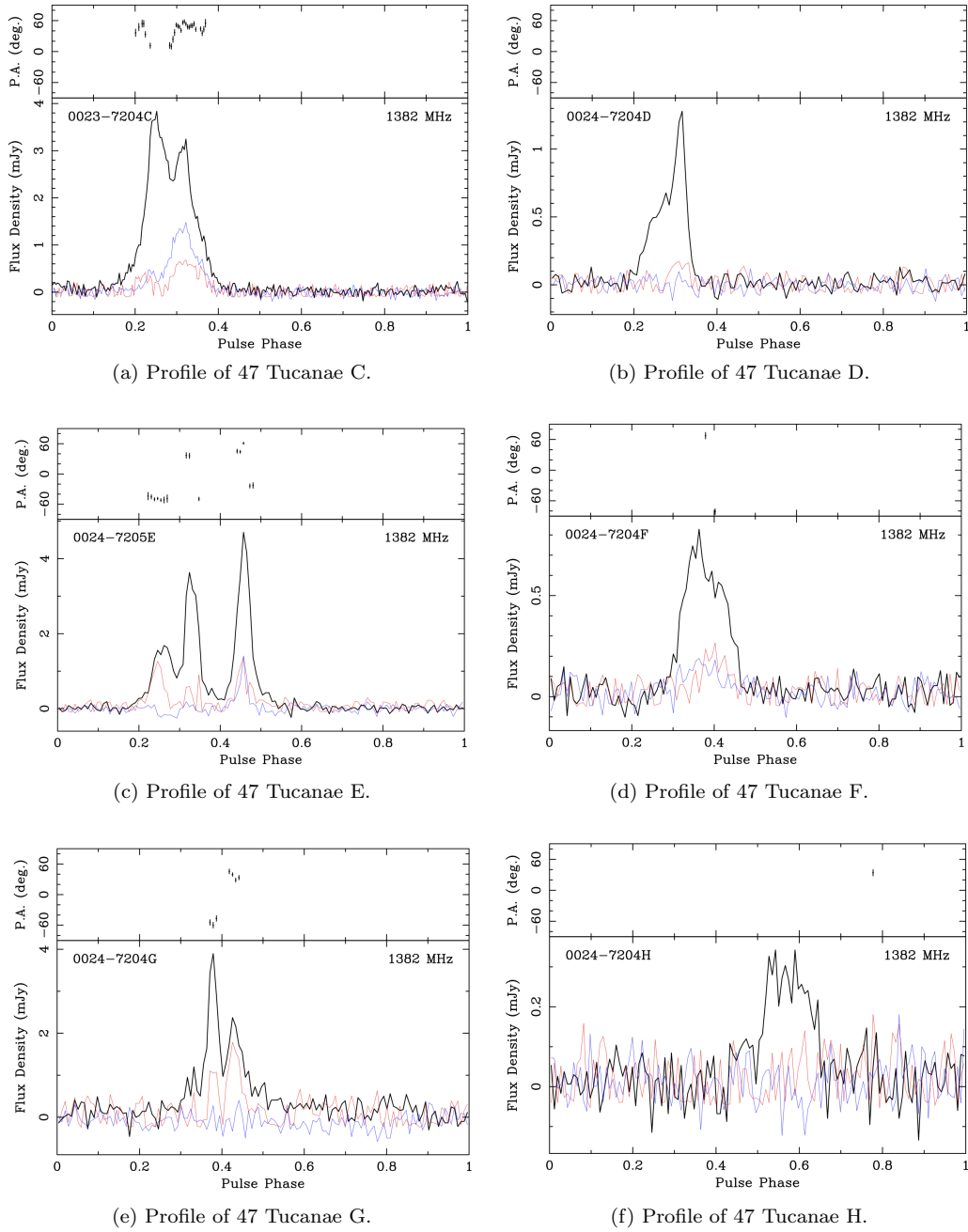
(e) Profile of 47 Tucanae G.

(f) Profile of 47 Tucanae H.

Figure 5.11: Polarization profiles of the pulsars detected in the observations. The top panel of each plot shows the PA variation from the celestial north as a function of pulse phase. The PAs are plotted only if the linear polarization is above 2σ The bottom plot shows the flux density of the integrated profile. The black line is the total intensity, the red line is the linear polarization and the blue line is the circular polarization. The center frequency of the observations is written on the left of the plot. The profile for the pulsars with measured RM are corrected for the measured value. Each profile is described in details in the text.
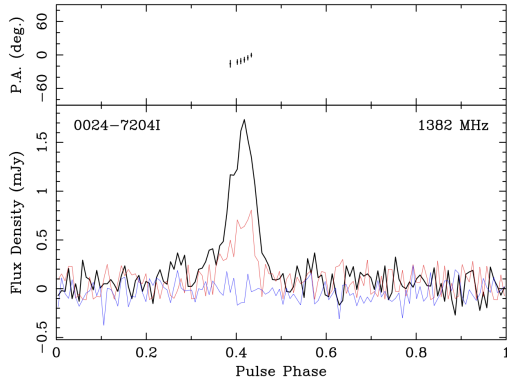
(a) Profile of 47 Tucanae I.
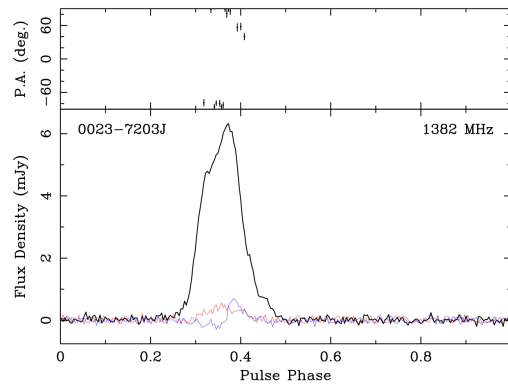
(b) Profile of 47 Tucanae J.
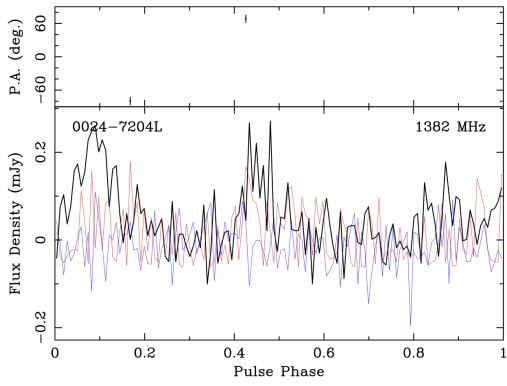
(c) Profile of 47 Tucanae L.

(d) Profile of 47 Tucanae M.

(e) Profile of 47 Tucanae N.

(f) Profile of 47 Tucanae O.

(a) Profile of 47 Tucanae Q.

(b) Profile of 47 Tucanae R.

(c) Profile of 47 Tucanae S.

(d) Profile of 47 Tucanae T.

(e) Profile of 47 Tucanae U.

(f) Profile of 47 Tucanae Y.

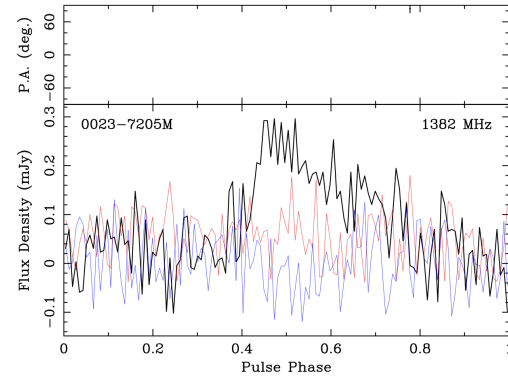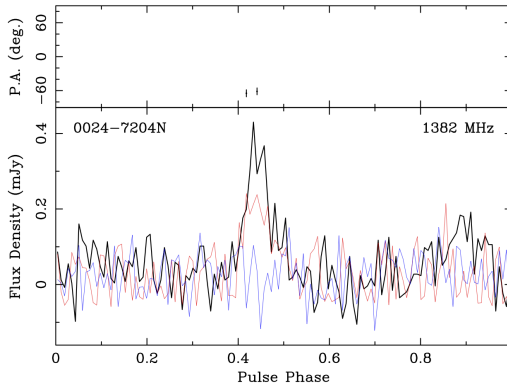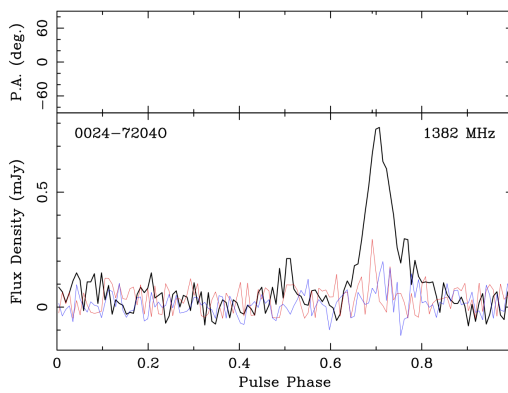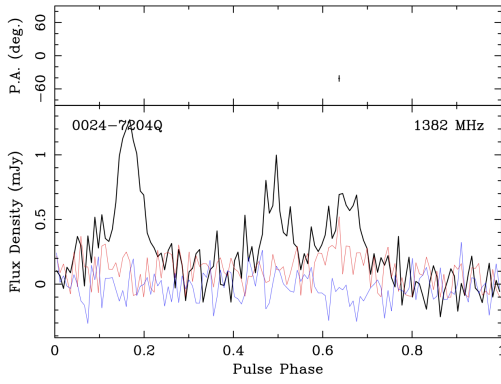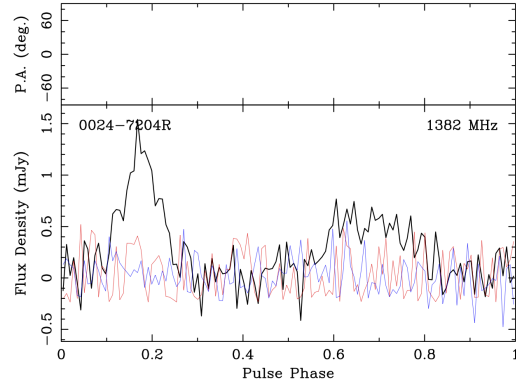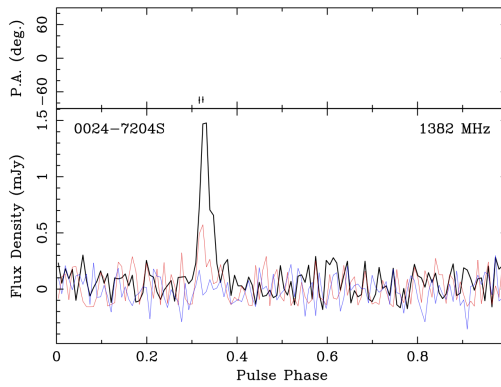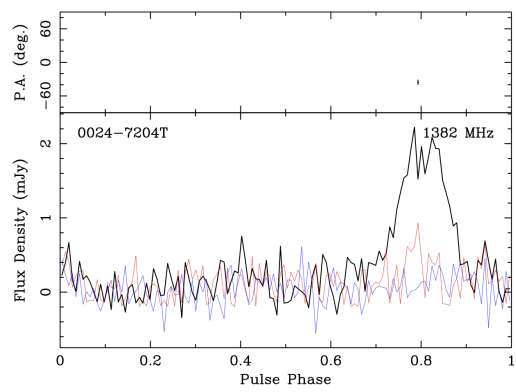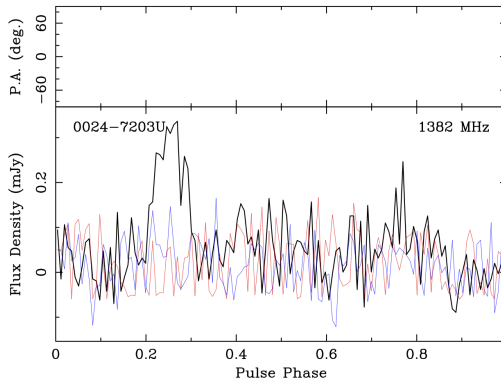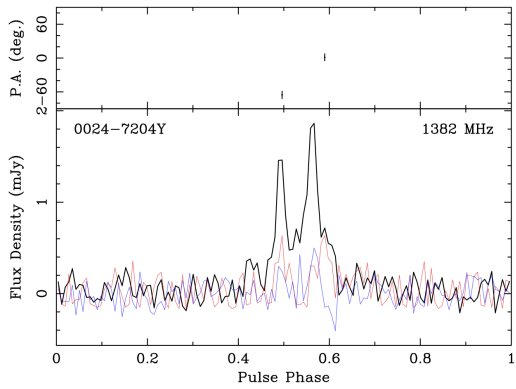| Name	My code (rad/m^2)	*rmfit* (rad/m^2)	Final results (rad/m^2)
C	34.1 ± 3.4 (sim)	28.0 ± 7.1	33.4 ± 2.4
D	11.8 ± 11.8 (sim)		11.8 ± 11.8
E	27.2 ± 3.1 (sim)	27.2 ± 3.2	27.2 ± 2.2
F	17.4 ± 8.1		17.4 ± 8.1
G	12.3 ± 8.0 (sim)	12.1 ± 12.9	12.2 ± 6.8
I	12.1 ± 8.1 (sim)	-3.0 ± 8.5	4.9 ± 5.8
J	-9.1 ± 3.1 (sim)		-9.1 ± 3.1
L	18.7 ± 11.0		18.7 ± 11.0
N	-0.4 ± 7.5 (sim)		-0.4 ± 7.5
O		23.8 ± 17.0	23.8 ± 17.0
Q	-9.1 ± 9.9		-9.1 ± 9.9
T	14.5 ± 16.4	8.7 ± 20	12.2 ± 12.7
Y	-6.3 ± 13.0	16.0 ± 13.6	4.3 ± 9.4

Table 5.1: Results of the RM analysis. Only the pulsars with measured RM are reported in the table. In the second column I show the results obtained with my code. They are obtained with a single peak fit except for the pulsars with written (sim). For those I performed a simultaneous fit between different parts of the profile. In the third column I show the results obtained with the program *rmfit*. In the last column I reported the final results obtained with a weighted average between the two preceding results.

explained with the OPM (McKinnon and Stinebring 2000) but the number of points is too small to be sure.

F The profile shows a large single peak with linear and circular polarization of about the same intensity.

G The pulsar has two close peaks in total intensity with the leading peak showing a higher flux. The linear polarization follows the two peaks but in this case the trailing peak has higher values. There is no significant circular polarization. The PAs of the two peaks appear to be orthogonal.

H The pulsar has a single broad profile. No significant polarization is seen.

I This pulsar has a single profile slightly asymmetric. The linear polarization is very high showing the same profile as the total intensity while the circular polarization is not significant. The PAs vary along a line that could be described in the context of the RVM (Radhakrishnan and Cook 1969) but is also consistent with a straight line.

J The profile shows a very bright single peak with small amounts of linear polarization. The circular polarization varies from negative in the first half of the profile to positive in the second half. The position angles vary from $-80°$ to $\sim 60°$ along a curve that could be described by the RVM (Radhakrishnan and Cook 1969).

L The total intensity profile shows two distant peaks. Only the second peak is polarized with very high levels of linear polarization. No circular polarization is detected.

M The pulsar shows a very broad and asymmetric profile. No significant polarization is detected.

N The pulsar presents a very bright peak and a barely detectable second peak opposite in phase which could be interpreted as an interpulse. The first peak has very high levels of linear polarization, but no significant circular polarization. The PAs stay roughly constant along the phases.

O The profile has a single symmetrical peak. The linear polarization is not constant along the peak but has a very sharp spike near the center of the profile.

Q The profile shows three peaks, one is brighter and isolated while the other two are close together. The separation between the first peak and the third peak is almost 0.5 in phase, so it might be an interpulse. The first and the second peaks are not linearly polarized while the third peak is.

R The pulsar two peaks in total intensity. They can be interpreted as a main pulse and an interpulse. None of the peaks show significant polarization.

S The pulsar shows a very sharp single peak with some linear polarization. There is no apparent circular polarization.

T This profile has a single large peak. There is some linear polarization in the central regions of the peak but no significant circular polarization.

U The pulsar shows a single peak. In a previous work (Camilo et al. 2000) this pulsar showed an interpulse. Though there may be some sings of it around the phase 0.7-0.8 it is not clearly detected. The profile shows no significant polarization.

Y The profile shows two close peaks both with some amount of linear polarization. The second peak shows evidence of circular polarization.

Name	S (mJy)	L per cent	V per cent	$\lvert V \rvert$ per cent	RM (rad/m^2)	$\langle B_\parallel \rangle (\mu\text{G})$
C	0.42 ± 0.01	15.4 ± 0.4	27.1 ± 0.2	27.1 ± 0.3	33.4 ± 2.4	1.36 ± 0.10
D	0.061 ± 0.004	13.3 ± 1.8	-0.2 ± 1.0	2.6 ± 1.1	11.8 ± 11.8	0.48 ± 0.48
E	0.45 ± 0.01	27.4 ± 1.1	4.2 ± 0.5	9.8 ± 0.5	27.2 ± 2.2	1.12 ± 0.09
F	0.080 ± 0.006	18.7 ± 1.8	17.4 ± 1.1	17.4 ± 1.6	17.4 ± 8.1	0.71 ± 0.33
G	0.20 ± 0.02	44.1 ± 2.4	-1.6 ± 1.5	5.7 ± 1.7	12.2 ± 6.8	0.50 ± 0.28
H	0.036 ± 0.005	13.1 ± 4.7	-5.1 ± 2.3	5.1 ± 3.6		
I	0.12 ± 0.01	46.0 ± 1.7	-1.1 ± 1.4	1.1 ± 1.7	4.9 ± 5.8	0.20 ± 0.24
J	0.643 ± 0.007	5.9 ± 0.2	2.0 ± 0.1	4.8 ± 0.2	-9.1 ± 3.1	-0.37 ± 0.13
L	0.011 ± 0.004	55.9 ± 10.2	-6.5 ± 6.2	6.5 ± 7.5	18.7 ± 11.0	0.77 ± 0.45
M	0.06 ± 0.01	12.3 ± 3.7	-2.2 ± 2.0	12.3 ± 2.6		
N	0.024 ± 0.005	62.7 ± 5.4	7.9 ± 2.6	15.1 ± 5.2	-0.4 ± 5.6	-0.02 ± 0.23
O	0.060 ± 0.006	9.8 ± 1.6	11.6 ± 1.1	14.8 ± 1.7	23.8 ± 17.0	0.98 ± 0.70
Q	0.12 ± 0.02	23.5 ± 3.4	-1.8 ± 1.7	7.3 ± 2.8	-9.1 ± 9.9	-0.38 ± 0.41
S	0.044 ± 0.009	24.3 ± 3.7	0.0 ± 3.0	0.0 ± 3.5		
T	0.26 ± 0.03	15.7 ± 1.9	5.1 ± 1.5	5.1 ± 2.2	12.2 ± 12.7	0.50 ± 0.52
U	0.024 ± 0.006	0.0 ± 5.1	8.9 ± 2.2	8.9 ± 3.8		
Y	0.12 ± 0.01	23.7 ± 3.5	12.8 ± 1.4	12.8 ± 2.1	4.3 ± 9.4	0.18 ± 0.38

Table 5.2: Summary of the main results of the analysis. The second column (S) is the total intensity flux. The columns L per cent, V per cent and $\lvert V \rvert$ per cent are percentages of the the linear, circular and the absolute value for the circular polarizations. The column RM is the value of the Faraday rotation measure and $\langle B_{parallel} \rangle$ is the average value of the parallel component of the magnetic field. For the total intensity flux the error presented is at 3σ, for all the other quantities is at 1σ.
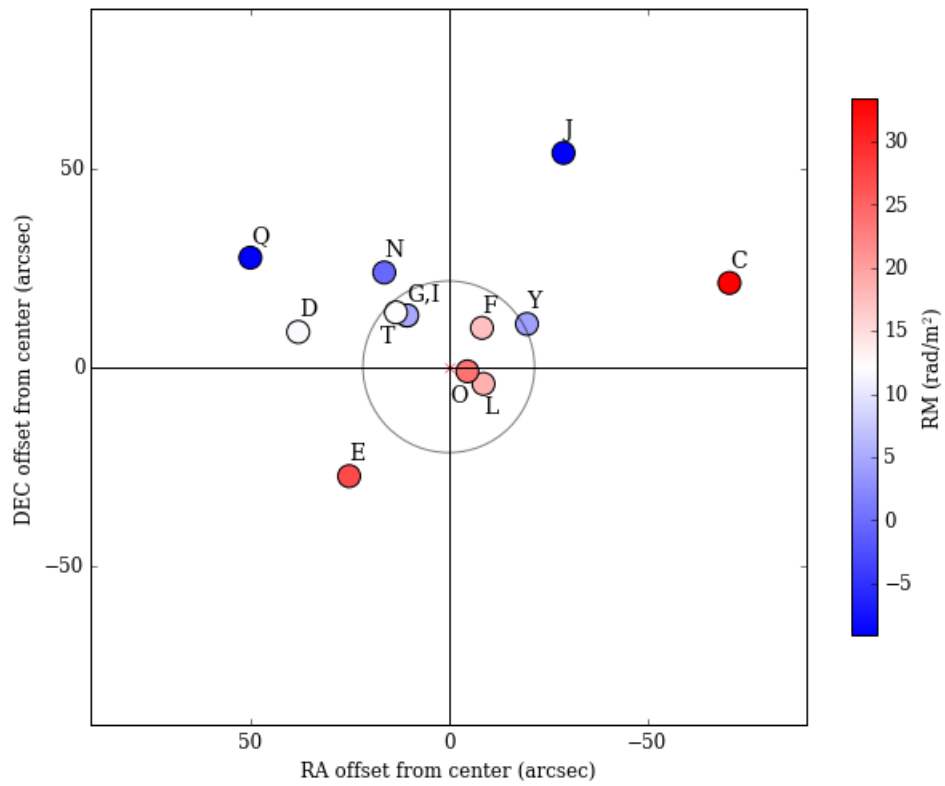
Figure 5.12: Plot representing the position inside the cluster and values of RM for the pulsars for which the Faraday rotation was measured. The position of the center is taken from McLaughlin et al. (2006).

Chapter 6

Magnetic field considerations

The results presented in the previous chapter show that there is some scatter between the measured values of RM, well outside the statistical errors, thus we conclude that there is a difference in magnetic field along the different lines of sight toward the examined pulsars. In this chapter I will first plot the results as a function of different quantities to check if some clear relation can be recovered. Then I will study the possible origins of the observed magnetic field differences which may be due to the Galactic contribution or to the globular cluster itself.

1   RM plots

From the correct timing solutions of the pulsars we can derive many parameters (as described in a previous chapter) like the value of the dispersion measure, the angular coordinates and the line of sight acceleration (obtained by dividing the period derivative with the period). Using these parameters we can look for different relations and test different hypotheses on the origin of the RM variations.

To investigate if the RM variations are due to a magnetic field and not to variations in the electron density (reflected in DM variations), I plot a graph showing the measured RM as a function of DM (see fig. 6.1). In this plot we don't see any clear correlation between the two sets. There seems to be a decreasing trend in the central region of the plot but it is not statistically relevant.

Since there is no clear trend in the data we can conclude that the variations of RM are not primarily caused by fluctuations of the electron column density along the line of sight. This is because such fluctuations would contribute equally to the DM and to the RM. Instead the data suggests that there might be a variation in magnetic field along the different lines of sight. However from this plot we cannot conclude whether the variations in the magnetic field are located inside the cluster or in the Galactic medium along the line of sight.

A method for investigating if the magnetic field is constrained inside the cluster is to study the correlation with the angular separation from the center. From the plot (see fig. 6.2) we see that there seems to be a constant decrease in the inner 30" but it is not statistically relevant. Outside, the values vary significantly but not in a clear pattern. Because of the high statistical errors and of the small angular scales probed this plot is inconclusive and we cannot gain useful informations from it.
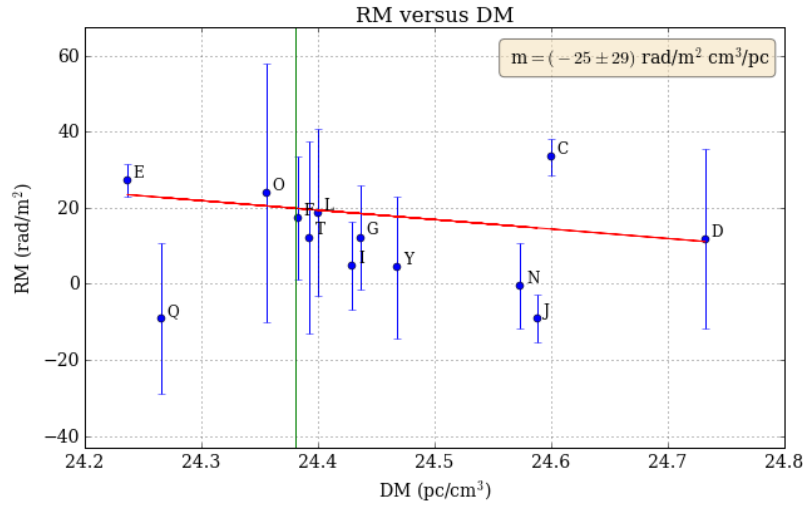
Figure 6.1: Plot of RM as a function of DM. The green line is at the value of DM at the center of the cluster as measured by Freire et al. (2001b). The red line is the best straight line fit through the data. m is the angular coefficient of the fit. Since it is compatible with zero no correlation can be determined. The errors are at two sigma. For a detailed description of this plot see the text.

Figure 6.2: Plot of RM as a function of angular separation from the center. The position of the center is taken from McLaughlin et al. (2006). The red line is the best straight line fit through the data. m is the angular coefficient of the fit. Since it is compatible with zero no correlation can be determined. The errors are at two sigma. For a detailed description of this plot see the text.

Other useful informations can be gained by looking at the values of RM as a function of the position in the sky, starting with the simplest option of looking for correlations with the declination and the right ascension (see figs. 6.3 and 6.4).

In the plot 6.3 we can see that all values except for the pulsar C could be fit with a straight line decreasing with increasing declination. The outlier, however, has the smallest statistical error and there is no reason to exclude it. Thus, similarly with the case of plot 6.4 we don't see any clear correlation.

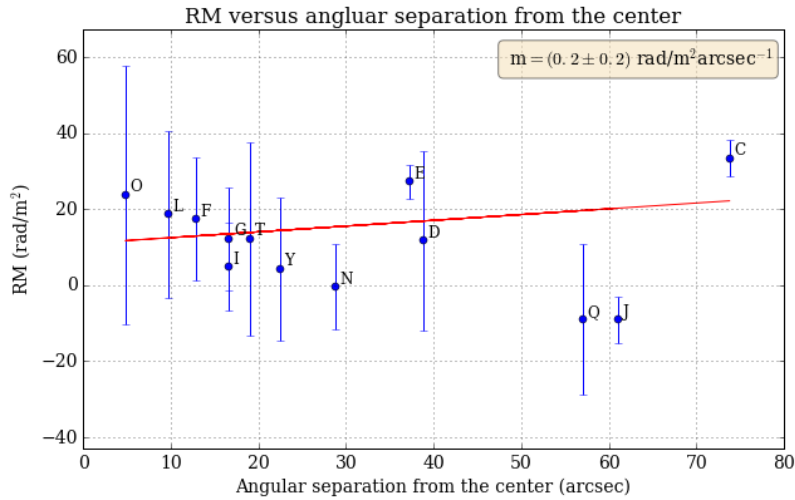

Figure 6.3: Plot of RM as a function of the declination offset from the center of the cluster (represented by the green line). The position of the center is taken from McLaughlin et al. (2006). The red line is the best straight line fit through the data. m is the angular coefficient of the fit. This value is not compatible with zero but the reduced chi square of the correlation is ~ 9 with 11 degrees of freedom. The probability of a random distribution producing a similar value is almost 100%, thus this correlation is statistically irrelevant. The errors are at two sigma. For a detailed description of this plot see the text.

The last parameter I will check the correlation with, is the line of sight acceleration. This can be recovered by taking the derivative of the relation $v_{los}/c = \Delta P/P$, where v_{los} is line of sight component of the velocity and ΔP is the difference between the observed period and the intrinsic period. The line of sight acceleration will therefore be described by $a_{los}/c = \dot{P}/P$. This value is biased by the intrinsic period derivatives of the pulsars but we can assume it has a constant value for all pulsars. Freire et al. (2001b) used this relation to show that pulsars in the far side of the cluster have higher DM, I will try to do the same using the RMs (see fig. 6.5). In this plot we can divide the pulsars on the far side from the pulsars on the near side and check whether there is a significant difference between the two sets. Since no significant difference is evident, there probably is no constant magnetic field in the portion of the cluster hosting the pulsars.
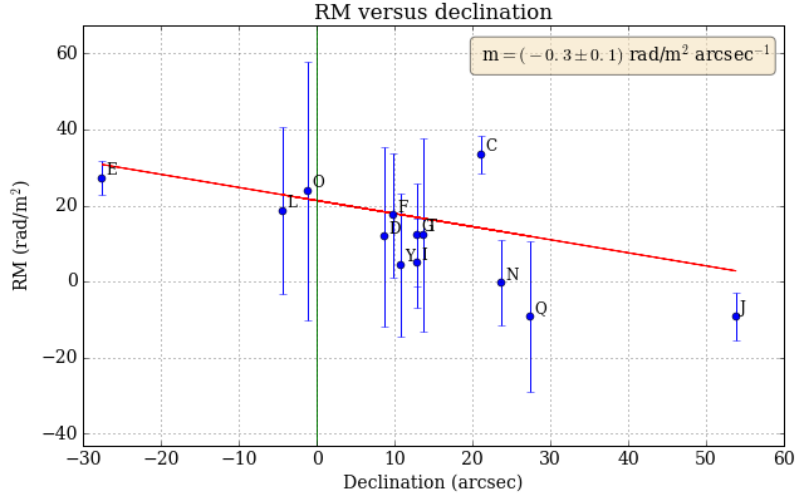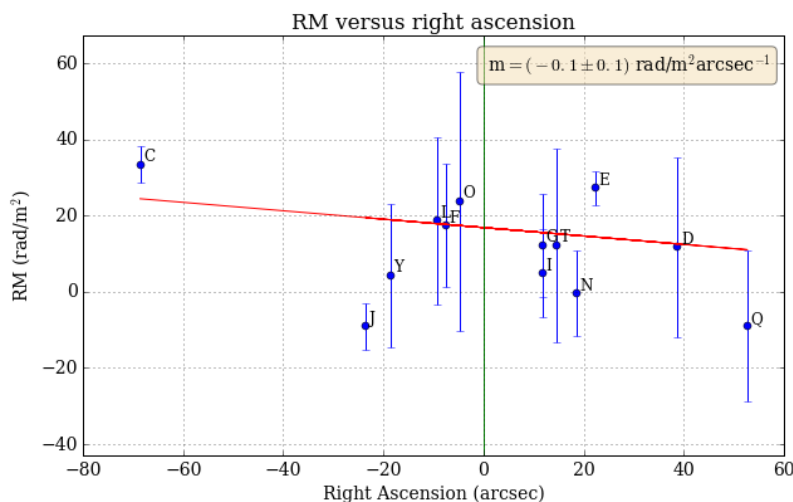
Figure 6.4: Plot of RM as a function of the right ascension offset from the center of the cluster (represented by the green line). The position of the center is taken from McLaughlin et al. (2006). The red line is the best straight line fit through the data. m is the angular coefficient of the fit. Since it is compatible with zero no correlation can be determined. The errors are at two sigma. For a detailed description of this plot see the text.

1.1 Structure function

When studying the Faraday rotation of different sources, a typical analysis made is the structure function (Haverkorn et al. 2008, Roy et al. 2008). The structure function is measured by calculating the average of the square of the differences of RM for each pair of pulsars within a certain range of angular separation. This function has been used to study the turbulent nature of the small-scale Galactic magnetic field. It is usually fitted with broken power laws and, from the spectral indices and the angular scales of the breaks, the intensity and the inner and outer scales of turbulence are constrained.

Because of the large angular separations between extragalactic sources, the structure function has usually been measured only on large scales. A recent work (Ho et al. 2013), similar to mine, has measured the structure function measuring the RMs of the pulsars in the globular cluster Terzan 5 and obtained that it could be fit with a power law of spectral index $\alpha = 1.15 \pm 0.25$.

The results for 47 Tucanae are shown in fig. 6.6. The errors on the values of ΔRM are too big to reveal any dependance. The spectral index resulting from the power law fit has an error that is so big that it cannot comunicate any information. In summary no conclusion on the structure function of 47 Tucanae can be obtained with the available data.

2 Detection of a gradient

From the previous tests we can only conclude that in the cluster there is no homogeneous magnetic field in the region where the pulsars reside; all other tests were inconclusive. However careful
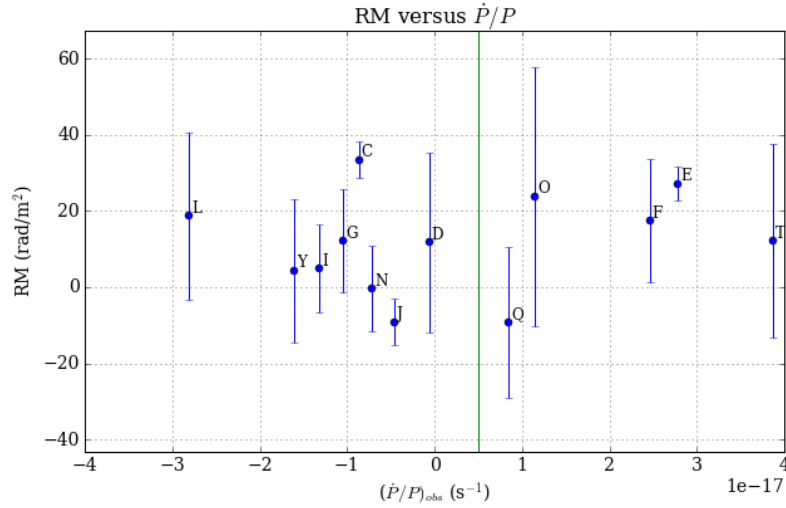
Figure 6.5: Plot of RM as a function of $\dot{P}/P$ which is linked to the line of sight acceleration of the pulsars. The green line is the assumed value of $\dot{P}/P$ intrinsic to every pulsar taken from Freire et al. (2001b). The pulsars on the left should be in the far side of the cluster while the pulsars on the right should be in the near side. The errors are at two sigma. For a detailed description of this plot see the text.
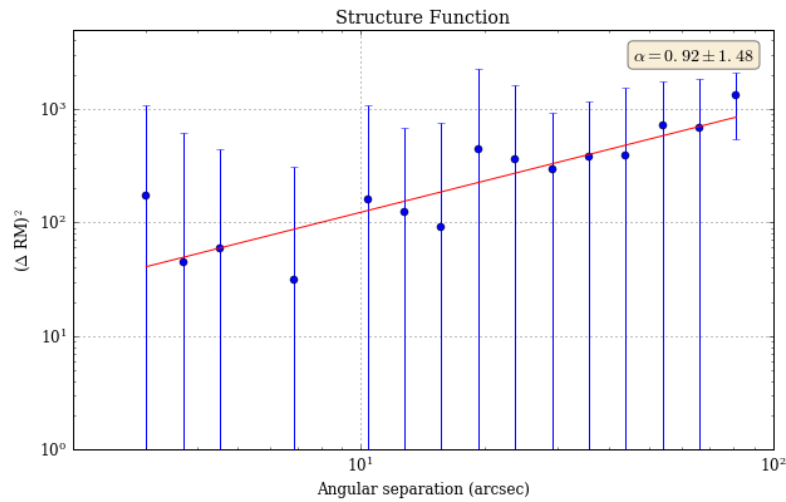
Figure 6.6: Structure function of the RMs of the different pulsars. α is the spectral index of the power law fit. The errors are at two sigma. For a detailed description of the plot see the text.

examination of fig. 5.12 shows that there is a trend of RM along the diagonal passing through the second and forth quadrant.

To test whether there is a correlation along that line and to check what is the angle at which the correlation is higher I wrote a piece of code in Python. This code requires an angle as input, the angle is set to 0 in the East direction (positive RA) and increases clockwise towards the North direction (positive DEC) (notice that in the plot the East direction is to the left). The code then measures the orthogonal projections of the position of the pulsars with respect to a line perpendicular to the assigned direction and passing through the center of 47 Tucanae. The length of the projection (with its sign) is used as input for the x-axis of the plots. After that, I fit the resulting data with a straight line and measure the reduced chi square of the fit. Using a minimization algorithm in Python I looked for the angle for which the reduced chi square was smaller.

The angle with the minimum reduced chi square is $\sim 59°$ with a reduced chi square of 0.725 with 11 degrees of freedom (the probability of correlation is $\sim 70\%$). The plot 6.7 shows the data resulting from the choice of the angle and the best straight line fit along this direction. The gradient of RM results (-0.74 ± 0.05) rad/m^2/arcsec, while the RM for the center of the cluster is (19 ± 1)rad/m^2 This line fits the data well as it passes through the two sigma uncertainty bars for all the data.
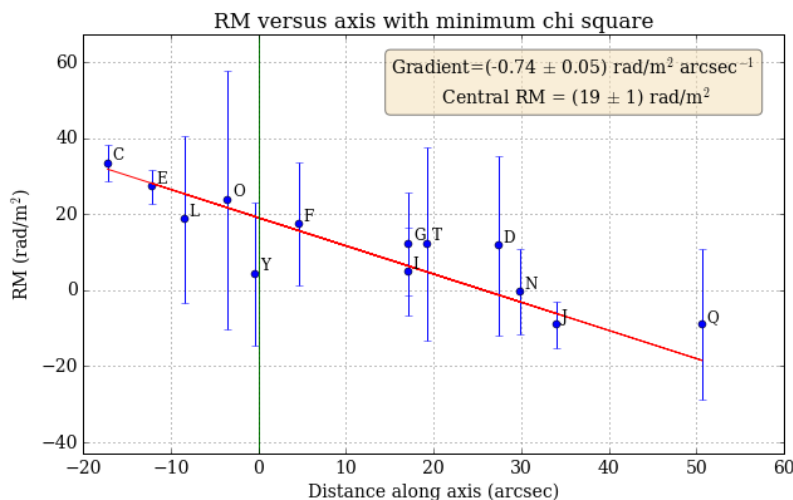
Figure 6.7: Plot of RM as a function of the projected distance along the axis with an angle of 59° from the East direction. The red line is the best straight line fit through the data. The box contains the parameters of the fit. The green line represents the position of the center that is taken from McLaughlin et al. (2006). The errors are at two sigma. For a detailed description of the plot see the text.

To measure a reasonable error on the angle, I calculated the reduced chi square for a large variety of values. I considered plausible the angles for which the reduced chi square was less than 2.4 (which corresponds to a probability of correlation higher than 0.5%). With this limit all angles between $50° - 70°$ resulted acceptable.

To check how much we can trust this correlation, I measured how likely a random distribution

of RMs for the pulsars in the cluster can generate a linear fit with a reduced chi square of 0.725.

To generate the random distribution I first scattered the position of the pulsars in the central region of the cluster and I gave to each pulsar a random RM taken between the minimum and maximum values of the observed set. To each pulsar I assigned the error that I measured from the real data. For each random distribution I used the same code as before to measure the direction with minimum reduced chi square (for a straight line fit) and I saved the resulting chi square value. Then I repeated the steps for 10000 different random distributions.

After I gathered all the results I measured the probability that the minimum reduced chi square was less than 0.725 (the value that I got form the real data). I obtained that the probability that a random distribution of RM produces a reduced chi square (for a straight line fit) of less than that is 0.17%. This means the observed data cannot be generated by a random distribution at 3 sigma.

This test proves that there is a very high probability that the pattern observed is real.

If I take this fit to be correct I can construct a model that allows me to determine the RM at each point of the cluster. This model is shown in fig. 6.8.

Now that we know that there is a gradient in the values of RM across the cluster we need to try to explain the origin of this gradient. It can be generated along the line of sight inside the Galaxy disk, in the Galactic halo or inside the globular cluster. Many different effects have to be considered for each of the cases as described in the following sections.

3   Galactic magnetic field

The Galactic magnetic field, despite having been studied for many years and with different techniques, is not very well known in its entirety. Direct studies have only been made in the local interstellar medium (LISM) by Voyager 2 with measured fields of $4 - 5\,\mu$G (Opher et al. 2009). For the rest of the galaxy we rely on the information carried by synchrotron emission, optical polarization, Zeeman splitting (Widrow 2002) and RM measures of pulsars and extragalactic sources (Han et al. 2006, Noutsos et al. 2008, Taylor et al. 2009). From these studies the resulting picture seems to be an azimuthal magnetic field directed in the plane of the disk inverting from clockwise to counter-clockwise going from spiral arms to the interarm regions. The halo field is even less known. A recent study (Mao et al. 2010) tried to measure the magnetic field in the regions of the Galactic poles and was not able to constrain any field in the north polar region but measured a field of $0.3\,\mu$G directed towards the south pole.

There are no models able to predict the value of the Galactic magnetic field and the contribution in RM in a certain direction in the sky. There are however some RM maps constructed by observing extragalactic sources (Taylor et al. 2009, Oppermann et al. 2012, 2015). Since these catalogues have been built mainly from NVSS sources, they contain very few sources at high negative latitudes (where 47 Tucanae is located). This means that the result obtained from these catalogues is very imprecise for the location I am interested in and doesn't have any angular information. According to the catalogue of Oppermann et al. (2015) the value of galactic RM is ~ 30 rad/m^2 with a scatter of ~ 8 rad/m^2 within $1°$. As I said, these values are to be considered only as a first approximate indication.

3.1   ISM turbulence

The small scale magnetic field is dominated by the turbulent motion of the gas. Many authors (Armstrong et al. 1995, You et al. 2007) found that the ISM density turbulence can be well described
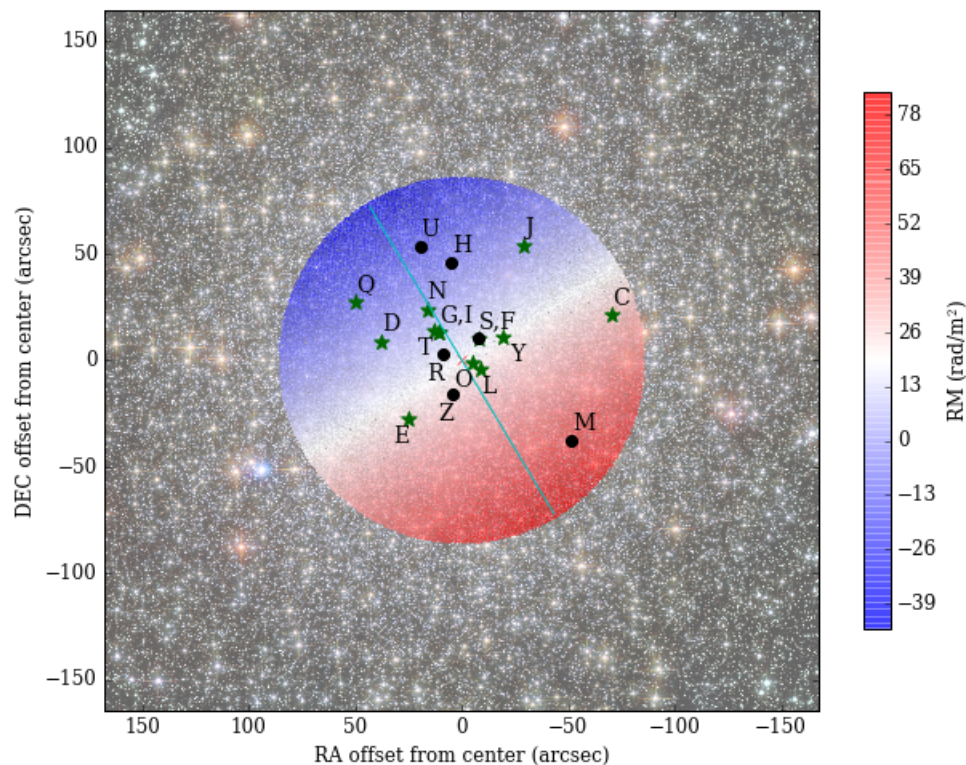
Figure 6.8: Model of globular cluster 47 Tucanae representing the values of RM in every point in the central region. The green stars and black dots are the pulsars with known position inside the cluster. The pulsars represented by green stars are those with measured RM, while for the ones represented by black dots no significant constrain on RM is available. The cyan line shows the direction of the measured gradient. The background image is the optical view of the cluster taken from the Hubble Space Telescope, credits: NASA, ESA, and the Hubble Heritage (STScI/AURA)-ESA/Hubble Collaboration.

by the Kolmogorov theory of turbulence (Kolmogorov 1941).

The Kolmogorov theory of turbulence (following the description of Somov (2006) and Chiuderi and Velli (2015)) assumes a stationary incompressible fluid and that the turbulence is homogeneous and isotropic. In this theory energy is injected in the fluid at the largest scale, the *outer scale*: at these dimensions viscosity is negligible. Through a non-linear cascade, energy is transferred to smaller scales creating eddies and turbulent motion. The energy continues to be transferred at smaller and smaller scales until it reaches the *dissipation scale* where viscosity becomes important and the fluid stops being turbulent and becomes laminar.

Starting from the Navier-Stokes equation it follows that the energy spectrum at different wave number, between the outer and the dissipation scale, becomes:

$$E(k) \propto \varepsilon^{2/3} k^{-5/3}, \tag{6.1}$$

where ε is the rate of energy input per unit mass (in the stationary solution it is independent from the scale) and k is the wave number. This is the famous *Kolmogorov spectrum.*

For the ISM, Armstrong et al. (1995) showed that the density fluctuations can be fitted with a Kolmogorov spectrum from 10^5 to 10^{13} m. In later works the spectrum was fitted at larger scales and estimates of the outer scale were found. Ohno and Shibata (1993) found values of ~ 100 pc and Haverkorn et al. (2008) confirmed this large value for the interarm regions while for the spiral arm found outer scales of > 10 pc. Similar values of $16 - 29$ pc where found by Iacobelli et al. (2013). Malkov et al. (2010) found, studying anisotropies in TeV cosmic rays, outer scales of ~ 1 pc.

These considerations are valid for the density fluctuation. Since usually the magnetic field is considered frozen to the matter, the fluctuations of both are thought to follow the same distribution. In a recent paper Xu and Zhang (2016) refute this line of reasoning. They propose, instead, that magnetic field fluctuations are still described by a Kolmogorov spectrum but are different from density fluctuations. They reconstructed the structure function of RMs and found that it is fitted by a broken power law steeper under the parsec scale. This can be explained if at large scales the electron density fluctuations dominate the RM while magnetic field fluctuations dominate on smaller scales. We found a variation of RM on very small scales that is inconsistent with the variation of density fluctuations (described by the DM). If if the observed variation is attributed to the ISM, our results support the Xu and Zhang (2016) hypothesis.

3.2 Contributions of the Galactic magnetic field

Inside the Galaxy there are different regions where the origin of the observed variations in RM could be located: the local interstellar matter (LISM); the spiral arms; the halo. Following the indications of different papers (Mao et al. 2010, Akahori et al. 2013) I check, in this section, the possible contributions of each region.

The maximum contribution of the LISM was estimated by Spangler (2009) to be $0.32 - 1.1$ rad/m^2. This estimate is measured for densities of 0.12 cm^{-3}, magnetic fields of 4 μG and volume filling factor (the fraction of the volume occupied by these clouds) of $5.5 - 19\%$. This means that the observed variation of $\sim 40 - 50$ rad/m^2 cannot be generated in this region.

In the spiral arms, the small scale field is dominated by turbulence. The Kolmogorov turbulence is homogeneous and isotropic and therefore if the line of sight intercepts a large number of bubbles, the resulting RM variations are supposed to be isotropic. I already proved that it is very unlikely for random variations of RMs to produce the observed trend, therefore turbulence probably isn't the cause for the gradient in the data. However, since we must consider also the case in which turbulence is not completely isotropic, I checked in the literature the amplitude of RM variations caused by turbulence. Mao et al. (2010) and Akahori et al. (2013) found that this value is $\sim 8 - 9$ rad/m^2 in the directions of the galactic poles. Another paper (Schnitzeler 2010) consolidated this result and derived a dependance on galactic latitude of $1/\sin(|b|)$. Calculating the resulting RM variation at the latitude of 47 Tucanae ($b \sim -45^\circ$) we obtain a value of ~ 12 rad/m^2. Similar results were also found by Johnston-Hollitt et al. (2004) who showed that the RM variation of extragalactic sources with galactic latitudes $|b| > 30^\circ$ is ~ 10 rad/m^2. This means that the turbulences are not strong enough to recreate the measured values of RM at these galactic latitudes.

These results are taken from large sky surveys and are therefore very general. To measure more precisely the Galactic contribution in the regions of the sky of 47 Tucanae we need to measure the RMs of extragalactic sources in the same region. Luckily our cluster of interest is located very close to the Small Magellanic Cloud (SMC) which has been subjected to a study of the magnetic field through RM measures and optical polarization (Mao et al. 2008). During this study the authors selected extragalactic radio sources in the area with measured RM and found a dependance of RM on the right ascension and fitted it with a straight line of equation:

$$\mathrm{RM}_{\mathrm{MiklyWay}} = (46.1 \pm 4.1) - (4.9 \pm 0.9) \times a \,\mathrm{rad/m}^2 \tag{6.2}$$

where a is the offset in degrees eastward from zero right ascension. They weren't able to test the dependance on the declination because of a lack of sources in the southern direction. Using this fit to measure the Galactic contribution at the position of 47 Tucanae returns $\sim 16 \pm 10$. This value is similar to what I find for the RM in the center of the cluster in fig. 6.7 but the variation over the angle is too small to explain what I see in the cluster.

To see if the gas in the spiral arms can explain the small scale ordered gradient observed we can envision an extreme case in which all the variations are caused by a single magnetized bubble. If we suppose that there is a constant magnetic field inside we can explain the measured trend by saying that the different lines of sight pass through different parts of the bubble. The lines of sight with higher RM pass near the center while those with lower RM pass near the side (as shown in fig. 6.9).
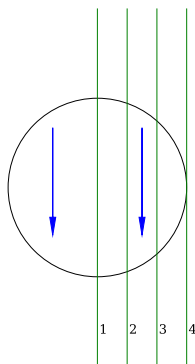
Figure 6.9: Model of the radiation of the pulsars passing through a magnetized bubble. The magnetic field in the bubble is constant and its direction is represented by the blue arrows, the green lines are the lines of sight for different pulsars. The lines of sight '1' and '2' cross the bubble for most of its part and the RM of the radiation becomes higher. Instead the line of sight '4' barely crosses the bubble and it is not influenced by its magnetic field.

To put the tightest constraints on the density and magnetic field I will set the dimensions of the bubble to be the largest possible so that the line of sight with highest RM passes through the center and the one with the smallest RM passes at the side. The distance between the two lines is $\sim 1'$, if we put the bubble at a scale height of 1 kpc from the galactic disk the distance on the line of sight becomes ~ 1.5 kpc (The cluster has galactic latitude of $b \sim -45°$), so the bubble should have

a radius of ~ 0.5 pc. We use the equation $RM \sim 0.81 n_e B_\parallel L$, where n_e is the electron dencity in cm^{-3}, $B_\parallel$ is the line of sight component of the magnetic field in μG and L is the distance travelled in the pulsar in pc. The total RM contribution of the bubble is ~ 45 rad/m^2 (the maximum RM difference of the sample), the total length crossed passing through the center is ~ 1 pc, so we obtain $n_e B_\parallel \sim 55$ μG/cm^3. Akahori et al. (2013) found that the turbulent magnetic field is of the order of ~ 2 μG, so the bubble should have an electron density of ~ 25 cm^{-3}. This value is not implausible for a dense cloud so, even though this is an extreme case, this could explain the observations.

Another possible region where the field could be generated is the halo. There are no precise models to explain the magnetic field in the Galactic halo. However, there are some hypotheses, like the Parker instability loop (Parker 1992) or a Galactic wind driven by cosmic rays (Haverkorn and Heesen 2012). These fields however would be weak, with very small variation on the parsec scales and, since the ISM density drops in the halo, very hard to detect. So the halo field cannot be responsabile for the observed variation.

In inspecting the direction of the observed gradient in galactic coordinates we find that it points towards the galactic disk and it is stronger on the side where the disk is located (see fig. 6.10).
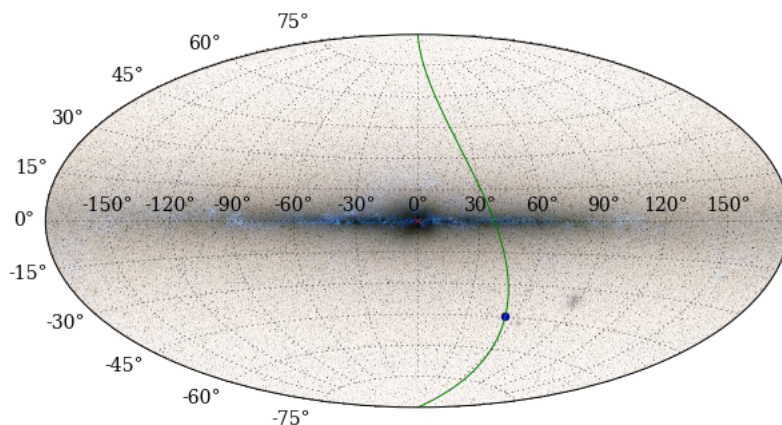
Figure 6.10: Plot of the Galaxy in galactic coordinates. The blue dot is the position of the globular cluster 47 Tucanae and the green line is the extrapolation over the whole sky of the direction of the gradient. The RM values are stronger on the side facing the galaxy disk. The background image is taken from the Two Micron All Sky Survey with inverted values.

If this is not considered to be a chance alignment it could be linked to an interaction between the Galactic wind and the globular cluster as described by the figure 6.11. In this picture the magnetic field flows outwards from the Galactic disk, when it reaches the cluster the field lines bend around it. The lines of sight of sources inside the cluster on the side facing the Galactic disk see a stronger parallel component of the magnetic field. Instead the line of sight of sources on the far side from the cluster see a negative component of the magnetic field. This scenario could explain the observed gradient in the data.
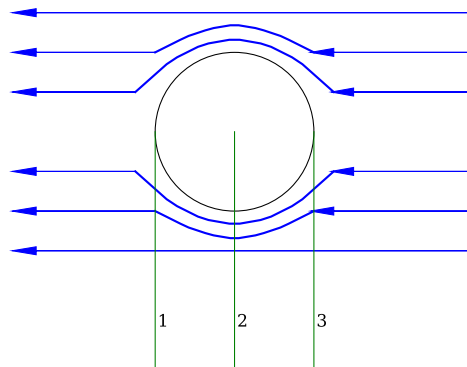
Figure 6.11: Representation of the interaction between a Galactic wind and the globular cluster. The blue arrows are the field lines while the green lines are the line of sight of the pulsars. As the cluster moves in the halo the magnetic field lines are bent around it. On the line of sight '1' the magnetic field has a negative component and the RM of the radiation becomes smaller. On the line of sight '2' there is no parallel component so the RM remains constant. Instead on the line of sight '3' the radiation sees a a stronger parallel magnetic field and acquires an higher RM.

4 Globular cluster magnetic field contribution

Another possibility to explain the data is to suggest that the magnetic field responsible for the observed variation is located inside the cluster. In the literature I couldn't find any example of a magnetic field linked to a globular cluster, but, since magnetic fields are ubiquitous is nature, it may be be possible that these objects contain one. Since we don't have any previous work to follow on this subject, the safest hypothesis is to assume that the magnetic field is frozen in the gas and that there is equipartition between the thermal and magnetic pressure. In plasma physics the ratio of the two pressures is expressed by the parameter β (Chiuderi and Velli 2015), defined as:

$$\beta = \frac{P_{th}}{B^2/8\pi} = \frac{2}{3}\frac{E_{th}}{E_{mag}}. \tag{6.3}$$

Equipartition is reached when $\beta \simeq 1$. To calculate the magnetic field corresponding to this value, I express the thermal energy as $E_{th} = 3/2nK_BT \times 4/3\pi r^3$, where n is the number density of the gas, K_B is the Boltzmann constant, T is the temperature and r is the radius of the cluster, and the magnetic energy as $E_{mag} = B^2/8\pi \times 4/3\pi r^3$. The terms representing the volumes cancel out leaving only:

$$1 = \frac{nK_BT}{B_{eq}^2/8\pi}, \tag{6.4}$$

isolating the magnetic field in the equation we obtain:

$$B_{eq} = \sqrt{8\pi n K_B T}. \tag{6.5}$$

The value of the electron density is $n_e = 0.067 \pm 0.015$ cm^{-3} (Freire et al. 2001b). We can assume to have the same density of protons, and the value of the gas temperature is $T \sim 2 \times 10^4$ K (McDonald and Zijlstra 2015). The equipartition value becomes $B_{eq} \sim 3\,\mu$G.

In a spherical symmetric system like a globular cluster, there are not many possible geometries a magnetic field can take: there is a constant field, a radial outflowing field or a turbulent field. None of these seem to explain the measured gradient. However in a previous chapter I reported that Bianchini et al. (2013) have measured a rotation of the stars in the cluster around an axis titled by $\sim 45°$ counterclockwise from the East direction. If also the gas to which the magnetic field is frozen is rotating around this axis, it is possible to describe the field with toroidal or poloidal geometries. The observed gradient is oriented almost orthogonally to the aforementioned rotational axis and the highest RMs are measured in the region where the motion of the gas is pointing towards us. Thus it might be possible to describe the field with a toroidal geometry.

4.1 Toroidal magnetic field

To test if a toroidal magnetic field could explain the data and to measure the strength and dimensions of such field, we first need to simulate the geometry and the effects of the field on the RMs. To solve this problem, I wrote a piece of code for the cases of a constant magnetic field and a field decreasing as $1/r$ (the code will be reported in the appendix).

The geometry and intensity of a magnetic field is usually described by the field lines. In the toroidal case, the field lines are circles centered around a given axis. Because of these considerations, in my code I generated evenly spaced circles around the axis perpendicular to the observed gradient and I assigned to each circle a magnetic field. The idea behind my code is that the radiation from each pulsar has to cross a number of circles forming with each one a different angle. Every field line crossed produces an additional RM which depends on the parallel component of the field, on the electron density and on the distance between field lines.

I created the model following different steps of increasing complexity, I will describe each step separately so that the explanation becomes easier to understand. At the first step I imagined all the pulsars aligned on the plane passing through the center perpendicular to the lines of sight (see fig. 6.12). For the pulsar near the edge the line of sight has to cross very few circles but the magnetic field of each line of force is directed towards (or opposite to) the line of sight. For the pulsars near the center the radiation crosses a large number of circles with field almost perpendicular to the line of sight. Another parameter that has to be considered is the distance between the circle along a line of sight, near the center it is very small, near the edge it is very large. This distance is the length for which a field line contributes to the total RM.

The model becomes more complicated if we consider that the pulsars are not on the plane passing through the center but are located farther or nearer from it. According to the model by Freire et al. (2001b) this distance can be calculated from the measure of DM. In this model the electron density in the region of the pulsar is constant at 0.067 ± 0.015 cm^{-3}. From equation 2.18 we find that the relation between DM and the distance crossed, L, is $DM = n_e L$. By measuring the difference in DM of the pulsar from the center, remembering that $DM_{center} = 24.38 \pm 0.09$ cm^{-3} pc (Freire et al. 2001b), we can obtain the distance from the plane passing through the center.

The lines of sight of the pulsars behind the center have to cross more field lines and accumulate a bigger RM (or smaller if the field is in the negative direction), instead radiation from the pulsars

(a) View from the top.   (b) View from the front.

Figure 6.12: Model of the toroidal magnetic field inside the cluster. In this case the pulsars are aligned along the East direction on the plane passing through the center perpendicular to the lines of sight. The axis of rotation of the field is along the North axis. The green lines are the lines of sight for different pulsars while the black circles are the magnetic field lines, the arrow indicate the direction the field. The blue dots are the pulsars. The z axis is the depth.

in front crosses less circles (see fig. 6.13).

Finally, the complete model measures the RMs from pulsars which are not aligned in the sky but are scattered across the cluster both in sky coordinates and in depth (see fig. 6.14). The measure of RM is more complicated if the pulsar is not located along the field lines that are projected on the center (as was the case for fig.6.12b and 6.13b). Since the symmetry is always along the rotational axis (the North axis in fig. 6.12-6.14), the field lines that pass in front of our line of sight are centered on the same axis. The parameters that change in this case are the maximum radius of the field lines in front of the pulsar and the number of those lines. Both decrease as we move to the poles. Thus also the RM contribution of the magnetic field becomes smaller for sources close to the poles.

Now the model is complete and we need to implement the different complications we saw. First we measure the tridimensional position of the pulsars in the cluster using the model of Freire et al. (2001b) to find the position along the line of sight. Then we set the total radius of the magnetized gas, the number of field lines and the rotational axis. Based on the 3d position of the pulsar we measure the distance along the rotational axis and the one perpendicular to it. The distance along the axis sets the total radius, R_{tot} and number of the field lines of interest, N_{tot}.

After this initial part, we measure the contribution of each field line in front of the pulsar to the RM. Supposing a constant toroidal field, B_0, each circle has a parallel magnetic field component of:

$$B_\parallel = B_0 \sin \theta = B_0 \frac{x}{r}, \qquad (6.6)$$

where θ is the angle between the line of sight and the field line, x is the perpendicular distance of the pulsar from the rotational axis and r is the radius of the field line in question. Inverting

(a) View from the top.   (b) View from the front.
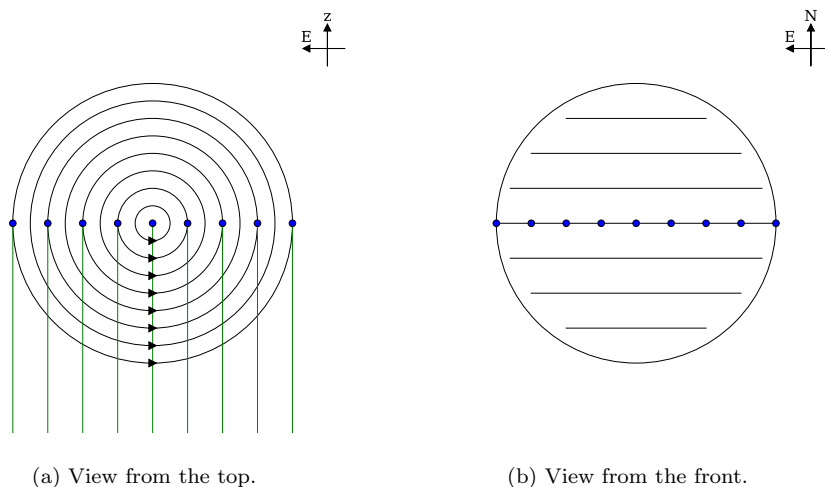
Figure 6.13: Model of the toroidal magnetic field inside the cluster. In this case the pulsars are aligned along the East direction but scattered along the z axis. The axis of rotation of the field is along the North axis. The green lines are the lines of sight for different pulsars while the black circles are the magnetic field lines, the arrow indicate the direction the field. The blue dots are the pulsars. The radiation from the pulsars farther from the center have to cross more field lines than the radiation from the pulsars in front.

equation 2.28 and using 2.18 in the case of constant density, we can write that $RM \simeq 0.81 n_e L B_{\parallel}$, where in this case L is the distance between two field lines along the line of sight. The distance in radius between two field lines (as they are evenly spaced) is R_{tot}/N_{tot} so we can express L as:

$$L = \sqrt{\left(r + \frac{R_{tot}}{N_{tot}}\right)^2 - x^2} - \sqrt{r^2 - x^2}. \tag{6.7}$$

I can conclude that the contribution of RM from a single field line is:

$$RM \simeq 0.81 \, n_e B_0 \frac{x}{r} \left(\sqrt{\left(r + \frac{R_{tot}}{N_{tot}}\right)^2 - x^2} - \sqrt{r^2 - x^2} \right) \tag{6.8}$$

$$RM \simeq 0.0543 \, B_0 \frac{x}{r} \left(\sqrt{\left(r + \frac{R_{tot}}{N_{tot}}\right)^2 - x^2} - \sqrt{r^2 - x^2} \right), \tag{6.9}$$

where I used $n_e \simeq 0.067$ (Freire et al. 2001b).

I performed a fit using this equation to find the best value of magnetic field that explains the observed gradient. The fit had two parameters, one is $0.0543 \, B_0$ and the other is the galactic RM (added as a constant over all the cluster). I chose to take the number of field line to be 1000 and the radius of the region immersed in the magnetized gas to be 8 pc. This value is large enough to
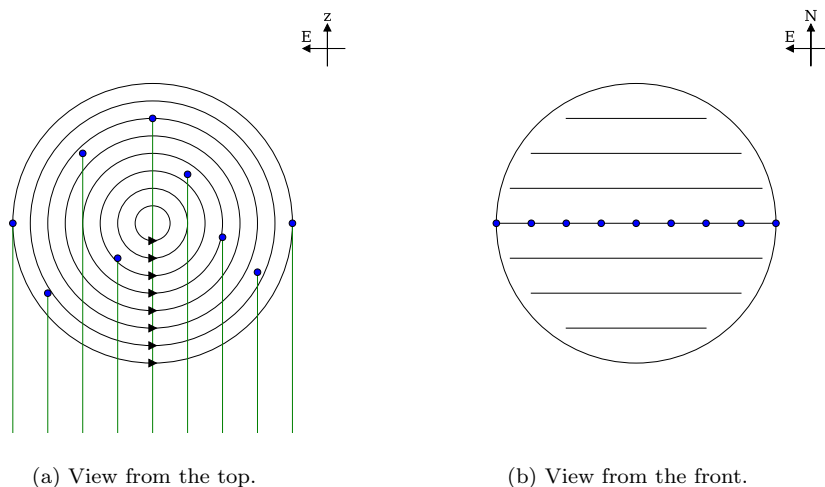
(a) View from the top.   (b) View from the front.
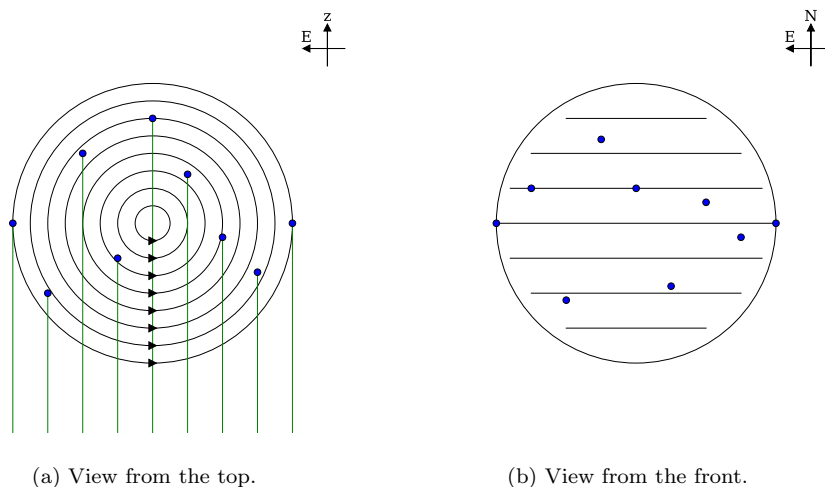
Figure 6.14: Model of the toroidal magnetic field inside the cluster. In this case the pulsars are scattered along the North, East and z axis. The axis of rotation of the field is along the North axis. The green lines are the lines of sight for different pulsars while the black circles are the magnetic field lines, the arrow indicate the direction the field. The blue dots are the pulsars. The maximum radius of the field lines diminishes as we approach the poles. Together with it also the number of field lines in front and the total contribution of RM decreases.

contain all the pulsars but not much larger. Since I don't have any mean of exploring the region outside this sphere I cannot exclude that the magnetic field permeates to a larger radius. But I found from the fit that the intensity of the magnetic field required does not change much modifying this radius. Therefore for this parameter I chose the value that requires less energy (the smallest possible radius).

The axis of rotation was found with a code (similar to the one used to find the best direction of the gradient), that calculated the chi squares of the fit described above for different angles and chose the axis that minimized the chi square.

The best axis has an angle of 59° measured clockwise from the East direction and has a reduced chi square of 0.723 with 11 degrees of freedom (the probability of correlation is $\sim 70\%$). The best fit along this is plotted versus the differences of DM in fig. 6.15 and versus the position in fig. 6.16. The best value of the magnetic field is $(192 \pm 13)\,\mu G$ and the value of RM induced by the galaxy is $(18 \pm 1)\ \mathrm{rad/m^2}$. This fit follows the data very well and passes through all the data within two sigma uncertainty.

Real life toroidal fields usually do not have constant strength at all radii, but rather decrease with increasing radius. I used the same code to see if an a toroidal field decreasing as $1/r$ can explain the data. The code works in the same way except that in the relation 6.9 there is an extra factor $1/r$. The contribution from every field line to the total RM therefore becomes:

$$RM \simeq 0.0543\, B_0 \frac{x}{r^2} \left(\sqrt{\left(r + \frac{R_{tot}}{N_{tot}} \right)^2 - x^2} - \sqrt{r^2 - x^2} \right). \qquad (6.10)$$

Figure 6.15: Plot of RM as a function of the differences of DM from the center value taken from Freire et al. (2001b) (green line in the plot). The red crosses are the values predicted by the best fitted model. The box contains the parameters of the fit. The errors are at two sigma.

Figure 6.16: Plot of RM as a function of the distance among each pulsar and the perpendicular to the selected axis passing across the center of 47 Tucanae. The red crosses are the values predicted by the best fitted model. The box contains the parameters of the fit. The green line represents the position of the center that is taken from McLaughlin et al. (2006). The errors are at two sigma.

In this case B_0 becomes the intensity of the magnetic field at a distance at 1 pc from the center (all distances are in units of parsecs).

The best axis has an angle of 59.3° measured clockwise from the East direction and has a reduced chi square of 2.01 with 11 degrees of freedom (the probability of correlation is ~ 2%). The best fit is plotted against the differences in DM in fig. 6.17 and against the position projected on the axis of rotation in fig. 6.18. The best value of the magnetic field at 1 pc is $(236 \pm 28)\,\mu G$ and the value of RM induced by the galaxy is (14 ± 2) rad/m^2. This fit is not as good as the previous one but still passes through almost all data within two sigma uncertainty.
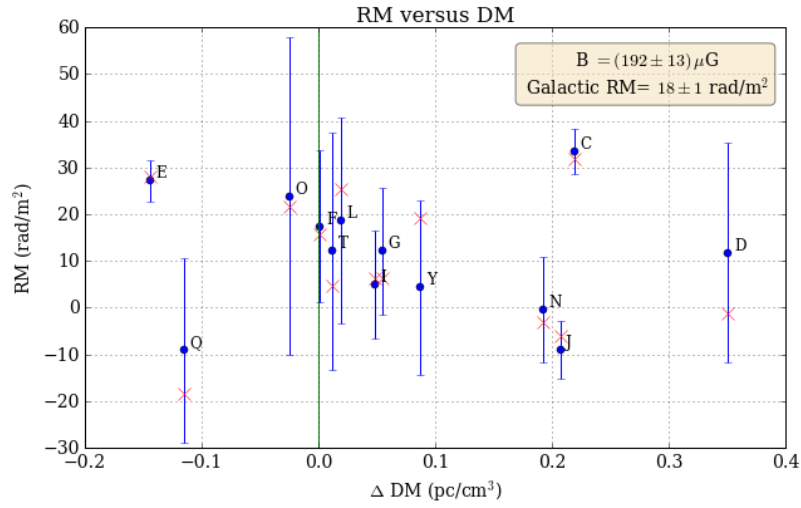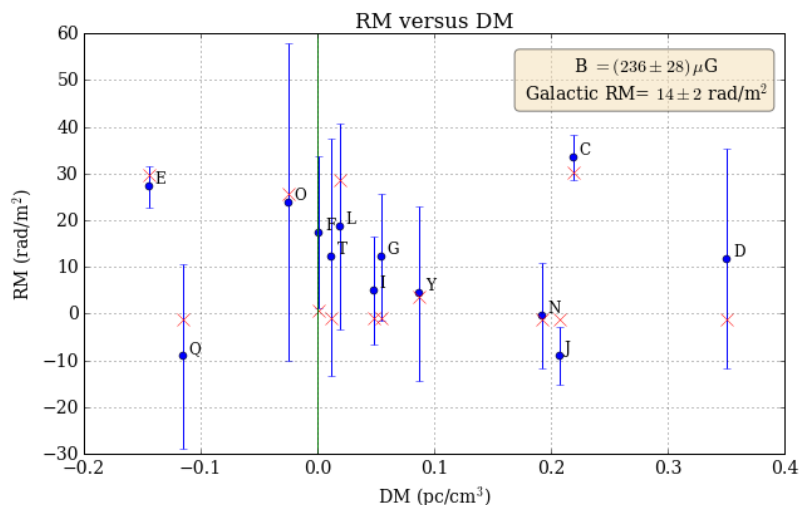

Figure 6.17: Plot of RM as a function of the differences of DM from the center value taken from Freire et al. (2001b) (green line in the plot). The red crosses are the values predicted by the best fitted model. The box contains the parameters of the fit. The errors are at two sigma.

The constant strength toroidal magnetic field fits the data better than the field decreasing as $1/r$. In both cases there is a magnetic field of ~ $200\,\mu G$ inside the cluster. This value is 2 orders of magnitude greater than the equipartition value measured before. In this case the β parameter would be ~ 10^{-4}. This means that the magnetic field is the dominant form of energy in this region. Usually, when this happens in nature, different processes that dissipate this energy in heat start to take place (like in the Solar corona). However we know that the cluster is cleared of all ionized gas in very short times, 10^6 yr according to McDonald and Zijlstra (2015), and it can be possible that these processes don't have time to take place.

It might be possible that this unusually high magnetic field is contained only in the small region of space occupied by the pulsars while outside it drops to normal levels. This might be impossible to test directly even with the next generation of radio telescopes as we don't have sources in those regions that we could use as probes. A possible solution may come from theoretical works such as complex magnetohydrodynamical simulations.
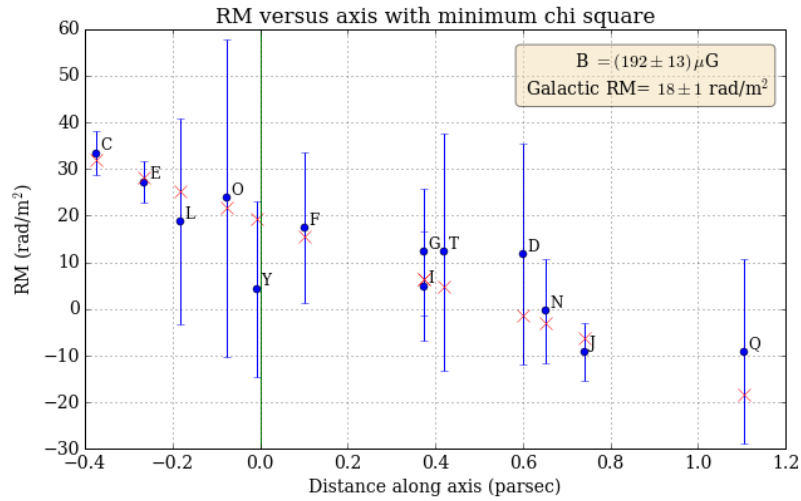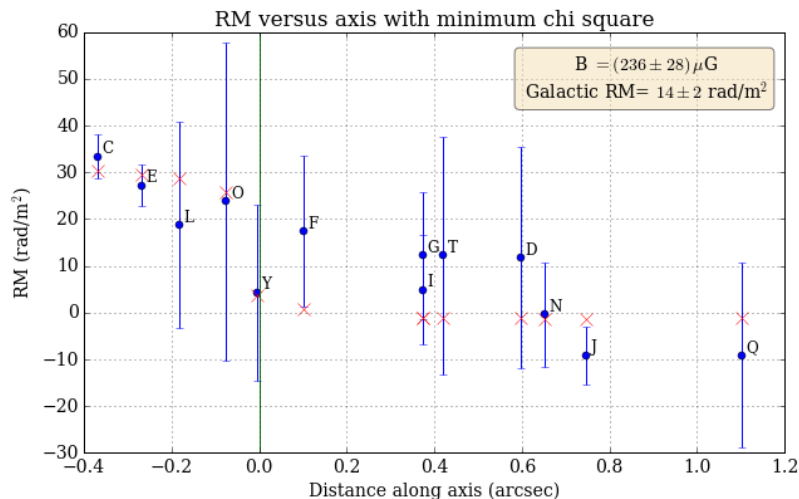
Figure 6.18: Plot of RM as a function of the projected distance among each pulsar and the perpendicular to the selected axis passing across the center of 47 Tucanae. The red crosses are the values predicted by the best fitted model. The box contains the parameters of the fit. The green line represents the position of the center that is taken from McLaughlin et al. (2006). The errors are at two sigma.

4.2 Possible origin of the magnetic field

If there is a relatively strong magnetic field in the central region of the cluster, it might be interesting to study how it is generated. Many theoretical works have been written on the subject of the generation of cosmic magnetic fields (Moss and Shukurov 1996, Widrow 2002, Beck 2016). Following the literature I will examine the different processes and see if they are applicable in my case:

Primordial field

The internal magnetic field could be present from the formation of the cluster. It could be a residual of the Galactic magnetic field or could have have been generated in the early stages of its life. However, the ionized gas is expelled on timescales of $\sim 10^6$ yr (McDonald and Zijlstra 2015). If the field is frozen to this gas any primordial field would escape on the same timescales. Therefore the primordial field would be completely gone and what we see must be constantly generated.

RGB and pulsar winds

The first thing to check is if the magnetic field can be generated by local sources in the cluster. Most of the gas inside 47 Tucanae was expelled from evolved stars like RGBs or AGBs. These stars are the most massive in the cluster and are therefore most easily found near the center of the cluster. In a theoretical work, Suzuki (2007) showed that the winds of RGB stars can form hot magnetized bubbles. The magnetic field on the surface of the star that generates these bubbles has an intensity of ~ 240 G. The radii of these stars is taken to be $\sim 20 R_\odot$ (~ 0.1 AU), even though

it may vary depending on the model. If we assume conservation of magnetic flux across the entire heliosphere, taken to be ~ 100 AU large, we obtain that the magnetic field at the border is:

$$B_{sur} R_{sur}^2 \simeq (B\, R^2)_{100\, AU} \tag{6.11}$$

$$B_{100\, AU} \simeq B_{sur} \left(\frac{0.1\, AU}{100\, AU} \right)^2 \tag{6.12}$$

$$B_{100\, AU} \simeq 240\, \mu G. \tag{6.13}$$

If we suppose that the central region is filled with cells of this size and magnetic field and that the magnetic field inside each cell is constant but it is uncorrelated between different cells, we would have a field of rms intensity of (Widrow 2002):

$$B_{rms} = \simeq B_{100} \left(\frac{R_{cell}}{L} \right), \tag{6.14}$$

where L is the dimension of central region of the cluster, $L \sim 10 pc$. We obtain $B_{rms} \simeq 0.1\, \mu G$. This field is too small to be responsible for the observed one.

Other possible sources for the magnetic field are the many pulsars that populate this cluster. An estimate of ~ 200 millisecond pulsars are thought to be hosted in 47 Tucanae (Camilo et al. 2000). Each of these pulsars has a surface magnetic field of $\sim 10^8 - 10^9$ G and a surface radius of $\sim 10^6$ cm. If I repeat the same argument as before in this case, assuming cells of ~ 100 AU and flux conservation we obtain:

$$B_{100\, AU} \simeq 10^8\, g \left(\frac{10^6\, \text{cm}}{10^{15}\, \text{cm}} \right)^2 \tag{6.15}$$

$$B_{100\, AU} \simeq 10^{-4}\, \mu G \tag{6.16}$$

Such fields are negligible if confronted with the ones from RGB stars. However, many millisecond pulsars are in binary systems and the interaction between the pulsar wind and the companion can create shocks that enhance the magnetic field.

Dynamos

The weak fields that seem to be present in the cluster are not strong enough to recreate the hypothetical toroidal magnetic field, but could be used as seed fields by dynamo mechanisms. These processes can amplify randomly organized seed fields into large scale structures and are known to be common in astrophysical environments. Indeed, large scale magnetic fields in galaxies and in galaxy clusters can only be explained considering a dynamo that amplifies and aligns very weak seed magnetic fields. The most common types of dynamos are the $\alpha - \Omega$ dynamo (Beck et al. 1996, Widrow 2002, Beck 2016) and the turbulent dynamo (Moss and Shukurov 1996).

Not all processes can work in our case as there are some constraints: the globular cluster 47 Tucanae is almost spherically symmetric, with small hints of a rotation; the gas to which the magnetic field should be tied is constantly escaping the cluster at high speeds, the time scale of escape is $\sim 4 \times 10^6$ yr (McDonald and Zijlstra 2015).

The $\alpha - \Omega$ dynamo is based on differential rotation (Ω) and on expanding gas flows whose magnetic field is twisted by the Coriolis force (the α effect). This mechanism can generate toroidal fields but cannot be applied to the cluster as there is no differential rotation.

The turbulent dynamo does not require differential rotation but it does require a turbulent motion of the gas. To check if the gas in the cluster is turbulent I return to the Kolmogorov theory and check whether it can be applied in this case. From the theory we can express the dissipation length scale as:

$$l_d = \left(\frac{\nu^3}{\varepsilon}\right)^{1/4},\tag{6.17}$$

where ν is the kinematic viscosity of ionized hydrogen and is $\sim 10^{21} \text{cm}^2\text{s}^{-1} \left(\frac{\text{T}}{2\times 10^4 \text{K}}\right)^{5/2} \left(\frac{\text{n}}{0.067\text{cm}^{-3}}\right)^{-1}$ (Ryden 2016), and ε is the rate of energy input per unit mass. We express ε as the energy emitted by the stars in the cluster 10^{47} eV/s (McDonald and Zijlstra 2015) divided by the total mass of the gas, $11 M_\odot$ (McDonald and Zijlstra 2015). Converting the units in cgs we obtain $\varepsilon \sim 20$ erg/s/g. The dissipation length scale becomes:

$$l_d \sim 2.65^{15}\,\text{cm} \sim 130 \text{AU}\tag{6.18}$$

This means that for scales smaller than this the flow becomes laminar. Since the energy injection sources are the stars, the energy injection scale , or outer turbulence scale, is ~ 100 AU. We can conclude that the gas in the cluster is likely not turbulent. Therefore the turbulent dynamo cannot work in 47 Tucanae.

Therefore the processes usually considered to be responsible for the generation of cosmic magnetic fields are not easy to apply in our case. The amplification of the field could be linked to cosmic rays or to external influences from the Galactic magnetic field.

Intermediate Massive Black Hole (IMBH)

If there is an IMBH in the center of the cluster, then it could be responsible for the observed toroidal field. In the accretion disk of the black hole many different processes can occur to amplify a seed field in the same way it happens around AGNs (Hoyle 1969). This association could explain also the axis of rotation of the magnetic field. The rotation velocity of stars is too small (smaller than the isotropic component) to explain such a strong correlation between the rotational axis of the stars and of the magnetic field. If on the other hand there is a rotating black hole in the center, it is likely to be aligned with the rotation of the stars and could generate a toroidal field with the same axis.

4.3   Radiative effects of the magnetic field

The intensity of the internal magnetic field necessary to explain the observed variation of the RMs is so high that it might be interesting to check is this field can be revealed by other mechanisms. The most used observational tracers of magnetic field are (Widrow 2002): Zeeman splitting, optical polarization and synchrotron radiation.

Zeeman splitting refers to the splitting between electronic energy levels in strong magnetic fields. To measure the intensity of the field we need to measure the difference between the atomic

or molecular energy levels. Unfortunately there is no detected neutral gas in the cluster, so we cannot use this method.

The optical polarization mechanism is caused by the alignment of prolate magnetized dust particles along the field lines. These particles absorb part of the starlight revealing the orientation and strength of the field. Unfortunately, also in this case there is no evidence of dust in the cluster so this method cannot give us any informations.

Synchrotron radiation

Synchrotron radiation is emitted by relativistic electrons orbiting around the field lines. To check if this could reveal the magnetic field deduced before, we need to check whether there are enough relativistic electrons in the central region of the cluster.

In the disk of the Galaxy there is a large population of relativistic electrons in the Galactic cosmic rays (Longair 2011), however most of them have low energy and are trapped in the disk by the Galactic magnetic field. Due to the magnetic turbulence, some electrons can escape the disk and reach the halo. The cosmic rays scale height is $\sim 2 - 3$ kpc (Haverkorn and Heesen 2012). Since the cluster 47 Tucanae is located at a height of ~ 3 kpc from the disk, we don't expect a large number of relativistic electrons.

Even if there are not many electrons coming from the outside, they can be generated from internal sources like the millisecond pulsars. Pulsars are known to be sources of relativistic particles (Kirk et al. 2009), but millisecond pulsars were thought to be devoid of them because of their low magnetic field (Harding et al. 2005). However recent observations proved that relativistic pairs are produced in the magnetosphere of millisecond pulsars (Venter et al. 2015). Harding and Muslimov (2011) found that millisecond pulsars can produce pairs with energies up to ~ 1 TeV and that about 1% of the spin-down luminosity is converted in electron-positron pairs. The spectrum is usually taken to have a spectral index of -2 (Venter et al. 2015).

Therefore it is safe to assume that inside the cluster we have electrons of energy up to ~ 1 TeV. First we check if these particles are trapped by the magnetic field in the cluster or if they will freely escape. This is usually done by confronting the gyration radius with the physical dimension of the object (Longair 2011). The gyration radius of electrons in a magnetic field can be expressed as:

$$r_g = \frac{\gamma m_e c^2 \beta}{eB} \simeq 1.7 \times 10^3 \frac{\gamma}{B} \, [\text{cm}], \tag{6.19}$$

where γ is the Lorentz factor of the particle, m_e is mass of the electron, c is the speed of light, β is the ratio between the velocity of the particle and the speed of light, e is the elementary charge and B is the magnetic field. To solve the equation I used the simplification $\beta \simeq 1$. Inserting the measured value of the magnetic field $B \sim 200 \, \mu$G, we obtain:

$$r_g \simeq 8.5 \times 10^6 \gamma \, [\text{cm}] \simeq 2.8 \times 10^{-12} \gamma \, [\text{pc}]. \tag{6.20}$$

According to our model the globular cluster has a strong magnetic field only in the central region of radius $r_{GC} \sim 8$ pc. This means that all electrons with $\gamma < r_{GC}/r_g \sim 3 \times 10^{12}$ are trapped in this region. Converting this value in energy we obtain $E \sim 10^{18}$ eV. We can safely assume that all electrons generated by the pulsars are trapped in this region. However, we must consider that if the energetic particles follow the field lines which are linked to the gas, they are carried out of the cluster in a time scale of $\sim 10^6$ yr.

Next, we need to estimate how many of these electrons emit synchrotron radiation. The most energetic particles lose their energy through radiation in very short time. Ghisellini (2013) gives a simple formula to calculate the time in which a particle of Lorentz factor γ loses its energy due to synchrotron radiation:

$$t_{syn} = \frac{24.57}{B^2\gamma} \text{ yr.} \tag{6.21}$$

Inverting this formula we can find the energy of the electrons that lose all their energy in $\sim 10^6$ yr under the given magnetic field, we obtain:

$$\gamma \sim \frac{24.57}{10^6}\frac{1}{B^2} \sim 600, \tag{6.22}$$

which corresponds to an energy of $E \sim 550$ MeV. I make the assumption that only electrons of higher energies emit radiation.

To find the total energy emitted by these electrons I consider the spin down luminosity of all pulsars. Typically, for a millisecond pulsar, we have $L_{sd} \sim 10^{34}$ erg/s. In the cluster there is an estimate of ~ 200 pulsars (Camilo et al. 2000), so the total luminosity emitted by all pulsars is $L_{sd,tot} \sim 2 \times 10^{36}$ erg/s. Of this energy only 1% is converted into pairs. We conclude that the energy per unit time present in pairs is $L_{pair} \sim 2 \times 10^{34}$ erg/s.

Of this energy only the one contained in electrons more energetic than ~ 550 MeV is emitted in synchrotron. To estimate the total luminosity in synchrotron we make use of the spectral distribution of electrons. The distribution is peaked at 1 MeV (the energy of the rest mass of the electron) and decreases to higher energies with a spectral index of -2. If we suppose that the luminosity at the peak is L_{pair}, the luminosity at 550 MeV (which is the total luminosity emitted by synchrotron) can be estimated as:

$$L_{syn} \sim \frac{L_{pair}}{550^2} \sim 6 \times 10^{28} \text{ erg/s.} \tag{6.23}$$

The bolometric flux emitted is $F_{syn} = L_{syn}/(4\pi R^2)$, where R is the distance of the cluster. Setting the distance to 4500 pc (Harris 2010), we obtain $F_{syn} \sim 3 \times 10^{-17}$ erg/s/cm^2.

The range of frequencies at which this energy is emitted can be found using the formula (Ghisellini 2013):

$$\nu_s = \gamma^2 \frac{eB}{2\pi m_e c} \sim 3 \times 10^5 \gamma^2 \text{ Hz.} \tag{6.24}$$

For the γs of interest, between 600 and 10^6 (corresponding to an energy of 1 TeV), we obtain frequencies between $(10^{11} - 3 \times 10^{17})$ Hz. In this range the spectrum is a power law peaked at 10^{11} Hz and with spectral index $-\alpha = (p-1)/2$, where $p = 2$ is the opposite of the spectral index of the electrons. The spectral index of the observed flux is -0.5. The value of the peak can be observed with the HFI instrument on board of the Planck satellite (the lowest frequency band of this instrument is between 87-117 GHz) (Lamarre et al. 2003). To see if this instrument would be capable of observing the synchrotron radiation we need to measure the flux in that frequency band.

The monochromatic flux can be described by the formula $F(\nu)d\nu = k\nu^{-0.5}d\nu$, where k is a constant. Integrating this across the spectrum gives us F_{syn}, so we can find the value of the constant k:

$$F_{syn} = \int_{10^{11}}^{3\times10^{17}} k\nu^{-0.5}d\nu = 2k\left[\nu^{0.5}\right]_{10^{11}}^{3\times10^{17}} \simeq 10^{9}k \tag{6.25}$$

$$k \simeq \frac{F_{syn}}{10^{9}} \simeq 3\times10^{-26} \, \text{erg/s/cm}^{2}/\text{Hz}^{0.5} \tag{6.26}$$

The monochromatic flux at the peak becomes:

$$F(\nu_{peak}) \simeq 3\times10^{-26}(10^{11})^{-0.5} \simeq 10^{-31} \, \text{erg/s/cm}^{2}/\text{Hz}. \tag{6.27}$$

The sensibility of the Planck instrument expressed in brightness temperature is $\sim 10^{-6}$ K. To convert the estimated flux in brightness temperature we must first convert it into intensity and then use the formula (Ghisellini 2013):

$$T_{B} = \frac{c^{2}I(\nu)}{2k_{B}\nu^{2}} \tag{6.28}$$

The intensity can be found dividing the flux by the solid angle of the source (the central region has a radius of 6 arcminutes), we finally obtain:

$$T_{B} = \frac{c^{2}F(\nu)}{2k_{B}\nu^{2}\pi\theta^{2}} \sim 3\times10^{-12} \, \text{K}, \tag{6.29}$$

Thus the synchrotron radiation emitted by the relativistic electrons in this magnetic field would not be visible by the HFI instrument on board of the Planck satellite.

The magnetic field would therefore have no observable radiative counterparts and only more precise measures of the Faraday rotation could give us insight on the nature of the field.

Chapter 7

Conclusions and Prospects

The aim of my work was to test the presence of a magnetic field linked to a globular cluster by measuring the amount of Faraday rotation of the pulsars in 47 Tucanae. At the same time it was possible to probe the turbulent nature of the ISM on very small scales of the order of arcseconds.

The raw observations, taken at the Parkes radio telescope, were corrected for the artificial interference, calibrated and reduced to a more compact size. The rotation measure (RM) of the pulsars were then derived with a code written in Python and the errors were estimated with a Monte Carlo simulation.

The results showed a large scatter in the amount of Faraday rotation among the sample of pulsars, and a thorough analysis was carried out to find the origin of this scatter. The data was found to follow a gradient, the best model that fits the data being shown in fig. 6.8. The gradient can be thought to be generated in the Galaxy along the line of sight or inside the cluster. Both hypotheses were tested.

In the case of a Galactic origin, the investigated possibilities were: a turbulent magnetic field and a localized magnetic field. The strong anisotropy of the scatter seems discarding the possibility of it being generated by an isotropic turbulent field in the Galaxy. On the contrary, a localized source could better explain the gradient. The required electron number density and magnetic field are not too extreme for the Galactic context.

The gradient was seen to point in the direction of the Galactic disk. This led to the idea that it could be generated by an interaction between a Galactic outflow and the cluster itself. In this scenario, the magnetic field lines of the outflow would bend around the cluster and would point towards our line of sight in the side near the Galactic disk and away from the line of sight far from the disk.

The case in which the gradient is generated in the cluster has also been considered. It was not possible to fit the data with a constant magnetic field inside 47 Tucanae, but, instead, the data were compatible with a toroidal field. Indeed, there is optical evidence for a collective rotation of the stars in the cluster around an axis almost perpendicular to the observed gradient (Bianchini et al. 2013). To explain the intensity of the gradient, the toroidal field would need to have intensities of $\sim 200\,\mu$G. This value is almost two orders of magnitude greater than the equipartition value with the gas. The possible sources of this magnetic field were searched following various theoretical works. It was found that the field could not be explained by the magnetized outflow of ordinary stars and/or pulsars, but needed amplification. The most common types of dynamos were discarded

as the source of the amplification. A possibility that could not be excluded (nor confirmed), was the presence of an intermediate mass black hole (IMBH) in the center of the cluster as the origin of the magnetic field. The radiative signature of the implied field was found to be too weak to be observed by the present day radio telescopes in the form of synchrotron radio emission.

It was not possible to conclusively determine the origin of the observed gradient. However, the presence of a constant magnetic field inside the cluster was rejected. Furthermore, the presence of an isotropic turbulence in the ISM was not confirmed. Probably, the effects of the isotropic turbulence on these scales are weak and have not been detected during the observations. Even if this work did not firmly prove the existence of a magnetic field inside a globular cluster, it showed that such fields may be within our observational capabilities.

1   Future prospects

Further theoretical works, focused on the magnetic fields in globular clusters, could help discern between the possible origins of the observed gradient. Magnetohydrodynamical (MHD) simulations, already suggested by Naiman et al. (2013), could be of significant importance. These simulations could show whether toroidal fields could reach the intensities required to explain the results and also reveal the origin of such fields.

A large improvement in the quality of the data could come with the next generation of radio telescopes in the southern hemisphere, like the Square Kilometre Array (SKA)[1] or its precursor in South Africa, MeerKAT. When completed, the SKA will be the largest radio telescope in the world with a total collecting area of one square kilometer (for comparison the Parkes radio telescope has a collecting area of ~ 3200 square meters). It will be made up of thousands of radio telescopes and will be built in Australia and in South Africa. It will not be fully completed before the 2030s. However, as soon as 2023, SKA1-MID, a smaller version of the radio telescope, will be fully functional. It will have a collecting area of ~ 33000 square meters.

MeerKAT (Booth and Jonas 2012) is an array in the Karoo desert in South Africa that consists of 64 Gregorian offset antennas with a projected diameter of 13.5 meters. It will be commissioned in 2017 and will form the central nucleus of SKA1-MID. The first 16 antennas have already been built and will start soon to observe the sky. Once completed it will have a collecting area of ~ 9000 square meters.

The improvement of the quality of the data with these telescopes can be estimated by studying the improvement of the Signal to Noise Ratio (SNR) of the polarization profiles of the pulsars. The SNR grows linearly with the effective area and as the square root of the integration time. Therefore, observing the same pulsars with MeerKAT with the same integration time will increase the SNR by a factor of ~ 3. The SNR will later increase by a factor of ~ 10 when using SKA1-MID with the same integration times.

The increase of SNR leads to an increase in sensibility and to a decrease of the minimum detectable intrinsic magnetic field in a globular cluster. As an example, to test the capabilities of the different telescopes we assume that there is a constant magnetic field in the cluster. In this case there is a correlation between the rotation measures (RMs) and the dispersion measures (DMs) of the pulsars. The minimum detectable magnetic field can then be estimated by setting the variations in RM across the various values of DMs to be larger than the errors on the values of RM at two

---

[1] for more informations see https://www.skatelescope.org

sigma. To estimate the errors of RM for different SNR, I modified the previously used Monte Carlo simulations to calculate the errors of RM for my sample. The results are shown in fig. 7.1.

By inspecting this plot, we can quantify the improvement gained by using a larger telescope. At a fixed integration time, MeerKAT will be able to measure an intrinsic magnetic field which is ~ 3 times less intense than that measurable with the Parkes radio telescope. To obtain the same sensibility as MeerKAT with the Parkes radio telescope, the integration time needs to increase by a factor of ~ 10. Also, the capabilities achieved by SKA1-MID will be ~ 10 times that of Parkes observing for the same amount of time. To obtain the same sensibility with Parkes we would need an integration time longer by a factor of ~ 100.
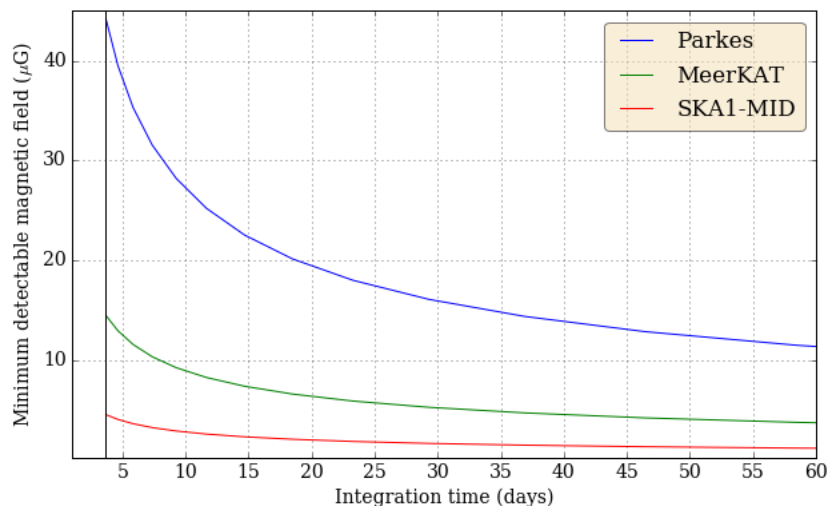
Figure 7.1: Plot showing the minimum intensity of a supposedly constant magnetic field in the cluster 47 Tucanae, as detectable by the different telescopes. The x-axis reports the integration time expressed in days. The black vertical line represents the total integration time of the observations used in this work. The magnetic field measurable with the MeerKAT radio telescope with the same integration time is ~ 3 times fainter than what achievable with the Parkes radio telescope. The details of how this plot was created are in the text.

With MeerKAT, and, in the future, SKA1-MID, we could observe the pulsars in 47 Tucanae with unprecedented details. We could obtain more precise measures of the Faraday rotation for the pulsars observed in this work and, possibly, obtain a first measure for the ones that showed weak polarization. This could give us more informations on the nature of the magnetic field responsible for the reported values of the RMs. Possibly, this could lead to a decisive proof of the existence of (or lack of) a magnetic field inside the globular cluster 47 Tucanae.

Appendix A

RM code

Here I present the code used to calculate the Faraday rotation measure of the pulsars. The code is written in the Python programming language. It follows the prescriptions described in Tiburzi et al. (2013).

In the first part I load the profile scrunched to 4 frequency channels and I set the start and end of the profile and of the off-pulse region. The profile has already been corrected for the RM value found with the program *rmfit*.

```
namefile= '/Volumes/Pulsar/47tuc/C/47tucCfinalbdf4rm.txt'

profile=(np.genfromtxt(namefile, skip_header=1, delimiter=' '))[:,:]

nfreq=int(profile[-1,1])+1
nbin=int(profile[-1,2])+1

I=np.zeros(shape=(nfreq,nbin))
Q=np.zeros(shape=(nfreq,nbin))
U=np.zeros(shape=(nfreq,nbin))
V=np.zeros(shape=(nfreq,nbin))

for n in xrange(0,nfreq):
    for j in xrange(0,nbin):
        if  profile[n*nbin+j,1]==n:
            I[n,j]=profile[n*nbin+j,3]
            Q[n,j]=profile[n*nbin+j,4]
            U[n,j]=profile[n*nbin+j,5]
            V[n,j]=profile[n*nbin+j,6]

freq=np.zeros(nfreq)
for i in xrange(0,nfreq):
    freq[i]=1382 + 312.5/(nfreq) *(i-2) + 312.5/(2*nfreq)

inizio=int(0.2*nbin)
fine=int(0.38*nbin)
startoff=int(0.5*nbin)
```

```
endoff=int(1.0*nbin)
```

In the next part I calculate the values of the position angle for the different frequencies using the formula 5.3. The Python function atan2() returns the correct angles between $-\pi$ and π.

```
Qpulse=np.zeros(shape=(nfreq,fine-inizio))
Qpulse=Q[:,inizio:fine]

Upulse=np.zeros(shape=(nfreq,fine-inizio))
Upulse=U[:,inizio:fine]

PA=np.zeros(nfreq)

for i in xrange(0,nfreq):
    if sum(Qpulse[i])==0.:
        PA[i]=0
    else:
        PA[i]= 0.5* math.atan2(sum(Upulse[i,:]), sum(Qpulse[i,:]))
```

Then I calculated the error on the measures of PA. First I measured the value of the noise calculating the root mean square of the total intensity in the off-pulse region. Then I measured the amount of linear polarization. This amount is biased to positive values, so I had to correct it following Wardle and Kroneberg (1974).

The measure of the error of PA for high SNRs follows Everett and Weisberg (2001). For low values of SNR, I separately constructed an analytical function to measure the error following Naghizadeh-Khouei and Clarke (1993).

```
Ioffpulse=np.zeros(shape=(nfreq,endoff-startoff))

for j in xrange(0,nfreq):
    for i in xrange(startoff,endoff):
        Ioffpulse[j,i-startoff]=I[j,i]

Ipulse=np.zeros(shape=(nfreq,fine-inizio))
Ipulse=I[:,inizio:fine]

rmsoffpulse=np.zeros(nfreq)
for i in xrange(0,nfreq):
    rmsoffpulse[i]=np.std(Ioffpulse[i,:])

L=np.zeros(nfreq)
for i in xrange(0,nfreq):
    L[i]=np.sqrt((sum(Upulse[i,:]))**2 + (sum(Qpulse[i,:]))**2)

n_pulse=(fine-inizio)
p0=np.zeros(nfreq)
L_true=np.zeros(nfreq)

for i in xrange(0,nfreq):
    p0[i]=L[i]/(rmsoffpulse[i]*np.sqrt(n_pulse))
```

```
for i in xrange(0,nfreq):
    if p0[i]<2.:
        L_true[i]=0.
    else:
        L_true[i]=np.sqrt(L[i]**2 -(rmsoffpulse[i]*np.sqrt(n_pulse))**2)

def sigmaPAcalculator(x):
    B=[ 0.00284453,  0.44833951,  0.25050409, -0.27628728,  0.08943829,-0.01204293,  0.00055808]
    if x==0.:
        return 0.
    else:
        return B[0] + B[1]/x +B[2]/x**2 +B[3]/x**3 +B[4]/x**4 +B[5]/x**5 +B[6]/x**6

P0=np.zeros(nfreq)
sigmaPA=np.zeros(nfreq)

for i in xrange(0,nfreq):
    P0[i]=L_true[i]/(rmsoffpulse[i]*np.sqrt(n_pulse))
    if np.isnan(P0[i]):
        P0[i]=0.

for i in xrange(0,nfreq):
    if P0[i]>10:
        sigmaPA[i]=1/(2*P0[i])
    else:
        sigmaPA[i]=sigmaPAcalculator(P0[i])
```

Finally I performed a least squares fit of the PAs measuring the RM. For the frequencies with very low SNR the code will not extract the error on PA. These frequencies should not be taken in consideration for the fit. Therefore I have to set the errors on PA to be large 2π (larger than the span of PA). In this part I also take care of the unwanted jumps in PA.

To measure the RM I performed a linear fit following the equation 5.1. As the x-axis the value of the wavelengths squared were inserted.

```
sigmaPA2=np.copy(sigmaPA)

for i in xrange(nfreq):
    if np.isnan(P0[i]) or sigmaPA[i]==0. or np.isnan(sigmaPA[i]):
        sigmaPA2[i]=2*pi

length =np.zeros(nfreq)
length[:]=(c/(freq[:]*10**6))

lengthsqr =np.zeros(nfreq)
lengthsqr[:]=length[:]**2

PA2=np.zeros(nfreq)
for i in xrange(nfreq):
```

```
    PA2[i]=PA[i]

for i in xrange(1,nfreq):
    if (abs(PA2[i]-PA2[i-1])>=pi/2):
        if PA2[i]>PA2[i-1]:
            PA2[i]=PA2[i]-pi
        else:
            PA2[i]=PA2[i]+pi

def lin(B, x):
    return B[0]*x + B[1]


linear = odrpack.Model(lin)

mydata = odrpack.RealData(lengthsqr, PA2, sy=sigmaPA2)
#mydata = odrpack.RealData(lengthsqr, PA2)

myodr = odrpack.ODR(mydata, linear, beta0=[0., 0.])
myodr.set_job(fit_type=2)
output = myodr.run()
output.pprint()

y=list(length)
for i in xrange(0,nfreq):
    y[i]=output.beta[0]*(length[i])**2+output.beta[1]

y2=np.zeros(nfreq)
for i in xrange(nfreq):
    y2[i]=y[i]

textstr = ' \$RM=(\%.1f \pm \%.1f)\$ rad/m\$^2\$'\%(output.beta[0]+34,np.sqrt(output.cov_beta[0][0]))

fig= plt.figure(figsize=(8,5))
ax= plt.subplot(1,1,1, axisbg='ivory')
ax.errorbar(length, PA2, yerr=sigmaPA)
ax.plot(length,y,'r-')
ax.set_xlabel('wavelength(m)')
ax.set_xlim(0.197,0.24)
#ax.set_ylim(1.3,1.6)
ax.set_ylabel('Position Angle (rad)')
ax.grid()
#And now for something completely different: number 1, the larch
props = dict(boxstyle='round', facecolor='wheat', alpha=0.5)
ax.text(0.55, 0.95, textstr, transform=ax.transAxes, fontsize=14,
        verticalalignment='top', bbox=props)

plt.show()
```

Appendix B

Monte Carlo simulation code

This is the code used to estimate the RM error for the pulsars. It is able to create a fake profile of the pulsar with the same characteristics as the real one. A random noise is added to the profile and the fake RM is measured. This procedure is repeated 1000 times. Measuring the standard deviation from the real value of the measured RM, we can estimate the error.

To create the profile we need a noiseless template made with the program *paas*. Then we need to measure the linear polarization, beginning and end of the pulse and the off-pulse region of the real data. The noise is added in a later stage. From the template we recreate the total intensity profile while the linear polarization is constructed by adding gaussian components. The height and width of these components is found imposing the percentage of linear polarization to be the same as what has been measured with the real data. The creation of the profile is completed measuring the Stokes parameters Q and U.

```
def gaussian(x, mu, sig):
    return np.exp(-np.power(x - mu, 2.) / (2 * np.power(sig, 2.)))

def PulsarCnbin():
    return 256
def PulsarC():

    nbin=PulsarCnbin()

    linpol1=8.7/100
    linpol2=22.4/100
    start1=int(0.56*nbin)
    end1=int(0.64*nbin)
    start2=int(0.64*nbin)
    end2=int(0.74*nbin)
    inizio=int(0.56*nbin)
    fine=int(0.74*nbin)
    startoff=int(0.*nbin)
    endoff=int(0.5*nbin)
    noise=1/25.
    noise_rms=1./37
```

```
    namefile= '/Volumes/Pulsar/47tuc/0023-7204Cpaas.txt'

    profile=(np.genfromtxt(namefile, skip_header=1, delimiter=' '))[:,:]

    nbinpaas=int(profile[-1,2])+1
    Ipaas=np.zeros(nbin)

    for j in xrange(0,nbin):
        Ipaas[j]=profile[j,3]

    Ipaastrue=np.zeros(shape=(nfreqtot,nbin))
    Lpaastrue=np.zeros(shape=(nfreqtot,nbin))

    m1=0
    m2=0
    for i in xrange(nfreqtot):
        Ipaastrue[i,:]=Ipaas[:]/Ipaas.max()

        m1=integrate.simps(Ipaastrue[i,start1:end1])*linpol1 /((np.sqrt(2*pi))* ((end1-start1)/4.)*0.9544)
        m2=integrate.simps(Ipaastrue[i,start2:end2])*linpol2 /((np.sqrt(2*pi))* ((end2-start2)/4.)*0.9544)
        Lpaastrue[i,:]=m1*mygaussian(np.linspace(0, nbin-1, nbin), (start1+end1)/2, (end1-start1)/4)+
                        +m2*mygaussian(np.linspace(0, nbin-1, nbin), (start2+end2)/2, (end2-start2)/4)


    return (Ipaastrue, Lpaastrue, inizio,fine,noise,noise_rms, startoff,endoff)

nbin=PulsarCnbin()
Itrue=np.zeros(shape=(nfreqtot,nbin))
Ltrue=np.zeros(shape=(nfreqtot,nbin))
(Itrue, Ltrue, inizio, fine,noise, noise_rms, startoff,endoff)= PulsarC()

Qtrue=np.zeros(shape=(nfreqtot,nbin))
Utrue=np.zeros(shape=(nfreqtot,nbin))

for i in xrange(nfreqtot):
        for j in xrange(nbin):
            Qtrue[i,j]= np.sqrt((Ltrue[i,j]**2)/((math.tan(2*PAtrue[i]))**2 + 1)) *
                            *np.sign(math.cos(2*PAtrue[i]))
            Utrue[i,j]=Qtrue[i,j] *math.tan(2*PAtrue[i])

freq=np.zeros(nfreq)
for i in xrange(0,nfreq):
    freq[i]=1241 + 312./(nfreq) *i + 312./(2*nfreq)
```

The noise that will be added to the profile is taken from the root mean square of the total intensity in the off-pulse region of the real pulsar. Inside the cycle I add to the profiles in I, Q and U a random gaussian noise with this mean intensity. For the real pulsars the noise varies for the different frequency bands. To account for this variation I measured standard deviation of the noises and randomly extracted a value for each frequency band.

```
for q in range(num):
```

```
I=np.zeros(shape=(nfreq,nbin))
Q=np.zeros(shape=(nfreq,nbin))
U=np.zeros(shape=(nfreq,nbin))

while True:
    noise_true=np.random.normal(noise,noise_rms,(nfreq))
    if (noise_true>0).all():
        break

I[:,:]=(Itrue[:,:]) +np.stack([np.random.normal(0,noise_true[i],(nbin)) for i in range(nfreq)])
Q[:,:]=(Qtrue[:,:]) +np.stack([np.random.normal(0,noise_true[i],(nbin)) for i in range(nfreq)])
U[:,:]=(Utrue[:,:]) +np.stack([np.random.normal(0,noise_true[i],(nbin)) for i in range(nfreq)])
```

Then the code proceeds measuring the RMs with the code described in the previous appendix. The results are stored in an array. Measuring the standard deviation of the set of calculated RMs gives us the error of RM for the pulsar.

Appendix C

Internal toroidal field code

To test the presence of an internal toroidal field inside the globular cluster I devised this piece of code. It takes into account all the considerations described in the corresponding chapter.

First, it calculates the maximum radius of the field lines in front of the line of sight of the pulsar. Then, it assigns to the line of sight the value of RM the pulsar would have if it was found on the plane passing through the center and orthogonal to the line of sight. In the next step, the code measures the contribution of RM due to the field lines between the pulsar and this plane. At the end the code adds or subtracts this contribution depending on whether the pulsar is in front or behind the central plane. The parameter a can be related to the strength of the magnetic field while the parameter b is the Galactic contribution to the RM.

```
def RM_function_constant_better(x,a,b):
    rad=8
    num_circ=1000
    y=np.ones(len(DM))+b
    ycenter=np.ones(len(DM))+b

    for i in range(len(DM)):
        radius=np.sqrt(rad**2-x[2,i]**2)
        num_circle=int(num_circ/rad *radius)
        circle_rad=np.linspace(0,radius,num_circle+1)

        ycenter[i]+=a*RM_central_plane(x[0,i],radius)
        y[i]=ycenter[i]
        for j in range(1,num_circle+1):
            index1=np.logical_and((circle_rad[j]>np.sqrt((x[0])**2)), (circle_rad[j]<np.sqrt((x[0])**2 +
                    +x[1]**2)), x[1]>0)
            y[index1]+= a*(x[0,index1]/circle_rad[j])*(np.sqrt((circle_rad[j]+float(radius)/num_circle)**2-
                    -x[0,index1]**2)- np.sqrt((circle_rad[j])**2-x[0,index1]**2))
            index2=np.logical_and((circle_rad[j]>np.sqrt((x[0])**2)), (circle_rad[j]<np.sqrt((x[0])**2 +
                    +x[1]**2)), x[1]<0)
            y[index2]-= a*(x[0,index2]/circle_rad[j])*(np.sqrt((circle_rad[j]+float(radius)/num_circle)**2-
                    -x[0,index2]**2) - np.sqrt((circle_rad[j])**2-x[0,index2]**2))

    return y
```

This part of the code shows how the function defined above is implemented. The fit at the end finds the best values of the magnetic field strength and of the Galactic contribution.

```
def lin(x, a, b):
    return a*x + b

DM=[C_dm,D_dm,E_dm,F_dm,G_dm,I_dm,J_dm,L_dm,N_dm,O_dm,Q_dm,T_dm,Y_dm]
DM_sigma=[C_dmsigma,D_dmsigma,E_dmsigma,F_dmsigma,G_dmsigma,I_dmsigma,J_dmsigma,
            L_dmsigma,N_dmsigma,O_dmsigma,Q_dmsigma,T_dmsigma,Y_dmsigma]
RM=[C_rm,D_rm,E_rm,F_rm,G_rm,I_rm,J_rm,L_rm,N_rm,O_rm,Q_rm,T_rm,Y_rm]
RM_sigma=[C_rmsigma,D_rmsigma,E_rmsigma,F_rmsigma,G_rmsigma,I_rmsigma,J_rmsigma,
            L_rmsigma,N_rmsigma,O_rmsigma,Q_rmsigma,T_rmsigma,Y_rmsigma]

ra=[C_coord.ra.radian,D_coord.ra.radian,E_coord.ra.radian,F_coord.ra.radian,G_coord.ra.radian,
        I_coord.ra.radian,J_coord.ra.radian,L_coord.ra.radian, N_coord.ra.radian,O_coord.ra.radian,
        Q_coord.ra.radian,T_coord.ra.radian,Y_coord.ra.radian]

dec=[C_coord.dec.radian,D_coord.dec.radian,E_coord.dec.radian,F_coord.dec.radian,G_coord.dec.radian,
        I_coord.dec.radian,J_coord.dec.radian,L_coord.dec.radian,N_coord.dec.radian,O_coord.dec.radian,
        Q_coord.dec.radian,T_coord.dec.radian,Y_coord.dec.radian]

deltaDM=DM[:]-(center_dm*np.ones(len(DM)))

deltaR=deltaDM[:]/0.067

X=ra[:]*cos(dec[:])*(np.cos(resRM.x)*np.ones(len(RM))) +dec[:]*(np.sin(resRM.x)*np.ones(len(RM)))
for i in range(len(X)):
    X[i]=X[i]-(center.ra.radian*cos(center.dec.radian)*(np.cos(resRM.x)) +center.dec.radian*
            * (np.sin(resRM.x)))
    X[i]=X[i]*4500.


Y=ra[:]*cos(dec[:])*(np.sin(resRM.x)*np.ones(len(RM))) -dec[:]*(np.cos(resRM.x)*np.ones(len(RM)))
for i in range(len(X)):
    Y[i]=Y[i]-(center.ra.radian*cos(center.dec.radian)*(np.sin(resRM.x)) -center.dec.radian*
            * (np.cos(resRM.x)))
    Y[i]=Y[i]*4500.

ingresso=np.zeros((3,len(X)))

for i in range(len(X)):
    ingresso[0,i]=X[i]
    ingresso[1,i]=deltaR[i]
    ingresso[2,i]=Y[i]

popt,pcov=scipy.optimize.curve_fit(RM_function_constant_better, ingresso, RM,sigma=RM_sigma,p0=(0.1,15))
```

Bibliography

J. G. Ables, C. E. Jacka, D. McConnell, P. M. McCulloch, and P. J. Hall. A millisecond pulsar in a 32-minute binary orbit. *Nature*, 342:158–161, 1989.

L. G. Ables and R. N. Manchester. Hydrogen-line absorption observations of distant pulsars. *Astronomy and Astrophysics*, 50:177–184, 1976.

T. Akahori, D. Ryu, J. Kim, and B. M. Gaensler. Simulated faraday rotation measures toward high galactic latitudes. *The Astrophysical Journal*, 767, 2013.

J. Antoniadis, P. C. C. Freire, N. Wex, T. M. Tauris, R. S. Lynch, M. H. van Kerkwijk, M. Kramer, C. Bassa, V. S. Dhillon, T. Driebe, J. W. T. Hessels, V. M. Kaspi, V. I. Kondratiev, N. Langer, T. R. Marsh, M. A. McLaughlin, T. T. Pennucci, S. M. Ransom, I. H. Stairs, J. van Leeuwen, J. P. W. Verbiest, and D. G. Whelan. A massive pulsar in a compact relativistic binary. *Science*, 340:448, 2013.

J. W. Armstrong, B. J. Rickett, and S. R. Spangler. Electron density power spectrum in the local interstellar medium. *The Astrophysical Journal*, 443:209–221, 1995.

W. Baade and F. Zwicky. Cosmic rays from super-novae. *Proceedings of the National Academy of Sciences of the United States of America*, 20:259–263, 1934.

D. C. Backer, S. R. Kulkarni, C. Heiles, M. M. Davis, and W. M. Goss. A millisecond pulsar. *Nature*, 300:615–618, 1982.

D. C. Backer, R. S. Foster, and S. Sallmen. A second companion of the millisecond pulsar 1620 - 26. *Nature*, 365:817–819, 1993.

P. Barmby, M. L. Boyer, R. D. Woodward, C. E. Gehrz, J. T. van Loon, G. G. Fazio, M. Marengo, and E. Polomski. A spitzer search for cold dust within globular clusters. *The Astronomical Journal*, 137:207–217, 2009.

R. Beck. Magnetic fields in spiral galaxies. *The Astronomy and Astrophysics Review*, 24, 2016.

R. Beck, A. Brandenburg, D. Moss, A. Shukurov, and D. Sokoloff. Galactic magnetism: Recent developments and perspectives. *Annual Review of Astronomy and Astrophysics*, 34:155–206, 1996.

A. Bellini, L. R. Bedin, G. Piotto, A. P. Milone, A. F. Marino, and S. Villanova. New Hubble Space Telescope WFC3/UVIS Observations Augment the Stellar-population Complexity of ω Centauri. *The Astronomical Journal*, 140:631–641, 2010.

D. Bhattacharya and E. P. J. van den Heuvel. Formation and evolution of binary and millisecond radio pulsars. *Physics Report*, 203:1–124, 1991.

P. Bianchini, A. L. Varri, G. Bertin, and A. Zocchi. Rotating globular clusters. *The Astrophysical Journal*, 772:67–86, 2013.

G. F. Bignami, P. A. Caraveo, A. De Luca, and S. Mereghetti. The magnetic field of an isolated neutron star from x-ray cyclotron absorption lines. *Nature*, 423:725–727, 2003.

J. Binney and M. Merrifield. *Galactic Astronomy*. Princeton University Press, Princeton, 1998.

J. Binney and S. Tremaine. *Galactic Dynamics*. Princeton University Press, Princeton, 2008.

S. Bogdanov, J. E. Grindlay, Craig O. Heinke, F. Camilo, P. C. C. Freire, and W. Becker. Chandra x-ray observations of 19 millisecond pulsars in the globular cluster 47 tucanae. *The Astrophysical Journal*, 646:1104–1115, 2006.

R.S. Booth and J. L. Jonas. An overview of the meerkat project. *African Skies*, 16:101, 2012.

R. Buonanno, C. E. Corsi, A. Buzzoni, C. Cacciari, F. R. Ferraro, and F. Fusi Pecci. The stellar population of the globular cluster m 3. i. photographic photometry of 10 000 stars. *Astronomy and Astrophysics*, 290:69–103, 1994.

M. Burgay, N. D'Amico, A. Possenti, R. N. Manchester, A. G. Lyne, B. C. Joshi, M. A. McLaughlin, M. Kramer, J. M. Sarkissian, F. Camilo, V. Kalogera, C. Kim, and D. R. Lorimer. An increased estimate of the merger rate of double neutron stars from observations of a highly relativistic system. *Nature*, 426:531–533, 2003.

M. Cadelano, C. Pallanca, F. R. Ferraro, M. Salaris, E. Dalessandro, B. Lanzoni, and P. C. C. Freire. Optical identification of he white dwarfs orbiting four millisecond pulsars in the globular cluster 47 tucanae. *The Astrophysical Journal*, 812, 2015.

F. Camilo and F. A. Rasio. Pulsars in globular clusters. In *Binary Radio Pulsars, ASP Conference Series*, page 147, Aspen, Colorado, USA, 2005.

F. Camilo, D. R. Lorimer, P. Freire, A. G. Lyne, and R. N. Manchester. Observations of 20 millisecond pulsars in 47 tucanae at 20 centimeters. *The Astrophysical Journal*, 535:975–990, 2000.

S. Chatterjee, J. M. Fregeau, and F. A. Rasio. Effects of stellar collisions on star cluster evolution and core collapse. In *Dynamical Evolution of Dense Stellar Systems, Proceedings of the International Astronomical Union, IAU Symposium*, volume 246, pages 151–155, 2008.

C. W. Chen and W. P. Chen. Morphological distortion of galactic globular clusters. *The Astrophysical Journal*, 721:1790–1819, 2010.

C. Chiuderi and M. Velli. *Basic of plasma astrophysics*. Springer-Verlag Italia, Milan, Italy, 2015.

M. L. Cioni, K. Bekki, L. Girardi, R. de Grijs, M. J. Irwin, V. D. Ivanov, M. Marconi, J. M. Oliveira, A. E. Piatti, V. Ripepi, and J. T. van Loon. The vmc survey. xvii. proper motions of the small magellanic cloud and the milky way globular cluster 47 tucanae. *Astronomy and Astrophysics*, 586, 2016.

D. Clausen, S. Sigurdsson, and D. F. Chernoff. Dynamically formed black hole+millisecond pulsar binaries in globular clusters. *Monthly Notices of the Royal Astronomical Society*, 442:207–219, 2014.

S. A. Colgate and R. H. White. The hydrodynamic behavior of supernovae explosions. *Astrophysical Journal*, 143:626, 1966.

M. Colpi and B. Devecchi. Dynamical formation and evolution of neutron star and black hole binaries in globular clusters. In M. Colpi, P. Casella, V. Gorini, U. Moschella, and A. Possenti, editors, *Physics of Relativistic Objects in Compact Binaries: From Birth to Coalescence*, pages 199–244. Springer, Dordrecht, The Netherlands, 2009.

C. Conroy and D. N. Spergel. On the formation of multiple stellar populations in globular clusters. *The Astrophysical Journal*, 726, 2011.

G. B. Cook, S. L. Shapiro, and S. A. Teukolsky. Recycling pulsars to millisecond periods in general relativity. *The Astrophysical Journal Letters*, 423:L117, 1994.

J. M. Cordes and T. J. W. Lazio. Ne2001.i. a new model for the galactic distribution of free electrons and its fluctuations. *eprint arXiv:astro-ph/0207156*, 2002.

J. M. Cordes and T. J. W. Lazio. Ne2001. ii. using radio propagation data to construct a model for the galactic distribution of free electrons. *eprint arXiv:astro-ph/0301598*, 2003.

F. Crawford, B. M. Gaensler, V. M. Kaspi, R. N. Manchester, F. Camilo, A. G. Lyne, and M. J. Pivovaroff. A radio supernova remnant associated with the young pulsar j1119-6127. *The Astrophysical Journal*, 554:152–160, 2001.

N. D'Amico and M. Burgay. Perspective in the search for relativistic pulsars. In M. Colpi, P. Casella, V. Gorini, U. Moschella, and A. Possenti, editors, *Physics of Relativistic Objects in Compact Binaries: From Birth to Coalescence*, pages 77–124. Springer, Dordrecht, The Netherlands, 2009.

B. Devecchi, M. Colpi, M. Mapelli, and A. Possenti. Millisecond pulsars around intermediate-mass black holes in globular clusters. *Monthly Notices of the Royal Astronomical Society*, 380:691–702, 2007.

A. K. Dupree, Graeme H. Smith, and J. Strader. Fast winds and mass loss from metal-poor field giants. *The Astrophysical Journal*, 138:1485–1501, 2009.

P. D. Edmonds, R. L. Gilliland, Craig O. Heinke, Jonathan E. Grindlay, and F. Camilo. Optical detection of a variable millisecond pulsar companion in 47 tucanae. *The Astrophysical Journal*, 557:L57–L60, 2001.

P. D. Edmonds, R. L. Gilliland, F. Camilo, C. O. Heinke, and J. E. Grindlay. A millisecond pulsar optical counterpart with large-amplitude variability in the globular cluster 47 tucanae. *The Astrophysical Journal*, 579:741–751, 2002.

R. T. Edwards, G. B. Hobbs, and R. N. Manchester. Tempo2, a new pulsar timing package - ii. the timing model and precision estimates. *Monthly Notices of the Royal Astronomical Society*, 372: 1549–1574, 2006.

J. E. Everett and J. M. Weisberg. Emission beam geometry of selected pulsars derived from average pulse polarization data. *The Astrophysical Journal*, 553:341–357, 2001.

F. Ferraro, B. Lanzoni, E. Dalessandro, A. Mucciarelli, and L. Lovisi. *Ecology of Blue Straggler Stars.* Springer-Verlag Berlin Heidelberg, 2015.

J. Frank and G. Gisler. The fate of gas in globular clusters. *Monthly Notices of the Royal Astronomical Society*, 176:533–538, 1976.

P. C. C. Freire. The pulsar population in globular clusters and in the galaxy. *Proceedings of the International Astronomical Union*, 291:243–50, 2013.

P. C. C. Freire, F. Camilo, D. R. Lorimer, A. G. Lyne, R. N. Manchester, and N. D'Amico. Timing the millisecond pulsars in 47 tucanae. *Monthly Notices of the Royal Astronomical Society*, 326: 901–915, 2001a.

P. C. C. Freire, M. Kramer, A. G. Lyne, F. Camilo, R. N. Manchester, and N. D'Amico. Detection of ionized gas in the globular cluster 47 tucanae. *The Astrophysical Journal Letters*, 557:L105–108, 2001b.

P. C. C. Freire, F. Camilo, M. Kramer, D. R. Lorimer, A. G. Lyne, R. N. Manchester, and N. D'Amico. Further results from the timing of the millisecond pulsars in 47 tucanae. *Monthly Notices of the Royal Astronomical Society*, 340:1359–1374, 2003.

G. Ghisellini. *Radiative Processes in High Energy Astrophysics.* Springer International, Heidelberg, Germany, 2013.

O. Y. Gnedin, H. Zhao, J. E. Pringle, S. M. Fall, M. Livio, and G. Meylan. The unique history of the globular cluster ω centauri. *The Astrophysical Journal Letters*, 568:L23–L26, 2002.

T. Gold. Rotating neutron stars as the origin of the pulsating radio sources. *Nature*, 218:731–732, 1968.

P. Goldreich and W. H. Julian. Pulsar electrodynamics. *The Astrophysical Journal*, 157:869, 1969.

R. G. Gratton, F. Fusi Pecci, E. Carretta, G. Clementini, C. E. Corsi, and M. Lattanzi. Ages of globular clusters from hipparcos parallaxes of local subdwarfs. *The Astrophysical Journal*, 491: 749–771, 1997.

J. L. Han, R. N. Manchester, A. G. Lyne, G. J. Qiao, and W. van Straten. Pulsar rotation measures and the large-scale structure of the galactic magnetic field. *The Astrophysical Journal*, 642:868–881, 2006.

A. K. Harding and A. G. Muslimov. Pulsar pair cascades in magnetic fields with offset polar caps. *The Astrophysical Journal*, 743, 2011.

A. K. Harding, V. V. Usov, and A. G. Muslimov. High-energy emission from millisecond pulsars. *The Astrophysical Journal*, 622:531–543, 2005.

W. E. Harris. A new catalog of globular clusters in the milky way. *eprint arXiv:1012.3224*, 2010.

M. Haverkorn and V. Heesen. Magnetic fields in galactic haloes. *Space Science Reviews*, 166: 133–144, 2012.

M. Haverkorn, J. C. Brown, B. M. Gaensler, and N. M. McClure-Griffiths. The outer scale of turbulence in the magnetoionized galactic interstellar medium. *The Astrophysical Journal*, 680, 2008.

C. Heiles, P. Perillat, M. Nolan, D. Lorimer, R. Bhat, T. Ghosh, M. Lewis, K. O'Neil, C. Salter, and S. Stanimirovic. Mueller matrix parameters for radio telescopes and their observational determination. *The Publications of the Astronomical Society of the Pacific*, 113:1274–1288, 2001.

C. O. Heinke, J. E. Grindlay, P. D. Edmonds, H. N. Cohn, P. M. Lugger, F. Camilo, S. Bogdanov, and P. C. Freire. A deep chandra survey of the globular cluster 47 tucanae: Catalog of point sources. *The Astrophysical Journal*, 625:796–824, 2005.

J. Hessels, A. Possenti, M. Bailes, C. Bassa, P. C. C. Freire, D. R. Lorimer, R. Lynch, S. M. Ransom, and I. H. Stairs. Pulsars in globular clusters with the ska. In *Proceedings of Advancing Astrophysics with the Square Kilometre Array*, volume 1, pages 355–370, Giardini Naxos, Italy, 2015.

J. W. T. Hessels, S. M. Ransom, I. H. Stairs, P. C. C. Freire, V. M. Kaspi, and F. Camilo. A radio pulsar spinning at 716 hz. *Science*, 311:1901–1904, 2006.

A. Hewish. Pulsars and high density physics. *Science*, 188:1079–1083, 1975.

A. Hewish, S. J. Bell, J. D. H. Pilkington, P. F. Scott, and R. A. Collins. Observation of a rapidly pulsating radio source. *Nature*, 217:709–713, 1968.

Anna Ho, S. M. Ransom, and P. Demorest. Rotation measures of globular cluster pulsars as a unique probe of the galactic magnetic field. *American Astronomical Society, AAS Meeting n.223, id.153.18*, 2013.

G. Hobbs, R. Edwards, and R. Manchester. Tempo2: a new pulsar timing package. *Chinese Journal of Astronomy and Astrophysics*, 6:189–192, 2006.

A. W. Hotan, W. van Straten, and R. N. Manchester. Psrchive and psrfits: An open approach to radio pulsar data storage and analysis. *Publications of the Astronomical Society of Australia*, 21: 303–309, 2004.

F. Hoyle. Magnetic fields and highly condensed objects. *Nature*, 223:936, 1969.

F. Hoyle, W. A. Fowler, G. R. Burbidge, and E. M. Burbidge. The hydrodynamic behavior of supernovae explosions. *Astrophysical Journal*, 139:909, 1964.

R. A. Hulse and J. H. Tayolr. Discovery of a pulsar in a binary system. *The Astrophysical Journal*, 195:L51–L53, 1975.

M. Iacobelli, M. Haverkorn, E. Orrù, R. F. Pizzo, J. Anderson, R. Beck, M. R. Bell, A. Bonafede, K. Chyzy, R.-J. Dettmar, T. A. Enßlin, G. Heald, C. Horellou, A. Horneffer, W. Jurusik, H. Junklewitz, M. Kuniyoshi, D. D. Mulcahy, R. Paladino, W. Reich, A. Scaife, C. Sobey, C. Sotomayor-Beltran, A. Alexov, A. Asgekar, I. M. Avruch, M. E. Bell, I. van Bemmel, M. J.

Bentum, G. Bernardi, P. Best, L. Brzan, F. Breitling, J. Broderick, W. N. Brouw, M. Brüggen, H. R. Butcher, B. Ciardi, J. E. Conway, F. de Gasperin, E. de Geus, S. Duscha, J. Eislöffel, D. Engels, H. Falcke, R. A. Fallows, C. Ferrari, W. Frieswijk, M. A. Garrett, J. Grießmeier, A. W. Gunst, J. P. Hamaker, T. E. Hassall, J. W. T. Hessels, M. Hoeft, J. Hörandel, V. Jelic, A. Karastergiou, V. I. Kondratiev, L. V. E. Koopmans, M. Kramer, G. Kuper, J. van Leeuwen, G. Macario, G. Mann, J. P. McKean, H. Munk, M. Pandey-Pommier, A. G. Polatidis, H. Röttgering, D. Schwarz, J. Sluman, O. Smirnov, B. W. Stappers, M. Steinmetz, M. Tagger, Y. Tang, C. Tasse, C. Toribio, R. Vermeulen, C. Vocks, C. Vogt, R. J. van Weeren, M. W. Wise, O. Wucknitz, S. Yatawatta, P. Zarka, and A. Zensus. Studying galactic interstellar turbulence through fluctuations in synchrotron emission. first lofar galactic foreground detection. *Astronomy and Astrophysics*, 558, 2013.

M. Johnston-Hollitt, C. P. Hollitt, and R. D. Ekers. Statistical analysis of extra-galactic rotation measures. In *The Magnetized Interstellar Medium*, pages 13–18, Antalya, Turkey, 2004.

J. S. Kalirai. Applications of the initial to final mass relation: the age of the galactic halo. *Memorie della Societa Astronomica Italiana*, 84:58, 2013.

A. Karastergiou and S. Johnston. Absolute polarization position angle profiles of southern pulsars at 1.4 and 3.1 ghz. *Monthly Notices of the Royal Astronomical Society*, 365:353–366, 2006.

A. Karastergiou, S. Johnston, and R. N. Manchester. Polarization profiles of southern pulsars at 3.1 ghz. *Monthly Notices of the Royal Astronomical Society*, 359:481–492, 2005.

V. M. Kaspi and D. J. Helfand. Constraining the birth events of neutron stars. In *Neutron Stars in Supernova Remnants, ASP Conference Series*, volume 271, page 3, Boston, MA, USA, 2002.

I. R. King. The structure of star clusters. iii. some simple dynamical models. *Astronomical Journal*, 71:64, 1966.

R. Kippenhahn, A. Weigert, and A. Weiss. *Stellar Structure and Evolution*. Springer-Verlag Berlin Heidelberg, 2012.

J. G. Kirk, Y. Lyubarsky, and J. Petri. The theory of pulsar winds and nebulae. In W. Becker, editor, *Neutron Stars and Pulsars*, pages 421–450. Springer-Verlag, Berlin, 2009.

C. Knigge, A. Dieball, J. Maíz Apellániz, K. S. Long, D. R. Zurek, and M. M. Shara. Stellar exotica in 47 tucanae. *The Astrophysical Journal*, 683:1006–1030, 2008.

A. N. Kolmogorov. The local structure of turbulence in incompressible viscous fluid for very large reynolds' numbers. *C. R. Acad. Sci. USSR*, 30:201–206, 1941.

M. Kramer, I. H. Stairs, R. N. Manchester, M. A. McLaughlin, A. G. Lyne, R. D. Ferdman, M. Burgay, D. R. Lorimer, A. Possenti, N. D'Amico, J. M. Sarkissian, G. B. Hobbs, J. E. Reynolds, P. C. C. Freire, and F. Camilo. Tests of general relativity from timing the double pulsar. *Science*, 314:97–102, 2006.

J. M. D. Kruijssen. Globular clusters as the relics of regular star formation in 'normal' high-redshift galaxies. *Monthly Notices of the Royal Astronomical Society*, 454:1658–1686, 2015.

J. M. Lamarre, J. L. Puget, F. Bouchet, P. A. R. Ade, A. Benoit, J. P. Bernard, J. Bock, P. De Bernardis, J. Charra, F. Couchot, J. Delabrouille, G. Efstathiou, M. Giard, G. Guyot, A. Lange, B. Maffei, A. Murphy, F. Pajot, M. Piat, I. Ristorcelli, D. Santos, R. Sudiwala, J. F. Sygnet, J. P. Torre, V. Yurchenko, and D. Yvon. The planck high frequency instrument, a third generation cmb experiment, and a full sky submillimeter survey. *New Astronomy Reviews*, 47: 1017–1024, 2003.

L. D. Landau. On the theory of stars. *Phys. Zs. Sowjet*, 1, 1932.

R. R. Lane, L. L. Kiss, G. F. Lewis, R. A. Ibata, A. Siebert, T. R. Bedding, and P. Székely. Testing newtonian gravity with aaomega: mass-to-light profiles and metallicity calibrations from 47 tuc and m55. *Monthly Notices of the Royal Astronomical Society*, 401:2521–2530, 2010.

S. Leon and F. Combes. Search for co emission in globular clusters. *Astronomy and Astrophysics*, 309:123–128, 1996.

A. Levinson and D. Eichler. Can neutron stars ablate their companions? *The Astrophysical Journal*, 379:359–365, 1991.

X. H. Li and J. L. Han. The effect of scatteing on pulsar polarization angle. *Astronomy and Astrophysics*, 410:253–256, 2003.

M. S. Longair. *Galaxy Formation*. Springer-Verlag, Berlin, Germany, 2008.

M. S. Longair. *High Energy Astrophysics*. Cambridge University Press, Cambridge, UK, 2011.

D. R. Lorimer. Binary and millisecond pulsars. *Living Reviews in Relativity*, 11, 2008.

D. R. Lorimer and M. Kramer. *Handbook of Pulsar Astronomy*. Cambridge University Press, Cambridge, UK, 2005.

A. G. Lyne and D. R. Lorimer. High birth velocities of radio pulsars. *Nature*, 369:127–129, 1994.

A. G. Lyne and R. N. Manchester. The shape of pulsar radio beams. *Monthly Notices of the Royal Astronomical Society*, 234:477–508, 1988.

A. G. Lyne and F. Graham Smith. Pulsar rotation measures and the galactic magnetic field. *Monthly Notices of the Royal Astronomical Society*, 237:533–541, 1989.

A. G. Lyne, A. Brinklow, J. Middleditch, S. R. Kulkarni, and D. C. Backer. The discovery of a millisecond pulsar in the globular cluster m28. *Nature*, 328:399–401, 1987.

A. G. Lyne, R. N. Manchester, and N. D'Amico. Psr b1745-20 and young pulsars in globular clusters. *The Astrophysical Journal Letters*, 460:L41, 1996.

A. G. Lyne, M. Burgay, M. Kramer, A. Possenti, R. N. Manchester, F. Camilo, M. A. McLaughlin, D. R. Lorimer, N. D'Amico, B. C. Joshi, J. Reynolds, and P. C. C. Freire. A double-pulsar system: A rare laboratory for relativistic gravity and plasma physics. *Science*, 303:1153–1157, 2004.

M. A. Malkov, P. H. Diamond, L. O'C. Drury, and R. Z. Sagdeev. Probing nearby cosmic-ray accelerators and interstellar medium turbulence with milagro hot spots. *The Astrophysical Journal*, 721:750–761, 2010.

R. N. Manchester. Pulsar rotation and dispersion measures and the galactic magnetic field. *The Astrophysical Journal*, 172:43, 1972.

R. N. Manchester. Observational properties of pulsars. *Science*, 304:542–547, 2004.

R. N. Manchester and J. H. Taylor. *Pulsars*. W. H. Freeman, San Fransisco, 1977.

R. N. Manchester, A. G. Lyne, C. Robinson, M. Bailes, and N. D'Amico. Discovery of ten millisecond pulsars in the globular cluster 47 tucanae. *Nature*, 352:219–221, 1991.

S. A. Mao, B. M. Gaensler, S. Stanimirović, M. Haverkorn, N. M. McClure-Griffiths, L. Staveley-Smith, and J. M. Dickey. A radio and optical polarization study of the magnetic field in the small magellanic cloud. *The Astrophysical Journal*, 688:1029–1049, 2008.

S. A. Mao, B. M. Gaensler, M. Haverkorn, E. G. Zweibel, G. J. Madsen, N. M. McClure-Griffiths, A. Shukurov, and P. P. Kronberg. A survey of extragalactic faraday rotation at high galactic latitude: The vertical magnetic field of the milky way toward the galactic poles. *The Astrophysical Journal*, 714:1170–1186, 2010.

I. McDonald and A. A. Zijlstra. Globular cluster interstellar media: ionized and ejected by white dwarfs. *Monthly Notices of the Royal Astronomical Society*, 446:2226–2242, 2015.

I. McDonald, M. L. Boyer, J. Th. van Loon, and A. A. Zijlstra. Dust production and mass loss in the galactic globular cluster 47 tucanae. *The Astrophysical Journal*, 730, 2011.

I. McDonald, A. A. Zijlstra, E. Lagadec, G. C. Sloan, M. L. Boyer, M. Matsuura, R. J. Smith, C. L. Smith, J. A. Yates, J. Th. van Loon, O. C. Jones, S. Ramstedt, A. Avison, K. Justtanont, H. Olofsson, J. A. D. L. Blommaert, S. R. Goldman, and M. A. T. Groenewegen. Alma reveals sunburn: Co dissociation around agb stars in the globular cluster 47 tucanae. *Monthly Notices of the Royal Astronomical Society*, 453:4324–4336, 2015.

M. M. McKinnon and D. R. Stinebring. The mode-separated pulse profiles of pulsar radio emission. *The Astrophysical Journal*, 529:435–446, 2000.

D. E. McLaughlin, J. Anderson, G. Meylan, K. Gebhardt, C. Pryor, D. Minniti, and S. Phinney. Hubble space telescope proper motions and stellar dynamics in the core of the globular cluster 47 tucanae. *The Astrophysical Journal Supplement Series*, 166:249–297, 2006.

G. Meylan and D. C. Heggie. Internal dynamics of globular clusters. *The Astronomy and Astrophysics Review*, 8:1–143, 1997.

A. P. Milone, G. Piotto, L. R. Bedin, J. Anderson, A. F. Marino, A. Bellini, R. Gratton, A. Renzini, P. B. Stetson, S. Cassisi, A. Aparicio, A. Bragaglia, E. Carretta, F. D'Antona, M. Di Criscienzo, S. Lucatello, M. Monelli, and A. Pietrinferni. Multiple stellar populations in 47 tucanae. *The Astrophysical Journal*, 744, 2012.

P. Miocchi, B. Lanzoni, F. R. Ferraro, E. Dalessandro, E. Vesperini, M. Pasquato, G. Beccari, C. Pallanca, and N. Sanna. Star count density profiles and structural parameters of 26 galactic globular clusters. *The Astrophysical Journal*, 774:151, 2013.

D. Moss and A. Shukurov. Turbulence and magnetic fields in elliptical galaxies. *Monthly Notices of the Royal Astronomical Society*, 279:229–239, 1996.

H. Mueller. M.i.t. course (8.26). *J. Opt. Soc. Am.*, 38:661, 1948.

J. Naghizadeh-Khouei and D. Clarke. On the statistical behaviour of the position angle of linear polarization. *Astronomy and Astrophysics*, 273:968, 1993.

J. Naiman, M. Soares-Furtado, and E. Ramirez-Ruiz. Modeling the tenuous intracluster medium in globular clusters. *eprint arXiv:1310.8301*, 2013.

A. Noutsos, S. Johnston, M. Kramer, and A Karastergiou. New pulsar rotation measures and the galactic magnetic field. *Monthly Notices of the Royal Astronomical Society*, 386:1881–1896, 2008.

R. W. O'Connell, B. Dorman, R. Y. Shah, R. T. Rood, W. B. Landsman, A. N. Witt, R. C. Bohlin, S. G. Neff, M. S. Roberts, A. M. Smith, and T. P. Stecher. Ultraviolet imaging of the globular cluster 47 tucanae. *The Astronomical Journal*, 114:1982, 1997.

M. Odenkirchen, P. Brosche, M. Geffert, and H-J. Tucholke. Globular cluster orbits based on hipparcos proper motions. *New Astronomy*, 2:477–499, 1997.

H. Ohno and S. Shibata. The random magnetic field in the galaxy. *Monthly Notices of the Royal Astronomical Society*, 262:953–962, 1993.

M. Opher, F. Alouani Bibi, G. Toth, J. D. Richardson, V. V. Izmodenov, and T. I. Gombosi. A strong, highly-tilted interstellar magnetic field near the solar system. *Nature*, 462:1036–1038, 2009.

J. R. Oppenheimer and G. M. Volkoff. On massive neutron cores. *Physical Review*, 55:374–381, 1939.

N. Oppermann, H. Junklewitz, G. Robbers, M. R. Bell, T. A. Enßlin, A. Bonafede, R. Braun, J. C. Brown, T. E. Clarke, I. J. Feain, B. M. Gaensler, A. Hammond, L. Harvey-Smith, G. Heald, M. Johnston-Hollitt, U. Klein, P. P. Kronberg, S. A. Mao, N. M. McClure-Griffiths, S. P. O'Sullivan, L. Pratley, T. Robishaw, S. Roy, D. H. F. M. Schnitzeler, C. Sotomayor-Beltran, J. Stevens, J. M. Stil, C. Sunstrum, A. Tanna, A. R. Taylor, and C. L. Van Eck. An improved map of the galactic faraday sky. *Astronomy and Astrophysics*, 542, 2012.

N. Oppermann, H. Junklewitz, M. Greiner, T. A. Enßlin, T. Akahori, E. Carretti, B. M. Gaensler, A. Goobar, L. Harvey-Smith, M. Johnston-Hollitt, L. Pratley, D. H. F. M. Schnitzeler, J. M. Stil, and V. Vacca. An improved map of the galactic faraday sky. *Astronomy and Astrophysics*, 575, 2015.

L. Origlia, R. Gredel, F. R. Ferraro, and F. Fusi Pecci. Co mapping of the central regions of the globular clusters omicroncen and 47tuc. *Monthly Notices of the Royal Astronomical Society*, 289:948–954, 1997.

Z. Pan, G. Hobbs, D. Li, A. Ridolfi, P. Wang, and P. Freire. Discovery of two new pulsars in 47 tucanae (ngc 104). *eprint arXiv:1603.01348*, 2016.

E. N. Parker. Fast dynamos, cosmic rays, and the galactic magnetic field. *The Astrophysical Journal*, 401:137–145, 1992.

H. C. Plummer. On the problem of distribution in globular star clusters. *Monthly Notices of the Royal Astronomical Society*, 71:460, 1911.

W. Priestley, M. Ruffert, and M. Salaris. On the evolution of intracluster gas within galactic globular clusters. *Monthly Notices of the Royal Astronomical Society*, 411:1935–1952, 2011.

T. A. Prince, S. B. Anderson, S. R. Kulkarni, and A. Wolszczan. Timing observations of the 8 hour binary pulsar 2127 + 11C in the globular cluster M15. *The Astrophysical Journal Letters*, 374: L41–L44, 1991.

C. Pryor and G. Meylan. Velocity dispersions for galactic globular clusters. In *Structure and Dynamics of Globular Clusters, Proceedings of a Workshop held in Berkeley, California, July 15-17, 1992*, volume 50, page 357. Astronomical Society of the Pacific, 1993.

V. Radhakrishnan and D. J. Cook. Magnetic poles and the polarization structure of pulsar radiation. *Astrophysical Letters*, 3:225, 1969.

J. M. Rankin. Toward an empirical theory of pulsar emission. i morphological taxonomy. *The Astrophysical journal*, 274:333–358, 1983.

S. M. Ransom, I. H. Stairs, A. M. Archibald, J. W. T. Hessels, D. L. Kaplan, M. H. van Kerkwijk, J. Boyles, A. T. Deller, S. Chatterjee, A. Schechtman-Rook, A. Berndsen, R. S. Lynch, D. R. Lorimer, C. Karako-Argaman, V. M. Kaspi, V. I. Kondratiev, M. A. McLaughlin, J. van Leeuwen, R. Rosen, M. S. E. Roberts, and K. Stovall. A millisecond pulsar in a stellar triple system. *Nature*, 505:520–524, 2014.

L. E. Rivera-Sandoval, M. van den Berg, C. O. Heinke, H. N. Cohn, P. M. Lugger, P. Freire, J. Anderson, A. M. Serenelli, L. G. Althaus, A. M. Cool, J. E. Grindlay, P. D. Edmonds, R. Wijnands, and N. Ivanova. Discovery of near-ultraviolet counterparts to millisecond pulsars in the globular cluster 47 tucanae. *Monthly Notices of the Royal Astronomical Society*, 453:2707–2717, 2015.

Clive Robinson, A. G. Lyne, R. N. Manchester, M. Bailes, N. D'Amico, and S. Johnston. Millisecond pulsars in the globular cluster 47 tucanae. *Monthly Notices of the Royal Astronomical Society*, 274:547–554, 1995.

S. Roy, A. Pramesh Rao, and R. Subrahmanyan. Magnetic field near the central region of the galaxy: rotation measure of extragalactic sources. *Astronomy and Astrophysics*, 478:435–442, 2008.

B. Ryden. *Dynamics*. The Ohio State University, Ohio, USA, 2016.

R. P. Schiavon, E. Dalessandro, S. T. Sohn, R. T. Rood, R. W. O'Connell, F. R. Ferraro, B. Lanzoni, G. Beccari, S. Rey, J. Rhee, R. M. Rich, S. Yoon, and Y. Lee. Ultraviolet properties of galactic globular clusters with galex. i. the color-magnitude diagrams. *The Astronomical Journal*, 143, 2012.

D. H. F. M. Schnitzeler. The latitude dependence of the rotation measures of nvss sources. *Monthly Notices of the Royal Astronomical Society: Letters*, 409:L99–L103, 2010.

E. H. Scott and R. H. Durisen. Nova-driven winds in globular clusters. *The Astrophysical Journal*, 222:612–620, 1978.

S. L. Shapiro and S. A. Teukolsky. *Black Hole, White Dwarfs and Neutron Stars: The Physics of Compact Objects*. Wiley & Sons, NY-NY, USA, 1983.

S. Sigurdsson, H. B. Richer, B. M. Hansen, I. H. Stairs, and S. E. Thorsett. A young white dwarf companion to pulsar b1620-26: Evidence for early planet formation. *Science*, 301:193–196, 2003.

J. F. L. Simmons and B. G. Stewart. Point and interval estimation of the true unbiased degree of linear polarization in the presence of low signal-to-noise ratios. *Astronomy and Astrophysics*, 142:100–106, 1985.

G. H. Smith, A. K. Dupree, and J. Strader. He i λ10830 absorption in metal-poor red giants: Probing fast chromospheric outflows. *The Publications of the Astronomical Society of the Pacific*, 116: 819–825, 2004.

B. V. Somov. *Plasma Astrophysics part I.* Springer, New York, NY, USA, 2006.

S. R. Spangler. Plasma turbulence in the local bubble. *Space Science Reviews*, 143:277–290, 2009.

D. N. Spergel. Evacuation of gas from globular clusters by winds from millisecond pulsars. *Nature*, 352:221–222, 1991.

L. Spitzer. *Dynamical evolution of globular clusters.* Princeton University Press, Princeton, 1987.

L. Staveley-Smith, W. E. Wilson, T. S. Bird, M. J. Disney, R. D. Ekers, K. C. Freeman, R. F. Haynes, M. W. Sinclair, R. A. Vaile, R. L. Webster, and A. E. Wright. The parkes 21 cm multibeam receiver. *Publications Astronomical Society of Australia*, 13:243–248, 1996.

G. Stokes. *Trans. Camb. Phil. Soc.*, 9:399, 1852.

H. Su, Q. Li, H. Zhu, and W. Tian. 78 pairs of possible psr-snr associations. *arXiv:1306.6509*, 2013.

T. K. Suzuki. Structured red giant winds with magnetized hot bubbles and the corona/cool wind dividing line. *The Astrophysical Journal*, 659:1592–1610, 2007.

A. R. Taylor, J. M. Stil, and C. Sunstrum. A rotation measure image of the sky. *The Astrophysical Journal*, 702:1230–1236, 2009.

J. H. Taylor and J. M. Cordes. A catalog of parameters for globular clusters in the milky way. *The Astrophysical Journal*, 411:674–684, 1993.

S. E. Thorsett, Z. Arzoumanian, F. Camilo, and A. G. Lyne. The triple pulsar system psr b1620-26 in m4. *The Astrophysical Journal*, 523:763–770, 1999.

C. Tiburzi, S. Johnston, M. Bailes, S. D. Bates, N. D. R. Bhat, M. Burgay, S. Burke-Spolaor, D. Champion, P. Coster, N. D'Amico, M. J. Keith, M. Kramer, L. Levin, S. Milia, C. Ng, A. Possenti, B. W. Stappers, D. Thornton, and W. van Straten. The high time resolution universe survey - ix. polarimetry of long-period pulsars. *Monthly Notices of the Royal Astronomical Society*, 436:3557–3572, 2013.

E. P. J. van den Heuvel. The formation and evolution of relativistic binaries. In M. Colpi, P. Casella, V. Gorini, U. Moschella, and A. Possenti, editors, *Physics of Relativistic Objects in Compact Binaries: From Birth to Coalescence*, pages 125–198. Springer, Dordrecht, The Netherlands, 2009.

J. T. van Loon, S. Stanimirovic, A. Evans, and E. Muller. Stellar mass loss and the intracluster medium in galactic globular clusters: a deep radio survey for h i and oh. *Monthly Notices of the Royal Astronomical Society*, 365:1277–1282, 2006.

W. van Straten. Radio astronomical polarimetry and point-source calibration. *The Astrophysical Journal Supplement*, 152:129–135, 2004.

W. van Straten. High-fidelity radio astronomical polarimetry using a millisecond pulsar as a polarized reference source. *The Astrophysical Journal Supplement*, 204, 2013.

Willem van Straten, Paul Demorest, and Stefan Oslowski. Pulsar data analysis with psrchive. *Astronomical Research and Technology*, 9:237–256, 2012.

C. Venter, A. Kopp, A. K. Harding, P. L. Gonthier, and I. Büsching. Cosmic-ray positrons from millisecond pulsars. *The Astrophysical Journal*, 807, 2015.

P. Ventura, M. Di Criscienzo, F. D'Antona, E. Vesperini, M. Tailo, F. Dell'Agli, and A. D'Ercole. The formation of multiple populations in the globular cluster 47 tuc. *Monthly Notices of the Royal Astronomical Society*, 437:3274–3282, 2014.

F. Verbunt and P. C. C. Freire. On the disruption of pulsar and x-ray binaries in globular clusters. *Astronomy and Astrophysics*, 561, 2014.

J. F. C. Wardle and P. P. Kronberg. The linear polarization of quasi-stellar radio sources at 3.71 and 11.1 centimeters. *Astrophysical Journal*, 194:249–254, 1974.

J. M. Weisberg and J. H. Taylor. The relativistic binary pulsar b1913+16: Thirty years of observations and analysis. In *Binary Radio Pulsars, ASP Conference Series*, volume 328, page 25, Aspen, Colorado, USA, 2005.

W. A. Wheaton, J. P. Doty, F. A. Primini, B. A. Cooke, C. A. Dobson, A. Goldman, M. Hecht, S. K. Howe, J. A. Hoffman, and A. Scheepmaker. An absorption feature in the spectrum of the pulsed hard X-ray flux from 4U0115 + 63. *Nature*, 282:240–243, 1979.

J. A. Wheeler. Superdense stars. *Annual Review of Astronomy and Astrophysics*, 4:393, 1966.

L. M. Widrow. Origin of galactic and extragalactic magnetic fields. *Reviews of Modern Physics*, 74:775–823, 2002.

A. Wolszczan and D. A. Frail. A planetary system around the millisecond pulsar PSR1257 + 12. *Nature*, 355:145–147, 1992.

E. M. H. Wu, C. Y. Hui, A. K. H. Kong, P. H. T. Tam, K. S. Cheng, and V. A. Dogiel. Chandra detection of a new diffuse x-ray component from the globular cluster 47 tucanae. *The Astrophysical Journal*, 788:L40–L45, 2014.

S. Xu and B. Zhang. Interpretation of the structure function of rotation measure in the interstellar medium. *eprint arXiv:1604.05445*, 2016.

X. P. You, G. Hobbs, W. A. Coles, R. N. Manchester, R. Edwards, M. Bailes, J. Sarkissian, J. P. W. Verbiest, W. van Straten, A. Hotan, S. Ord, F. Jenet, N. D. R. Bhat, and A. Teoh. Dispersion measure variations and their effect on precision pulsar timing. *Monthly Notices of the Royal Astronomical Society*, 378:493–506, 2007.

Ringraziamenti

Concluso il lavoro di Tesi, vorrei dedicare qualche paragrafo in italiano a tutte quelle persone che mi hanno aiutato e sostenuto durante questo lungo periodo. Prima di tutti vorrei ringraziare la mia famiglia che mi ha sempre sostenuto (affettivamente ma anche finanziariamente) nelle mie scelte per tutto il periodo di questo lavoro.

Vorrei ringraziare la mia relatrice, la Prof.ssa Monica Colpi, che, con grande entusiasmo e dedizione, mi ha avvicinato allo studio delle pulsar e ha reso possibile la collaborazione con l'Osservatorio Astronomico di Cagliari. Vorrei ringraziare il Dott. Gabriele Ghisellini che, durante la tesi triennale e i successivi incontri, mi ha ispirato una grande passione per la ricerca. Inoltre, vorrei ringraziare tutti i miei amici e compagni di studio con cui ho passato grandi avventure in questi anni e che hanno reso piacevoli anche le situazioni più dure.

Sentiti ringraziamenti vanno anche a tutto lo staff dell'Osservatorio Astronomico di Cagliari. In primis al direttore, Andrea Possenti, con cui ho realizzato questo magnifico lavoro. Disponibile in ogni momento ad darmi aiuto e consiglio, nonostante i numerosi impegni, ha sempre mostrato una gentilezza ed una fiducia che mi hanno spinto ad andare avanti. È merito suo se questo lavoro è stato portato a compimento. Vorrei ringraziare anche tutte le splendide persone dell'ufficio 54, gli abili giocatori di basket del Pala Pilia e tutti quelli che mi hanno aiutato durante la mia permanenza.

Un altro ringraziamento molto sentito va alla Dott.ssa Caterina Tiburzi. Le lunghe discussioni via mail che ci siamo scambiati si sono dimostrate essenziali per l'analisi dei dati. La ringrazio per la grande disponibilità e il forte incoraggiamento durante il lavoro.

Un ringraziamento va anche ai miei coinquilini di Cagliari per avermi offerto tante cene e per avermi consigliato bellissimi posti da visitare. Ringrazio anche tutti i praticanti del dojo di Aikido Musubi no Kai perché con la loro affettuosità e il loro entusiasmo mi hanno sempre fatto sentire a casa.

Infine vi lascio con una foto della mia creazione di legno che rappresenta tutto il duro lavoro fatto: un modello dell'ammasso globulare 47 Tucanae composto da 47 tucani realizzati in legno.